In-situ electron microscopy investigation of ferroelectric domain switching kinetics

Zibin Chen

A thesis submitted in fulfilment of the requirements for the degree of Doctor of Philosophy

Faculty of Engineering and Information Technologies

The University of Sydney

2017

献给我的家庭

Dedicated to my family

Declaration of Originality

I certify that this thesis does not incorporate without acknowledgement any material previously submitted for a degree or diploma in any university; and that to the best of my knowledge and belief it does not contain any material previously published or written by another person except where due reference is made in the text.

Signed: _____ On: _____/____/_____

Acknowledgements

This dissertation does not only represent my work on the material research itself; it is a milestone in more than three years of PhD research in the School of Aerospace, Mechanical and Mechatronic Engineering and the Australian Centre for Microscopy and Microanalysis at the University of Sydney. Since the first day of my enrolment as an MPhil student six years ago, I have felt at home in this research group. Throughout these years, I have been supported by my wife, my parents, my parents-in-law and my research colleagues, whom I wish to acknowledge. I have also met and learned from dozens of remarkable individuals to whom I would like to express my gratitude.

I would foremost like to thank my supervisor, Professor Xiaohzou Liao, for his professional guidance and constant support during my study. He has been greatly supportive since the day I began working in this research group. He taught me how to conduct research, how to devise a research idea, how to write an academic paper and how to become a qualified scientist.

I would like to express my gratitude to my co-supervisor, Professor Simon P. Ringer, who has provided me with an excellent opportunity to work and study in one of the largest microscopy centres in Australia. I also would like to thank Professor Julie Cairney and Ms Ellie Kable for providing me with an opportunity to work as a part-time lab manager in the centre.

This project was undertaken in collaboration with several other research groups all over the world whose contributions were essential. I would like to thank Dr Hong Liang and Professor Long-Qing Chen from Pennsylvania State University for their professional support in field–field simulations. Without their industrious input, the validity of my work may never have been realised. I would also like to thank Professor Feifei Wang from Shanghai Normal University, Professor Xiaolin Wang from the University of Wollongong and Professor Haosu

Luo from the Shanghai Institute of Ceramics for providing the necessary samples for this project. My thanks are likewise extended to Dr David Mitchell from the Electron Microscopy Centre of the University of Wollongong and Dr Hongwei Liu, Dr Patrick Trimby and Mr Steve Moody from the University of Sydney for their help with microscopy characterisation.

I offer my thanks to numerous friends and colleagues who have assisted me with my study. I am grateful to Dr Xianghai An for his help and suggestions in both academic and non-academic areas. I thank Dr Yujie Chen, Dr Yang Cao, Dr Jingli Sun, Dr Suqin Zhu, Mr Silu Liu, Mr Peng Gao, Mr Zening Mao, Mr Ranming Niu, Ms Qianwei Huang, Mr Hansheng Chen, Ms Fan Yun, Mr Jiangtao Qu, Mr Pengju Bian, Mr Yang Liu, Ms Yan Deng and Mr Ruhao Fang for their great support and companionship.

Most importantly, I would like to thank my beloved wife, Dr Liuen Liang, for her unconditional love and trust. Her endless support has pacified me during my most dispirited periods and her company has helped me through my most difficult times. This work would have been impossible without her love and support. I would also like to thank my parents and my parents-in-law, who have always supported me and treated me as their own.

Publication List

Journal Papers related to this thesis:

1. **Z.B. Chen,** L. Hong, F.F. Wang, S.P. Ringer, L-Q. Chen, H.S. Luo, X.Z. Liao
   Facilitation of ferroelectric switching via mechanical manipulation of hierarchical nanoscale domain structure
   Physical Review Letters **118**, 017601 (2017)

2. **Z.B. Chen**, X.L. Wang, S.P. Ringer, and X.Z. Liao
   Manipulation of Nanoscale Domain Switching Using an Electron Beam with Omnidirectional Electric Field Distribution
   Physical Review Letters **117**, 027601 (2016).

3. **Z.B. Chen,** L. Hong, F.F. Wang, X.H. An, X.L. Wang, S.P. Ringer, L-Q. Chen, H.S. Luo, X.Z. Liao
   Domain switching kinetic by mechanical and electrical stimulation in relaxor-based ferroelectric for non-volatile memories
   (In preparation)

4. **Z.B. Chen,** L. Hong, F.F. Wang, X.H. An, X.L. Wang, S.P. Ringer, L-Q. Chen, H.S. Luo, X.Z. Liao
   Stress-induced 'elastic' and 'plastic' ferroelectric domain switching
   (In preparation)

Thesis authorship attribution statement

Chapter 3 of this thesis is published as:

> **Z.B. Chen**, X.L. Wang, S.P. Ringer, and X.Z. Liao
> Manipulation of Nanoscale Domain Switching Using an Electron Beam with Omnidirectional Electric Field Distribution
> *Physical Review Letters* **117**, 027601 (2016).

I designed the study, analysed the data and wrote the drafts of the manuscript.

Chapter 5 of this thesis is published as:

> **Z.B. Chen,** L. Hong, F.F. Wang, S.P. Ringer, L-Q. Chen, H.S. Luo, X.Z. Liao
> Facilitation of ferroelectric switching via mechanical manipulation of hierarchical nanoscale domain structure
> *Physical Review Letters* **118**, 017601 (2017)

I designed the study, interpreted the simulation results done by Dr. Hong Liang and Prof. Long-Qing Chen, analysed the data and wrote the drafts of the manuscript.

Table of Contents

List of Figures

Abstract

Because of their ultrahigh piezoelectricity, pyroelectric properties, mechanical/electrical hysteresis and possession of non-volatile polarisation states, ferroelectric materials have been used in various electronic devices, including various sensors, actuators, transducers, micromotors and non-volatile memories. The mechanical, electrical, electromechanical and thermoelectric properties are crucial factors in device applications of ferroelectric materials. These properties are particularly sensitive to changes in the embedded microscopic structures. Therefore, the mechanical and electrical characterisation of ferroelectric materials and the observation of their microstructural evolution under external stimuli are necessary for understanding their unique properties. However, this is not an easy task because of the difficulties involved in the mechanical and electrical testing of nano/microscale materials.

Various techniques have been used to investigate the mechanical and electrical behaviours of ferroelectric materials—among which in-situ transmission electron microscopy is one of the most effective. This thesis aims to combine state-of-the-art in-situ transmission electron microscopy techniques, the scanning transmission electron microscopy high-angle annular dark-field imaging technique and phase-field modelling to investigate microstructural evolution in ferroelectric materials under different external stimuli. One of the ultimate goals of this research is to improve the performance of non-volatile ferroelectric memory devices.

In Chapter 1, the history, properties and applications of multiferroics, ferroelectrics and relaxor-based ferroelectrics are introduced and the mechanical and electrical characterisation techniques are summarised.

In Chapter 2, experimental techniques including scanning electron microscopy, the focused ion beam technique, transmission electron microscopy, scanning transmission electron

microscopy, an in-situ nanomechanical–electrical testing system and sample preparation techniques are described. The phase-field modelling method is also introduced.

In Chapter 3, a technique to manipulate nanoscale domain switching using an electron beam with omnidirectional electric field distribution is investigated. Reversible ferroelectric domain manipulation with a high spatial resolution is critical for memory storage based on thin-film ferroelectric materials. The ferroelectric domain can be manipulated using techniques that apply heat, mechanical stress or electric bias. However, these techniques have certain drawbacks. In this chapter, I propose to use an electron beam with an omnidirectional electric field as a tool for erasable stable ferroelectric nanodomain manipulation. My results suggest that a local accumulation of charges contributes to the local electric field that determines domain configurations.

Chapter 4 addresses ferroelastic domain switching by the mechanical and electrical stimulation for non-volatile memories. Ferroelectric materials have been extensively explored for high-density non-volatile memory devices because of their ferroelectric/ferroelastic domain switching behaviour under electric loading or mechanical stress. However, the existence of ferroelectric and ferroelastic backswitching can cause significant data loss and thus affect the reliability of data storage. In this chapter, ferroelastic domain switching in single-crystal $Pb(Mg_{1/3}Nb_{2/3})O_3$-33%$PbTiO_3$ pillars by electrical and mechanical stimuli is investigated using in-situ transmission electron microscopy and phase-field modelling. Results show that electrical stimulation leads to a mechanically irreversible ferroelastic domain state, while mechanical excitation results in the formation of a mechanically reversible domain state. I propose an approach that takes advantage of the mechanically reversible and irreversible states of ferroelastic domain configurations for advanced bit writing and reading for non-volatile memories. Because this approach does not consider the ferroelectric domain polarisation

direction, it overcomes the backswitching problem and broadens the types of ferroelectric materials for non-volatile memory applications.

Chapter 5 shows the facilitation of ferroelectric switching via the mechanical manipulation of hierarchical nanoscale domain structures, exploring heterogeneous ferroelastic transition that produces hierarchical 90° nano-tetragonal domains via mechanical loading as well as its effect on facilitating ferroelectric domain switching in relaxor-based ferroelectrics. Combining in-situ electron microscopy characterisation and phase-field modelling, I reveal the nature of the domain transition process and discover that the domain transition lowers the electrical loading threshold needed for ferroelectric domain switching by 40%. These results advance the fundamental understanding of ferroelectric domain switching behaviour.

In Chapter 6, I systematically study domain switching kinetics under a very large mechanical loading. The study reveals the capability of mechanical loading for manipulating 90° and 180° ferroelastic and ferroelectric domains using low-level and high-level mechanical loadings respectively. The domain switching behaviour is found to be reversible and permanent when the sample is subjected to low and high mechanical loadings, respectively. This study provides new insights for understanding the mechanical behaviour of ferroelectric materials.

In Chapter 7, major conclusions are drawn from my research and future perspectives are suggested.

Table of Abbreviations

ECM	Electrical characterisation module
EELS	Electron energy-loss spectroscopy
FIB	Focused ion beam
HAADF	High-angle annular dark field
MPB	Morphotropic phase boundary
PTP	Push-to-pull
SEM	Scanning electron microscope
STEM	Scanning transmission electron microscope
TEM	Transmission electron microscopy

Chapter 1

Introduction

1.1. Introduction of ferroelectric materials

An electric insulator that can be polarised by an electric field is called a dielectric material[1]. When a dielectric material is placed in an electric field, electrons do not flow through the material. Instead, positive charges shift towards the electric field while negative charges are repelled in the opposite direction, which is termed dielectric polarisation[2]. This creates an internal electric field that can offset the overall field within the dielectric material. As a result of this property, dielectric materials have been widely used in the storage and dissipation of electric energy.

In the early 1880s, the brothers Pieer and Jacques Curie discovered the phenomenon known as piezoelectricity in α-quartz crystals[3]. A material with piezoelectricity is capable of linearly converting applied mechanical energy into electrical energy or vice versa[4]. By changing the mechanical stress from compression to tension, the sign of the generated electric field is changed. When mechanical strain is applied to a piezoelectric crystal, electric dipoles—caused by the separation of positive and negative charges—are generated and aligned[5, 6]. This alignment of electric dipoles is called electric polarisation. Among the 32 crystallographic point groups of dielectric crystals, 20 are noncentrosymmetric. A piezoelectric crystal is always one of these 20 noncentrosymmetric crystalline structures. Ten of these 20 noncentrosymmetric point groups can result in spontaneous electric polarisation at low temperatures (below the

Curie temperatures of the materials). By varying the temperature, a flow of charges is generated from the material's surface, which is termed a pyroelectric effect[7, 8]. Materials possessing pyroelectricity are referred to as pyroelectric materials. Among those pyroelectric materials, materials that can have their polarisation reversed by the application of an external electric field are called ferroelectric materials[9-11]. A schematic diagram of the relationship between piezoelectrics, pyroelectrics and ferroelectrics is shown in Figure 1-1.

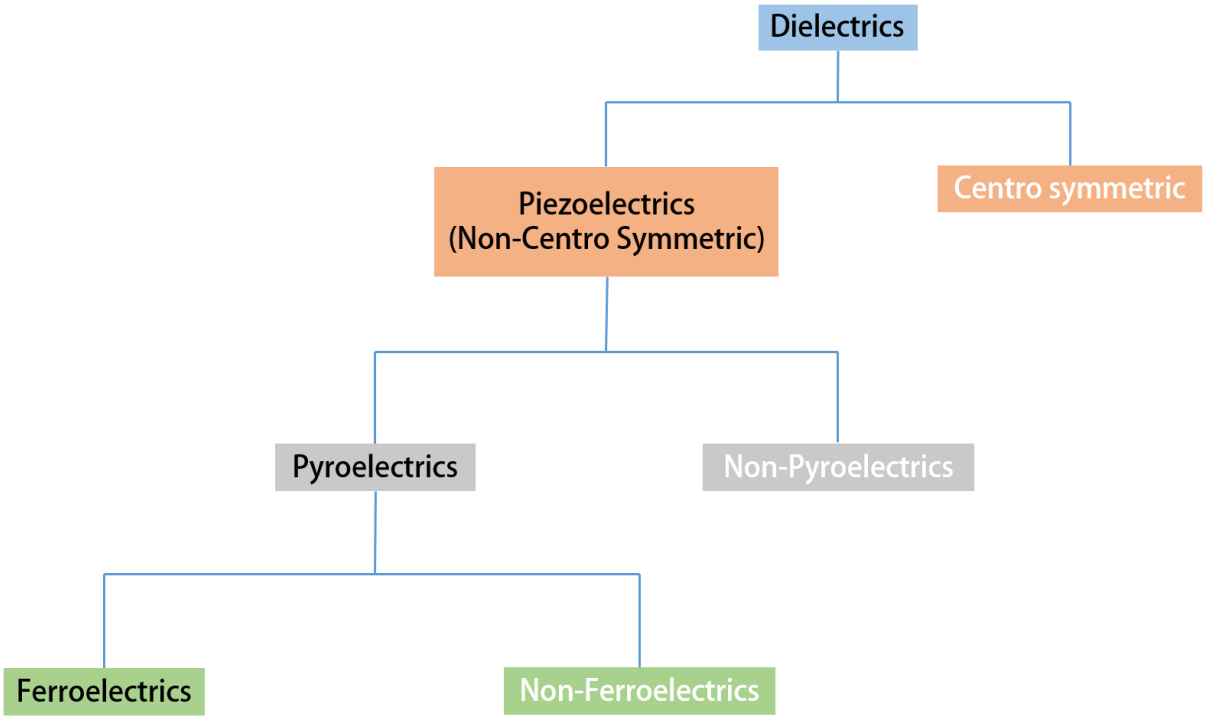

Figure 1-1 A schematic diagram of the relationship between piezoelectrics, pyroelectrics and ferroelectrics.

Ferroelectric materials demonstrate spontaneous electric polarisation in the absence of an external electric field. When the temperature is above a certain value T_c, which is called the Curie temperature[12], the unit cell of a ferroelectric crystalline material becomes cubic with a centrosymmetric atomic arrangement. Any ferroelectric material at a temperature higher than T_c loses its spontaneous polarisation and ferroelectricity, resulting in a phase called the paraelectric phase[13]. The paraelectric phase transfers back to the ferroelectric phase once the temperature falls below T_c.

The first ferroelectric material, Rochelle salt, was discovered in 1921[14]. After that, hundreds of other ferroelectric materials were discovered—of which the most commercially and scientifically important ones comprise the ABO_3 family[15]. In the 1940s, the discovery of ferroelectricity in barium titanate ($BaTiO_3$), an important ferroelectric material in the ABO_3 family, led to the increased scientific study of ferroelectric materials[16-20]. It was found that $BaTiO_3$ possesses a strong piezoelectric effect after electrical poling and proves to be a more useful replacement for some conventional piezoelectric materials (i.e., quartz)[1, 21]. However, its relatively poor stability at low temperature during the low-temperature ferroelectric phase transition makes it a less than ideal material for commercial use[22]. Ferroelectric phase transition usually occurs by ion displacement. The $BaTiO_3$ crystal structure is shown in Figure 1-2.

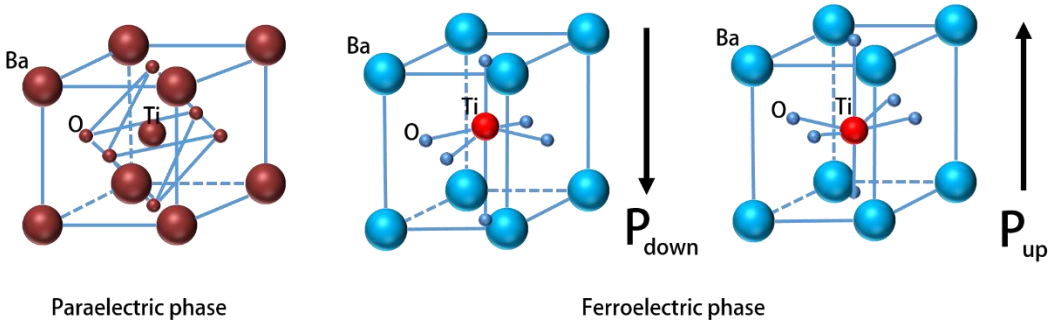

Figure 1-2 The crystal structures of $BaTiO_3$.A paraelectric or a ferroelectric phase presents depending on whether the temperature is above or below the Curie temperature.

When the temperature increases to above 120°C (T_c of $BaTiO_3$), barium and titanium cations and oxygen anions are in positions so that the positive and negative charge centres are overlapped. No electric dipole exists and $BaTiO_3$ is in the paraelectric phase showing paraelectric cubic symmetry. Immediately after the temperature has cooled to below 120°C, all ions displace over short distances. The displaced ions result in the separation of positive and negative charge centres, leading to the formation of an electric dipole moment and a phase transformation to a ferroelectric tetragonal phase. Phase transformation to a ferroelectric orthorhombic phase and a ferroelectric rhombohedral phase continues when the temperature

falls below 0°C and −90°C respectively. $LiNbO_3$ is another ferroelectric material in the ABO_3 family which possesses a high Curie temperature of 1210°C[23, 24]. However, its much lower piezoelectric constant than that of $BaTiO_3$ makes $LiNbO_3$ less useful for serving piezoelectric purposes.

A significant advance in the understanding of ferroelectric materials was made through the discovery of lead zirconate titanate ($Pb(Zr_{1-x}Ti_x)O_3$, PZT) in the 1950s[25, 26]. This material is a solid solution of different compositions of $PbZrO_3$ and $PbTiO_3$. Of particular significance for a PZT material is that it shows remarkably high dielectric and piezoelectric properties within a specific range of compositions[27-31]. This specific range of compositions is termed the morphotropic phase boundary (MPB)[32-34] and will be discussed in detail in Section 1.2.1.1. The importance of PZT material in electronic and thermo devices was realised in the 1960s[35, 36]. Since then, PZT has been widely used as a high-performance ferroelectric material and has dominated the piezoelectric material market until now.

A region of a ferroelectric material within which spontaneous polarisation is constant is termed a ferroelectric domain. The formation of a domain structure minimises the system's free energy when the material undergoes a transition from a paraelectric phase to a ferroelectric phase[37-39]. A thin interface separating two adjacent domains is called a domain wall[40].

A unique feature of ferroelectric materials is the formation of domain structures through the spontaneous breaking of crystal symmetry, resulting in hysteresis loops with different conjugate fields[41-44]. In general, different ferroelectric materials possess fingerprint-like unique hysteresis loop.

Figure 1-3 shows a typical ferroelectric hysteresis loop[45, 46]. Several characteristic parameters that will be explained in detail below, including spontaneous polarisation (saturation polarisation), the coercive field and remnant polarisation, can be found in the

hysteresis loop. To minimise the giant internal stress generated during the cooling process, a large single domain is usually split into multiple small domains associated with a large number of domain walls[47]. Initially, domain directions are randomly distributed so as to minimise free energy, leading to zero net polarisation in materials. When an external field with strength higher than the coercive field is applied, the polarisation gradually rotates, resulting in domain switching. The observed hysteresis behaviour in ferroelectric materials occurs because of the domain-wall motion. By increasing the applied field, the polarisation is finally saturated and the induced polarisation is proportional to the electric field where the material becomes a linear dielectric. The spontaneous polarisation is estimated by intercepting the vertical polarisation axis with the saturated linear segment. Upon polarisation saturation, multiple domains form a single large domain. As soon as the strength of the field decreases, domains start to back-switch in association with the polarisation rotating backward. Instead of turning back to net zero polarisation when the external field is completely withdrawn, remnant polarisation exists.

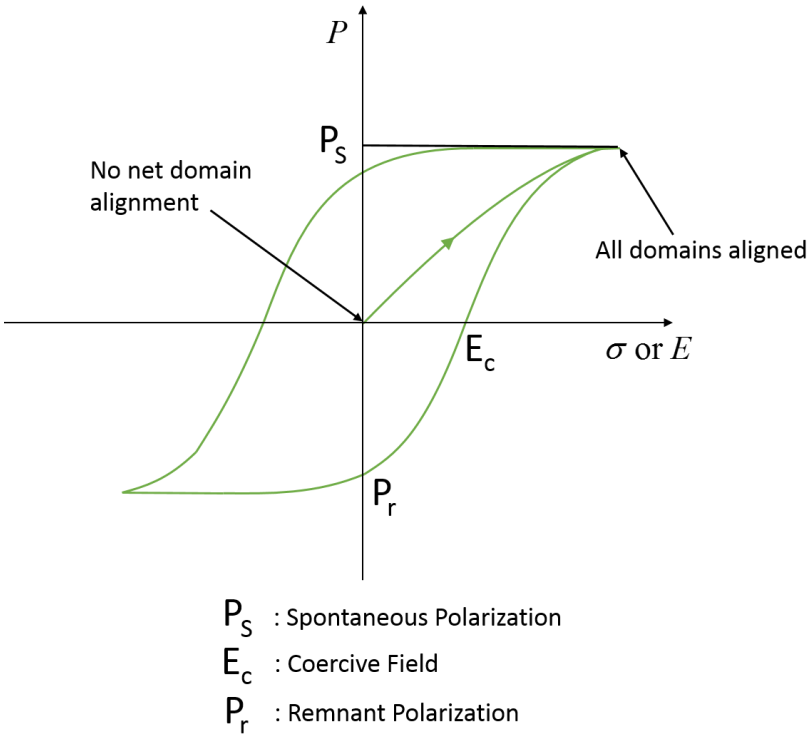

Figure 1-3 A typical ferroelectric hysteresis loop.

A zero polarisation can be obtained when an electric field from the opposite direction and of the same strength of the coercive field is applied. The same polarisation/domain reorientation can be achieved if an electric field is applied from the opposite direction. By analysing the hysteresis loop, scientists can comprehensively understand the ferroelectric properties and the bulk polarisation orientation of a ferroelectric material.

As a consequence of their novel pyroelectric properties and their outstanding piezoelectric properties, ferroelectric materials have been used as essential components in a wide variety of electronic devices[48]. They are widely used for manufacturing non-volatile memories[49-53], various sensors[54-57], actuators[58-63], ultrasonic micromotors[64, 65], micropumps[66-68], transducers[69-71] and photonic devices[72-75].

A non-volatile memory possesses a non-information-loss feature even when no power is supplied. The principle of non-volatile memory devices is based on polarisation reversal by applying an external electric field to a ferroelectric material. In these devices (shown in Figure 1-4), two polarisations that are opposite in direction act as the two logical signals 0 and 1, serving as memory bits that can be written and read by applying an electric field[76]. Ferroelectric memories exhibit much higher performance levels than other memory devices[77, 78]. Their writing and reading cycle time can be as short as 150 ns, which is about 100 times less than the time required by commercial flash memory. Their endurance is about 10 trillion, which is 1 million times longer than flash memory. Further, they consume very little power, which is of significance to miniature devices.

Writing of logical signals in memory bits using electrical wires of ferroelectric memory consisting of only 256 bits was first demonstrated in 1987[79]. Until the present, multiple approaches have been proposed for writing memory bits, including applying mechanical[80] and

electrical loading. Tracing these tracks, scientists have significantly enhanced the performance and the data-storage capacities of memory devices.

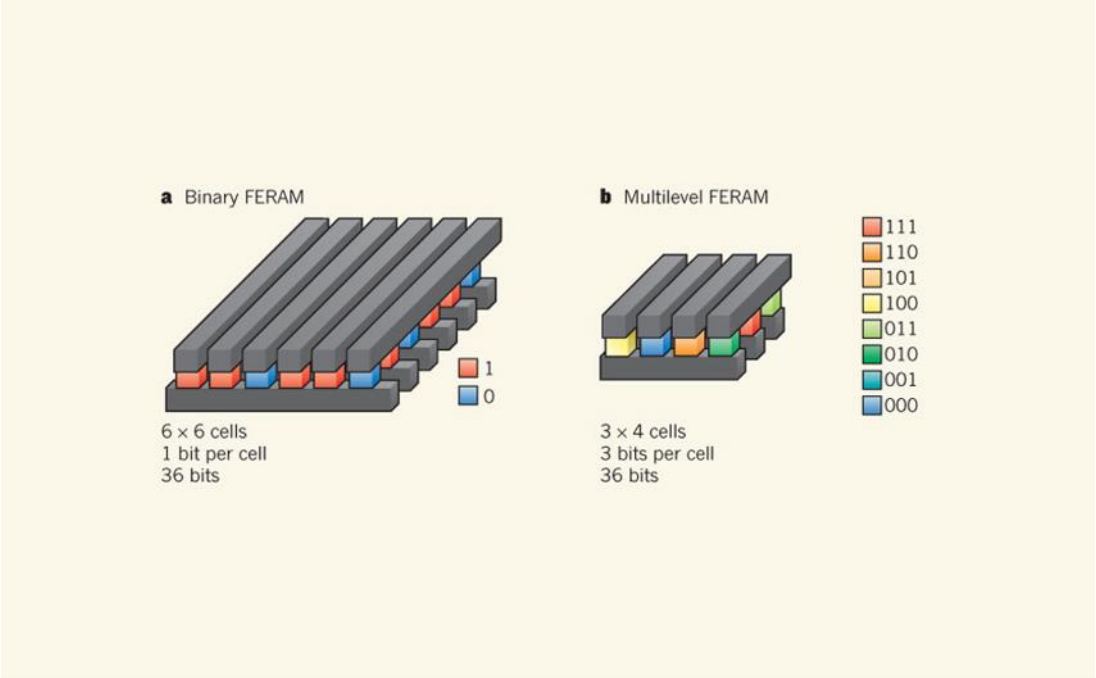

Figure 1-4 A binary and multilevel design of ferroelectric random access memory. In the binary ferroelectric random access memory, one bit of information '0' (blue) and '1' (red) is stored in a constituent cell. Electrical wires of grey colour are used to read and write the cells' polarisation. In the multilevel ferroelectric random access memory, each cell can be used to store three-bit logic states (000, 001, 010, 011, 100, 101, 110, 111) [76].

Recently, electromechanical devices such as sensors, actuators and transducers that are fabricated based on the microelectromechanical system (MEMS)[81-84] and the nanoelectromechanical system (NEMS)[61, 85-87], have attracted significant attention. Compared to the traditional materials for MEMS and NEMS, ferroelectric materials possess excellent electromechanical coupling factors, high piezoelectric constants, high sensibility to external temperatures, low power dissipation, and high signal-to-noise ratios, providing an excellent option for the electromechanical device market.

1.2. Relaxor-based ferroelectric and multiferroic materials

1.2.1. Relaxor-based ferroelectric materials

The first relaxor ferroelectric material was discovered in the late 1950s through the lead magnesium niobate [$Pb(Mg_{1/3}Nb_{2/3})O_3$] solid solution system[2]. Since this, a series of relaxor ferroelectric materials, including $Pb(Zn_{1/3}Nb_{2/3})O_3$[88, 89] and $Pb(Sc_{0.5}Nb_{0.5})O_3$[90, 91], have been discovered and widely studied. Relaxor ferroelectrics possess different features to other common ferroelectrics[92-96]. Compared to normal ferroelectrics ($BaTiO_3$ for example), relaxor ferroelectrics do not have a fixed Curie temperature[97]. Instead, the paraelectric to ferroelectric phase transition occurs within a temperature range—a process that is known as diffuse phase transition[93, 98]. Normal ferroelectrics exhibit a sharp peak in the dielectric constant at the temperature of dielectric maximum T_m. This peak is insensitive to electrical frequency in normal ferroelectric material as shown in Figure 1-5(a). In contrast, relaxor ferroelectrics exhibit a diffuse maximum of the dielectric constant at T_m with a change in frequency dispersion, resulting in a shift of the maximum dielectric constant towards higher temperatures with increasing frequency as shown in Figure 1-5(b)[92].

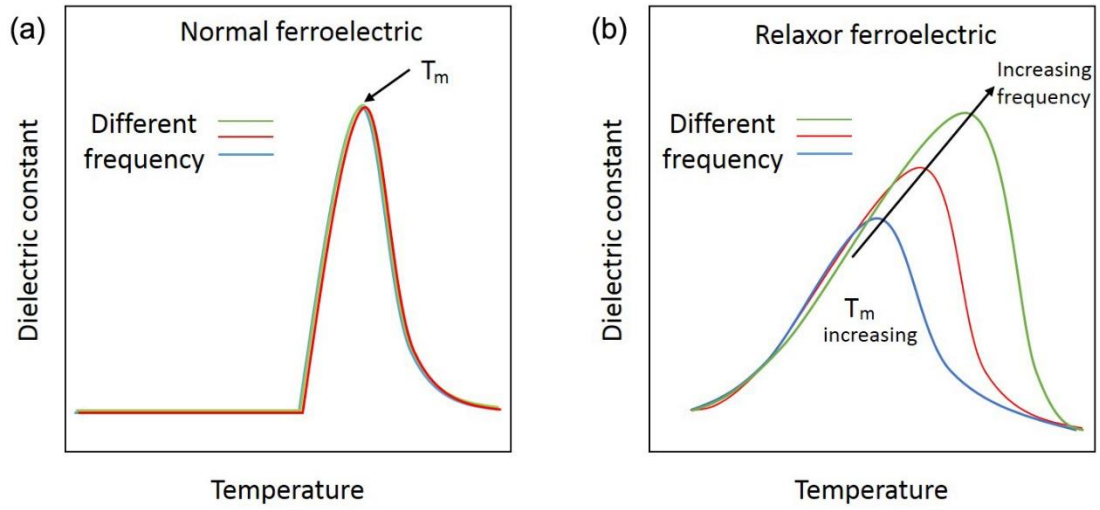

Figure 1-5 The dielectric constant and temperature behaviours for **(a)** normal ferroelectric and **(b)** relaxor ferroelectric.

Some scientists have suggested that the unique features of relaxor ferroelectrics result from the existence of local inhomogeneous polar clusters[99-104], known as the polar micro-regions or nano-regions[104]. These local regions possess a giant electromechanical response and are easily polarised by external stimuli, resulting in a modification of the dielectric properties of relaxor ferroelectrics. It has been proposed that the diffuse phase transition arises from compositional inhomogeneity[105, 106] and that composition is highly localised in relaxor ferroelectrics, resulting in different transition temperatures in different regions and in a broadening of the dielectric peak. Other theories have been proffered to explain the origin of the relaxor ferroelectric behaviour, including the martensitic phase transition model[107], the superparaelectric model[108, 109], the dipolar glass model[97, 110, 111], the random-field model[98, 112], and the random-bond, random-field model[113, 114].

Relaxor ferroelectrics are solid solutions with ferroelectric, complex $A(B_1B_2)O_3$ perovskite structures[93, 115] in which A represents A-site ions (i.e. Pb^{2+}), B_1 and B_2 represent B-site ions ($B_1 = Mg^{2+}$, Zn^{2+}, Sc^{3+}, Fe^{3+}, In^{3+}, …; $B_2 = Nb^{5+}$, Ta^{5+}, W^{6+}, …). A typical A-site complex relaxor ferroelectric is $(Pb_{1-x}Ba_x)(Zr_yTi_{1-y})O_3$. While A-sites are commonly occupied by Pb^{2+} ions, B-site ions are more flexible and are randomly arranged. Some widely studied B-site complex relaxor ferroelectrics are $Pb(Mg_{1/3}Nb_{2/3})O_3$, $Pb(Zn_{1/3}Nb_{2/3})O_3$, $Pb(Sc_{1/2}Ta_{1/2})O_3$, $Pb(Fe_{2/3}W_{1/3})O_3$, $Pb(Sc_{1/2}Nb_{1/2})O_3$ and $Pb(In_{1/2}Nb_{2/3})O_3$.

While both relaxor ferroelectrics and normal ferroelectrics exhibit piezoelectric properties, a giant piezoelectric constant is found from a material called relaxor-based ferroelectric[6, 116]. A relaxor-based ferroelectric material is generally a solid solution of relaxor with a normal ferroelectric $PbTiO_3$. In 1969, the first relaxor-based ferroelectric (1-x) $Pb(Zn_{1/3}Nb_{2/3})O_3$ – x $PbTiO_3$ (PZN-PT) was reported[117]. At room temperature, $Pb(Zn_{1/3}Nb_{2/3})O_3$ is a relaxor ferroelectric with short-range-ordering rhombohedral symmetry while $PbTiO_3$ is a normal ferroelectric with long-range-ordering tetragonal symmetry. It is

found that by increasing the $PbTiO_3$ content, the relaxor-behaving PZN-PT slowly transforms into a normal ferroelectric[118]. Meanwhile, the short-range ordering at a low $PbTiO_3$ content converts to long-range ordering at a high $PbTiO_3$ content, leading to a reduction in phase transition diffuseness and dielectric relaxation.

In 1997, relaxor-based ferroelectrics PZN-PT and PMN-PT with compositions situated near the MPB were reported to exhibit a giant electric-field-inducing strain of up to 1.7%, with an ultrahigh electromechanical coupling factor of (k_{33})>94%, and piezoelectric coefficients of (d_{33}) > ~ 2500 pC/N[6]. These excellent behaviours have attracted much attention and extensive investigations have been carried out on relaxor-based ferroelectrics that are near the MPB over the past few decades.

1.2.1.1. Morphotropic phase boundary

Originally, 'morphotropic' was used to describe the phase transition that occurred through changing composition. Today, the term is mainly used for the common compositional boundary, the 'MPB', that separates two structural phases—the tetragonal and the rhombohedral phases—in ferroelectric materials[119, 120]. It was found that the transition phases near the MPB are unstable and sensitive to external stimuli—such as external electric fields, stress and heat—resulting in an ultrahigh piezoelectric constant and an electromechanical coupling factor. The compositional MPB is different for different ferroelectrics. Solid solution ferroelectric materials (1-x)$PbZrO_3$–x$PbTiO_3$(PZT) have been widely studied[10, 31, 121]. Above the Curie temperature, PZT possesses a paraelectric phase. Below the Curie temperature, ferroelectric phases, which comprise two crystal structures with different amounts of $PbTiO_3$, are achieved. The ferroelectric phase in the $PbZrO_3$-rich area is of rhombohedral symmetry while the ferroelectric phase in the $PbTiO_3$-rich area is of tetragonal symmetry. The MPB between these two ferroelectric phases is located at the composition $x \approx 0.48$. PZT ferroelectric materials with compositions near the MPB can allow the two phases (rhombohedral and

tetragonal) to coexist, which enhances the capability of transition between the two phases. Therefore, the best performance of the piezoelectric constant d_{33} = ~ 223 pC/N and the electromechanical coupling factor k_{33} = ~ 67% is found in PZT with a composition that is near to the MPB.

In some ferroelectrics such as PZT single crystals, the MPB is insensitive to temperature, while in other relaxor-based ferroelectrics, the compositional MPB depends strongly on temperature. Investigations have showed that the dielectric and pyroelectric properties of (1−x)PMN−xPT solid solutions vary across the MPB compositions x = 0.275-0.4[122].

Many studies have been conducted to further reveal the features of MPBs. Since the space groups of the tetragonal phase (P4mm) with the polar axis along <001>c and the rhombohedral phase (R3m) with the polar axis along $<111>_c$ are not symmetry related, a continuous-phase transition theory—the 'bridging theory'—was proposed to explain the phase transformation from tetragonal to rhombohedral[123-125]. Here, the subscript 'c' indicates that the crystallographic orientation refers to the cubic crystal structure. The bridging theory suggests that the transition from tetragonal to rhombohedral phase occurs via a monoclinic phase. Initially, the monoclinic phase[31, 126] was calculated to be non-existent, since the ferroelectric perovskite can be described by sixth-order free energy without considering the monoclinic phase[127]. Another typical theory, ferroelectric adaptive phase theory[128, 129], suggests that monoclinic phases, consisting of the miniaturisation of stress-accommodating tetragonal phases, are micro-averaged tetragonal phases. Later, calculations showed that an eighth-order free-energy expansion can generate three possible M phases, including M_A, M_B and M_c, between the rhombohedral, tetragonal and orthorhombic phases[130]. The rotation paths of M_A, M_B and M_c are shown in Figure 1-6.

Investigation of a homogeneous PZT single-crystal sample using high-resolution x-ray diffraction showed that a monoclinic phase existed between the tetragonal and rhombohedral phases in a narrow composition range[131]. The monoclinic phase with the space group of Cm is a subgroup of P4mm and R3m[132]. The polar axis of the monoclinic phase is close to the $<111>_c$ direction, which serves as a 'bridge' between the tetragonal and rhombohedral phases. Another experiment using high-resolution x-ray diffraction to study poled PZT in the vicinity of the MPB showed fruitful results[133]. It revealed that the piezoelectric elongation of the tetragonal and rhombohedral unit cells does not occur in polar directions, but in other directions associated with the monoclinic distortion. Ever since the discovery of the monoclinic bridging theory, more efforts have been made to understand the origin of this phase.

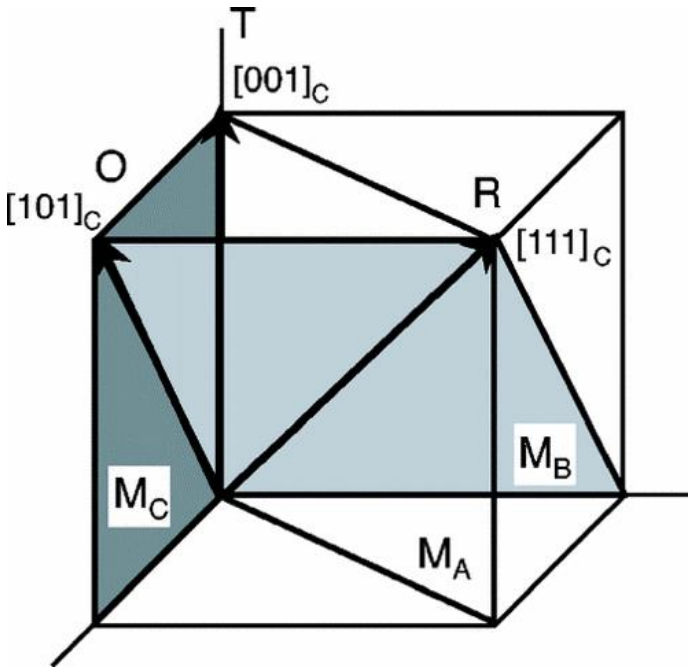

Figure 1-6 A schematic drawing of the rotation paths of M_A, M_B and M_c [134]. Phase transformation from T (tetragonal) to O (orthorhombic), from O to R (rhombohedral) and from T to R is via M_A, M_B and M_C paths respectively.

1.2.1.2. $Pb(Mg_{1/3}Nb_{2/3})O_3$-33%$PbTiO_3$

(1-x)PMN-xPT solid solution single crystal is a typical relaxor-based ferroelectric comprised of relaxor ferroelectric PMN and normal ferroelectric PT[135, 136]. The phase of this material at room temperature depends significantly on the composition x. The phase diagram of (1−x)PMN−xPT single-crystal solid solution is shown in Figure 1-7[137, 138].

According to the phase diagram, the MPB of the (1-x)PMN-xPT single crystal is located at a compositional range of $0.30 < \times < 0.35$. A mixture of the monoclinic, rhombohedral and tetragonal phases can be observed in the PMN-33PT single crystal at room temperature. A monoclinic phase possesses different angles of polarisation rotation which can be easily triggered by applying external stimuli. The polarisation vector of the monoclinic phase can rotate continuously under different external stimuli.

It is believed that the easily polarised, rotation-induced structural deformation in the PMN-33PT single crystal is the origin of the enhanced electromechanical properties[139-143]. Research has shown that the shear piezoelectric constant d_{15} in PMN-33PT can achieve a very high value[144]. At the same time, the piezoelectric constant d_{33} and the electromechanical coupling factor k_{33} are ultrahigh, reaching $d_{33} \approx 2820$ pC/N and $k_{33} \approx 94\%$ in the [001] poled single-crystal PMN-33PT—figures five times higher than those of the best modified PZT ceramics[6]. The easily polarised rotation induced by the external electric field through different paths generates significant strains through polarisation-strain coupling, resulting in significant piezoelectric properties for this material. Further, the phase transition from rhombohedral to tetragonal (or vice versa) induced by the electric field is another contributor to the ultrahigh electric-field-induced strain.

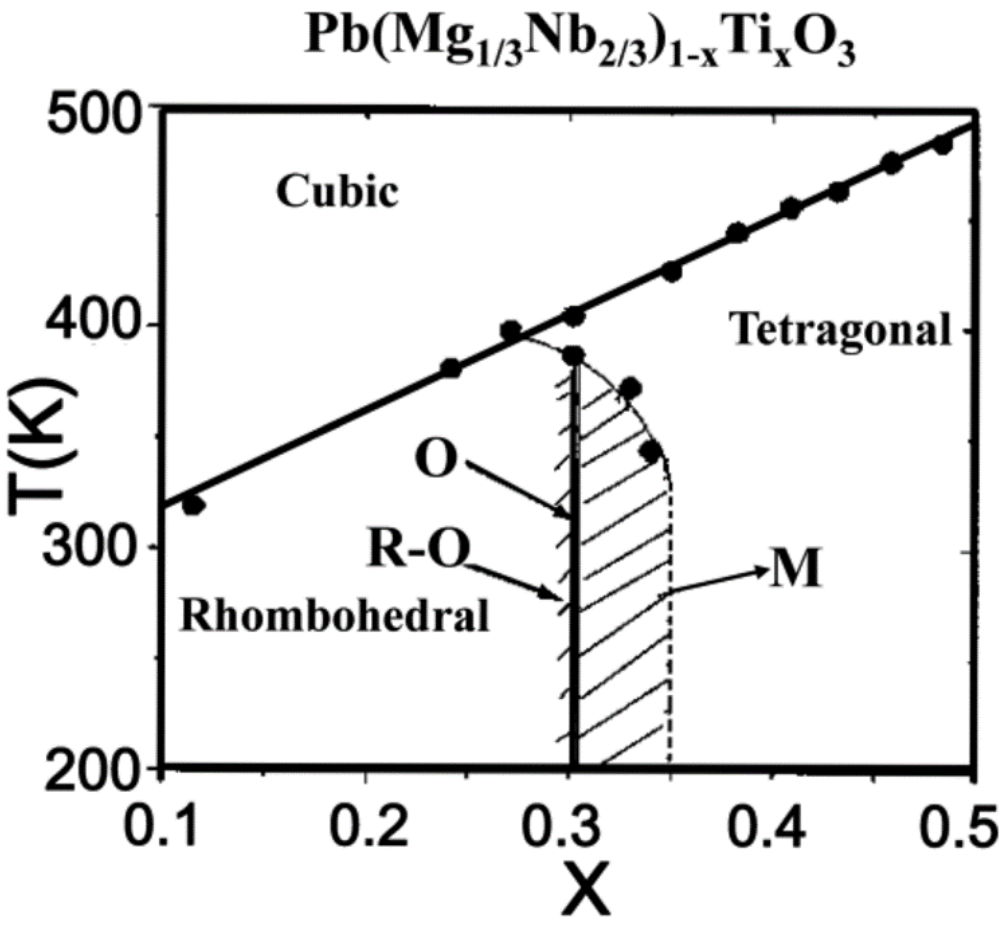

Figure 1-7 The phase diagram of (1−x)PMN−xPT [138]. PMN-PT solid solution exists as a rhombohedral phase, a monoclinic phase and a tetragonal phase when $x \leq 0.3$, $0.3 < x \leq 0.5$ and $0.5 < x$ respectively.

The comprehension and modelling of the structures of ferroelectrics, including domain structures, crystalline parameters to predict new structures and applications of ferroelectric materials, have become more prevalent in recent years[126, 145, 146]. These discoveries relied heavily on the unique features of polarisation orientation. The discoveries of different phases were initially made through the observation of different ferroelectric domains—rhombohedral, tetragonal and monoclinic domains—using an optical polarised microscope[136, 147, 148]. Later, these domain structures were distinguished in PMN-33PT using x-ray diffraction[149] and transmission electron microscopy (TEM) experiments[126, 145, 150].

1.2.1.3. $Pb(Mg_{1/3}Nb_{2/3})O_3$-38%$PbTiO_3$

Single crystalline $Pb(Mg_{1/3}Nb_{2/3})O_3$–38%$PbTiO_3$(PMN-38PT) has a composition that falls outside of the MPB separating the tetragonal phase and the rhombohedral phase. At room temperature, PMN-38PT exhibits the tetragonal phase[151], consisting of 90° ferroelastic domains and 180° ferroelectric domains as shown in Figure 1-8. As the tetragonal phase only possesses polarisation direction along $<001>_c$, the 90° ferroelastic domain walls are situated along $<011>_c$, while the 180° ferroelectric domain walls are located along $<001>_c$. Although PMN-38PT possesses a much smaller piezoelectric constant and electromechanical coupling factor than PMN-33PT, it is a better candidate for studying the domain switching dynamic by applying external stimuli as a consequence of its simple tetragonal structure at room temperature. The response of the tetragonal phase to external stimuli will be discussed in Chapters 5 and 6.

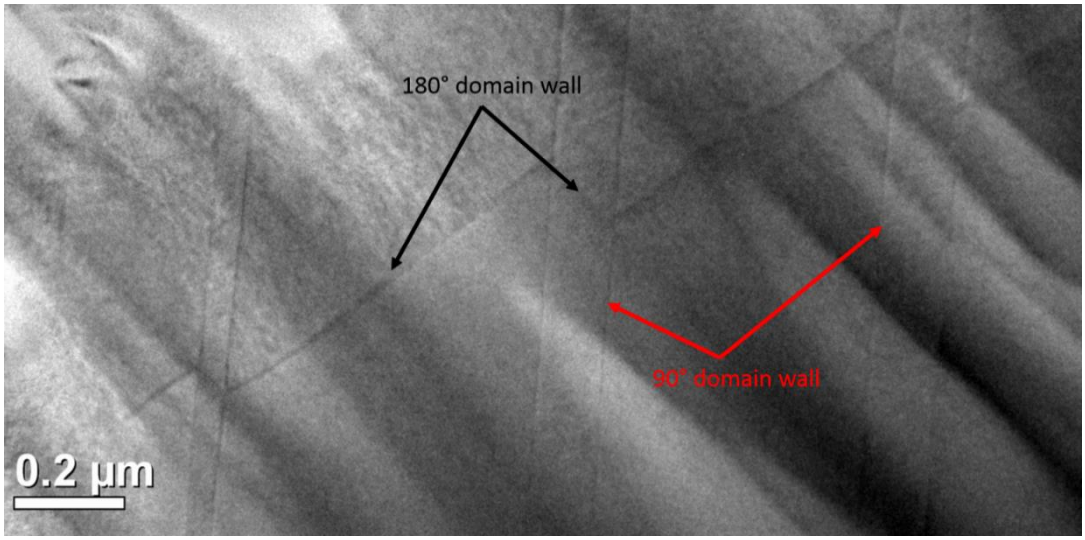

Figure 1-8 A typical TEM image of different domain/domain-wall structures in a PMN-38PT sample. Black arrows indicate 180° ferroelectric domain walls, while red arrows indicate 90° ferroelastic domain walls.

1.2.2. Multiferroic materials-$YMnO_3$

In the mid-nineteenth century, James Clerk Maxwell presented the now well-known Maxwell's equations regarding the dynamic relationship between electric and magnetic

fields[152]. Two independent phenomena, electric fields and magnetic fields, are intrinsically coupled together. Naturally, the origin of ferromagnetism[153] results from the ordering of electron spins in incomplete ionic shells while ferroelectricity comes from the shift-in-ions-induced electric dipoles. Maxwell's equations explain the similarities between the ferroelectric and the ferromagnetic—a milestone in the comprehension of the origins of ferroelectricity and ferromagnetism.

Multiferroic materials are known as materials comprised of ferromagnetism, ferroelectricity and ferroelasticity[154, 155]. Resulting from controlling spins by the variation of electric fields and charges, the coupling of ferromagnetism and ferroelectricity can be applied to many novel multifunctional devices, such as high-density memory devices[156, 157].

$ReMnO_3$ (where Re is rare earth and Re = Ho, Lu, Y and Sc) is among the materials belonging to the multiferroic family. The hexagonal manganites in $ReMnO_3$ present ferroelectricity because of the size mismatch between Re and Mn, which induces a trimerisation structural phase transition[158-160]. Hexagonal $ReMnO_3$ exhibits ferroelectric domains coupled with antiferromagnetic domains when a magnetic transition occurs below the ferromagnetic-transition temperature. At the same time, the ferroelectric domains are also found to be coupled with structural domains in the hexagonal $ReMnO_3$[161].

The multiferroic $YMnO_3$[158, 161, 162] is one member of the $ReMnO_3$ family. The crystal structure of $YMnO_3$ is shown in Figure 1-9. The $YMnO_3$ possesses a hexagonal structure consisting of a non-connected layer of MnO_5 trigonal bipyramids corner-linked by in-plane oxygen ions and forming close-packed planes separated by a layer of Y^{3+} ions with apical oxygen ions[158, 163]. The length of the yttrium-in-plane oxygen bonds is 0.285 nm, while the length of the Manganese-in-plane O bonds is 0.204 nm and the length of the Manganese-apical oxygen bonds is 0.190 nm.

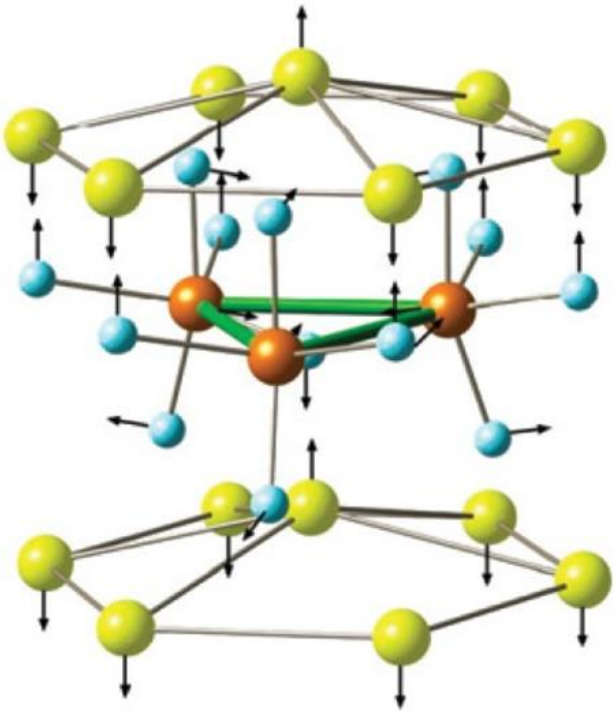

Figure 1-9 The crystal structure of $YMnO_3$. The yellow, brown and blue colours represent the Y, Mn and O ions respectively. The black arrows represent the ion displacement directions [161].

Single-crystal $YMnO_3$ has a Curie temperature of 914K, over which the $YMnO_3$ shows a paraelectric $P6_3/mmc$ phase[158]. In the paraelectric phase, all ions are constrained to planes and the {0001} planes run parallel to the ab plane of the lattice. Below the Curie temperature, the paraelectric phase transforms into a ferroelectric $P6_3cm$ phase. Therefore, the $YMnO_3$ is a ferroelectric material at room temperature. The first change from the paraelectric phase to the ferroelectric phase is the buckling of the MnO_5 bipyramids, which shortens the c axis[164]. As a result of the buckling, apical oxygen ions shift in-plane towards the yttrium-apical oxygen bonds. Yttrium ions also shift away from the ab plane, but retain their distance from the apical oxygen constantly. This results in the shortening of two yttrium-in-plane oxygen bonds from 0.28 nm to 0.23nm and in the increasing of the others to 0.34 nm[158]. This displacement of the

ions leads to a net electric polarisation. This net electric polarisation distorts the yttrium ions upward and downward along the c axis, resulting in 180° ferroelectric domains in the material.

This crystallographic domain pattern with six domains emerging from one point, resembling a cloverleaf pattern, can be found in the $YMnO_3$ single crystal[165-168]. Three types of antiphase domains, named α, β and γ, are found in the $YMnO_3$ and are alternatively separated by two types of antiphase domain boundaries (APB)–APB_I and APB_{II}. The formation of different antiphase domains is caused by the in-plane shifting of ions. Combined with two 180° ferroelectric domains, a cloverleaf pattern with six domains α+, β-, γ+, α-, β+, γ- is formed as shown in Figure 1-10. The distorted yttrium ions are simultaneously compensated for at the APBs and ferroelectric domain boundaries, which are energetically favoured[169]. Therefore, the APBs and ferroelectric domain boundaries are mutually interlocked.

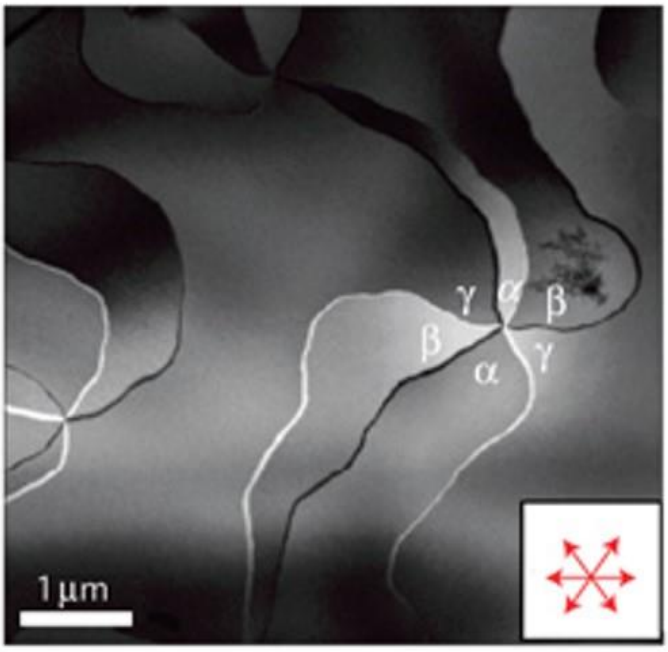

Figure 1-10 A dark-field TEM image shows six domains emerging from one point [161].

1.3. Polarisation switching kinetics under different external stimuli

Thermodynamic theory suggests that the Gibbs free energy G determines the stability of a phase[170, 171]. If one phase has lower G than the other, this phase is more stable. To initiate phase transformation, the energy difference between the original phase A and the resulting phase B, $\Delta G = G_A - G_B$, should be positive. Generally, the Gibbs free energy of each phase is a function of some thermodynamic variables, including electric field, magnetic field, mechanical loading, strain gradient, temperature, chemical composition and external pressure[170]. Therefore, phase transformation can result from a change in these variables.

1.3.1. Mechanical stimulation

While all ferroelectric materials are pyroelectric and piezoelectric materials, some ferroelectrics are also ferroelastic materials, in which the order parameter is associated with strain[172-174]. The role of strain in ferroelectric behaviour, such as ferroelectric switching and ferroelastic switching, is an essential aspect of ferroelectric sensors and actuators[175-177]. When mechanical loading is applied to a ferroelastic material, a non-Hookean hysteresis strain–stress curve will be observed. Such an elastic hysteresis shows the effect of polarisation switching between different ferroelastic states by mechanical loading. The first elastic hysteresis loop was reported in 1976 for the material $Pb_3(PO_4)_2$[170, 178]. Different ferroelastic states in $Pb_3(PO_4)_2$ result from the displacement of Pb inside its oxygen coordination by external stress[179-181]. Pb has short chemical bonds with two O atoms and it has long bonds with the other four O atoms. Such bonding structures between Pb and O atoms decrease the symmetry of the $Pb_3(PO_4)_2$ crystal from a trigonal structure to a monoclinic structure, generating different orientation strain states by varying the orientation of short bonds.

While the study of macroscopic behaviour showed a nonlinear hysteresis for the phase transition under mechanical loading, the mechanism behind this behaviour is attributed to polarisation and the domain-wall motion[182, 183]. Ferroelastic domain switching involves the

rearrangement of domains by applying external mechanical stress. Such switching associating non-180° domains is accompanied by stress.

However, phase transformation by applying external mechanical loading cannot be confirmed and many factors which affect the polarisation switching kinetics cannot be understood without microscopic observation of direct polarisation reversal[184]. Some techniques, including polarised light microscopy[185, 186], piezoresponse force microscopy[183, 187], scanning electron microscopy (SEM)[188, 189] and TEM[190], have been used to observe in-situ polarisation switching behaviour under external mechanical loading.

Piezoresponse force microscopy is a contact mode technique in which piezoelectric deformation is caused by applying voltage to a silicon nitride probe tip. An external electric field produced by an AC voltage bias can be directly applied by the scanning tip of the PFM for in-situ stimulating and imaging. The converse piezoelectric effect results from mechanical vibration, contributing to the contrasting morphologies of the polarisation domains. Kwanlae et al.[183] reported an in-situ compression test on a PZT ceramic with coexisting tetragonal and rhombohedral phases using a piezoresponse force microscope. Ferroelastic domain switching processes including the overwriting of lamellate-like domains were reported, confirming that the switching processes follow a positive work principle. Reichmann et al.[189] demonstrated a different ferroelastic switching mechanism in a polycrystalline $BaTiO_3$ sample. Phase transition with a banded twin structure changing to lamellar twinning was reported, suggesting the strong effect of grain orientation on domain switching kinetics. Gao et al.[190] reported 90° ferroelastic switching in a tetragonal PZT thin film using a TEM. Defects at the film/substrate interface were found to impede the mobility of domain walls under mechanical excitation.

Recent research has proposed that ferroelectric material possesses flexoelectricity[80, 191, 192]. Flexoelectricity is a property of the mechanical-loading-induced electric field owing to the

strain gradient of dielectric material. Lee et al.[192] showed that a strain gradient creates a strong imprint in the uniaxial direction and breaks inversion symmetry, generating an electric field from lattice deformations. Lu et al.[80] demonstrated that the strain gradient generated by the tip of an atomic force microscope can mechanically switch the polarisation of the nanoscale volume of a ferroelectric film. This work indicates that mechanical loading can also be used to induce 180° ferroelectric switching.

In summary, mechanical stimulation induces both 90° and 180° domain switching, providing uniform strain and strain gradient respectively. The domain switching process can be changed or impeded by various factors, including crystalline defects, crystalline orientation and material composition.

1.3.2. Electric fields

Polarisation in ferroelectric materials can be redirected and forced to align to a specific direction by applying an external electric field[175, 193]. Such polarisation switching is the origin of electric-field-induced phase transformation.

In the macroscopic view, the application of an electric field gives rise to the electric-polarisation hysteresis loop[42, 43]. The hysteresis loop assists in understanding how the applied electric field affects polarisation. When changing the strength of the applied electric field, the magnitude of the polarisation also changes allowing the remnant polarisation, coercive field and other electromechanical properties to be revealed[10].

The hysteresis loop changes with the direction of the external electric field relative to its crystalline orientation, suggesting that the polarisation switching process depends on the relationship between the crystallographic orientation and the direction of the applied external electric field. For example, for PMN-PT rhombohedral-phase single crystals, poling along [001]c results in a giant piezoelectric strain constant of d33 ≈ 3000 pC/N and a superior

electromechanical coupling factor of k33 > 90%[144]. When the poling direction is along [011]c, large transverse and shear piezoelectric properties (d32 and k32) are achieved[194]. Changing the poling direction to [111]c results in a significant shear piezoelectric strain coefficient of d15 ≈ 4000 pC/N and an electromechanical coupling factor of k15 > 80%[143]. These remarkable properties achieved by different poling directions are caused by the various polarisation rotation pathways. Initially, the rhombohedral-phase single crystal possesses polarisation along the eight <111>c directions. When an external electric field is applied along the [001]c, polarisation is forced to rotate from <111>c towards [001]c via either the MA or the MC phase, contributing to high levels of d33 and k33. The transverse and shear properties d32 and k32 benefit from polarisation rotation from [111]c to [011]c via the MB phase for electrical poling along [011]c. Nevertheless, a rhombohedral-phase material can be polarised into a single domain state without phase transformation if the electric field is applied along [111]c, resulting in excellent shear electromechanical properties.

Extensive efforts have been made to explore the effects of electric fields on ferroelectric material domain structures and diverse phenomena have been reported. These included the following investigations: (i) In-situ polarised light microscopy was used to show the polarisation directions and the positions of switched domains under electric field excitation[195], which closely adhered to the theoretical predictions for PMN-38%PT single crystals. (ii) An experiment on direct 180° ferroelectric switching that was conducted by applying AC voltage bias to a PZT thin film using atomic force microscopy[196] showed that no strain energy is associated with the ferroelectric switching that exhibits direct 180° polarisation redirection. (iii) Research[197] showed the voltage-controlled reversible creation and the annihilation of nanoscale non-180° ferroelastic switching without a synchronised ferroelectric 180° switching of the surrounding c-domain matrix in a PZT thin film using piezoelectric force microscopy. (iv) An in-situ investigation[198] reported a direct 180° ferroelectric switching along the [111] electric-

poling direction of a PZT thin film, while 180° ferroelectric switching as a result of successful ferroelastic switching was observed along [001] and [011]. (v) A retention loss (polarisation reversal) in PZT thin films after the retraction of the electric field was reported[199]. Further, the paper claimed that the capability of ferroelectric domain reversal is affected by the existence of defects in the thin-film/substrate interface that was observed using TEM.

These different reported phenomena about the effects of electric fields on ferroelectric materials suggested that polarisation switching kinetics is complicated and is affected by a number of factors, including electrostatics energy, domain (wall) energy, substrate constraint, crystal orientation and crystalline defects.

1.3.3. Heating

While normal ferroelectrics have a fixed temperature at the permittivity maximum, relaxor ferroelectrics have a diffuse temperature range of permittivity maximums with specific frequency dispersions. The temperature of the permittivity maximum—T_{max}—increases with the measurement frequency and the relationship is mathematically represented by the Vogel-Fulcher relation[200, 201]:

$$\omega = \omega_0 e^{\frac{-E_0}{k(T_{max}-T_f)}}$$

Here, ω is the measured frequency, ω_0 is the pre-exponential factor ~ 10^{13} Hz, E_0 is the activation energy, k is the Boltzmann constant, T_{max} is the temperature of the permittivity maxima and T_f is the freezing temperature upon which a frustrated polar-domain state forms[202-205].

The dielectric properties, reflected in the domain motion dynamic, are closely related to the temperature of ferroelectrics. Therefore, it is essential to study domain switching kinetics at various temperatures using in-situ techniques.

The domain dynamics of relaxor materials around the freezing temperature were reported by Craig et al.[200] using in-situ TEM. They found that the macro-domain structure changed to a micro-domain structure when the temperature was heated above T_f. When the temperature was higher than T_{max}, the diffraction contrast between the domains was lost because of high thermal energy introducing disorder to the system through polarisation fluctuations. The disappearance of diffraction contrast above T_{max} was not expected and required further in-situ investigation. The domain switching dynamic under electric poling is also temperature dependent. Mulvihill et al.[206] reported the domain dynamic upon cooling when a constant electric field was applied to relaxor ferroelectric single crystals. They found that the domain density decreased significantly with decreasing temperature.

These reports indicate the capacity for changing domain morphology, domain switching kinetics and internal system energy by applying heat flow to ferroelectric materials.

1.4. Outstanding issues to be addressed by this thesis

As seen from the literature review, ferroelectric materials demonstrate many remarkable properties, including hysteresis under different external stimuli, which can be used in various advanced applications. To utilise these properties for devices, it is essential to explore the mechanism behind the hysteresis behaviour—domain switching kinetics—by applying different external stimuli. However, the understanding of the domain switching kinetics is still limited. Local polarisation in ferroelectric/ferroelastic materials can be redirected through the application of external stimuli. Polarisation switching occurs as a consequence of particularly inhomogeneous nucleation and the growth of differently oriented domains. Domain switching kinetics is influenced by combined external stimuli, including electric fields, mechanical loading, heating and the existence of different types of defects such as interfaces, vacancies and dislocations. These influences on domain switching kinetics will either benefit ferroelectric properties, which will be introduced in Chapters 3, 4, 5 and 6 or cause various problems in the

application of ferroelectric devices. Therefore, comprehensive understanding of how domain switching kinetics is affected by external stimuli and defects is of significant importance to ferroelectric devices. It is necessary to explore the various factors that can affect the kinetics. As such, to comprehensively understand the kinetics and observe the structure–property relationship in real time, further investigations of ferroelectric materials using different in-situ techniques are necessary.

Reversible manipulation of ferroelectric domains at nanoscale resolutions will significantly enhance the electronic memory storage density and the ability for frequent rewriting in thin-film ferroelectric devices. Ferroelectric domain manipulation can be achieved using techniques that apply heat, mechanical stress or electric bias. Although increasing temperature[159, 207] and applying strain[190], both introduce additional energy that may lead to atomic redistribution; thus, it is difficult to use the two methods for precise ferroelectric domain manipulation. Applying an external electric field is the easiest way to manipulate ferroelectric domains at an ambient temperature. However, the contact mode causes serious abrasion of the probe tip and the ferroelectric materials[208]. In my study, I propose to use a high-energy electron beam with an omnidirectional electric field for non-contact, nanoscale ferroelectric domain manipulation. My investigation suggests that a local accumulation of trapped charges contributes to the local omnidirectional electric field that determines domain configurations. The results also indicate that caution is needed in the electron microscopy investigation of ferroelectric domain structures to avoid any artificial effect caused by electron-beam illumination.

In ferroelectric memory devices, the existence of ferroelectric and ferroelastic backswitching causes significant data loss and thus affects the reliability of data storage. Therefore, it is vital to find a way to overcome this long-standing problem. In my study, I conduct in-situ experiments to propose an approach that takes advantage of the mechanically

reversible and irreversible states of ferroelastic domain configurations for advanced bit writing and reading for non-volatile memories. Because this approach does not consider the ferroelectric domain polarisation direction, it overcomes the backswitching problem and broadens the types of ferroelectric materials for non-volatile memory applications.

Understanding ferroelectric domain switching behaviour under electrical loading is extremely important for the application of ferroelectrics in memories, actuators and nanoelectronic devices. Mechanical loading is expected to significantly affect domain switching kinetics under electrical loading. Therefore, the application of mechanical loading during electrical poling adds one more degree of freedom for domain manipulation and provides an appealing possibility for extensively improving ferroelectric device performance. Since polarisation switching usually occurs in nanoscale domains, to reveal the mechanisms behind the observed macroscopic behaviours, it is critical to understand at the microscopic level how combined external stimulations affect domain switching kinetics. In my study, I combine in-situ microscopy characterisation and phase-field modelling to reveal the nature of domain switching under electrical loading with and without mechanical loading in ferroelectric single crystals.

In various types of applications, ferroelectric materials are often subjected to different levels of mechanical loading, either intentionally in the design of a device itself or unintentionally by environmental stresses. Several studies[209, 210] have found that by changing the applied stress from compression to tension, the remnant polarisation increases and the coercive field decreases, while other studies[211] have shown opposite results. Comprehensive understanding of dynamic microscopic structure and domain kinetic behaviours is essential to resolve the controversy resulting from these conflicting reports. However, the mechanism behind domain switching kinetics under mechanical loading remains unclear because of the difficulty of extracting microscopic details in both mechanical compression and tension

experiments. Here, I conduct in-situ straining TEM experiments to explore ferroelastic domain switching kinetics by applying mechanical compression and tension to ferroelectric single crystals for a large stress range extending from lower to higher than the coercive field. The results provide significant new insights into polarisation switching kinetics and expand our fundamental comprehension of domain behaviour.

Chapter 2

Experimental techniques

2.1. Brief history of electron microscopy

In 1925, French physicist de Broglie proposed that microcosmic particles possess both wave-like characteristics and particle characteristics[212]. He suggested that wave–particle duality exists in multiple kinds of matter, including visible light, microcosmic motive substances and electromagnetic waves. Because the wavelength of high-energy electrons is much shorter than visible light, electrons were first considered for imaging small objects that are invisible under visible light. In 1926, German physicist Busch developed a theory[213, 214] that claimed that a symmetric-axis magnetic field could potentially be used to change the kinetic path of electron flow. This is the original idea of utilising magnetic fields as electron lenses to diverge (or converge) electron flows (electron beams).

Knoll and Ruska built the first TEM in Berlin in 1932[215]. It possessed an accelerating voltage of 70 kV and a magnification of only 12X. Although the magnification was not comparable to that of an optical microscope, the invention paved the way for using a magnetic lens and an electron beam for imaging. A more powerful TEM was built by Ruska one year later[216]. An image of fibres under 10,000X magnification was obtained, indicating that the electron microscope possesses a better magnification than the optical microscope. The first commercial TEM—model Metropolitan-Vickers EM1—was manufactured in the UK in 1936.

The development of the SEM was not as easy as that of the TEM. The first theory and idea for building an SEM was developed by Knoll in 1935[217]. However, it was not until 1965 that the first commercial SEM was manufactured. Thereafter, the development of the technology and resolution of the SEM progressed much more rapidly than before.

The wave theory of substance was developed by Schrodinger[218] and Heisenberg[219] in the early twentieth century. Since then, scientists have used the Schrodinger equation to solve problems with the fast-scattered electron beam. Among these scientists, Bethe[220] successfully developed a theory to interpret contrasting dynamic diffraction images using the Schrodinger equation.

Today, the function of electron microscopes has enormously improved as they are in high demand by various disciplines. With state-of-the-art electron microscopes, it is now possible to comprehensively explore the mechanisms behind macroscopic phenomena.

2.2. Introduction to electron microscopy techniques

The principle of electron microscopy is based on the interaction between high-energy electrons and materials. When an electron beam passes through a specimen, different types of interaction products, including auger electrons, backscattered electrons, secondary electrons and characteristic x-rays, are generated. This interaction is schematically drawn in Figure 2-1.

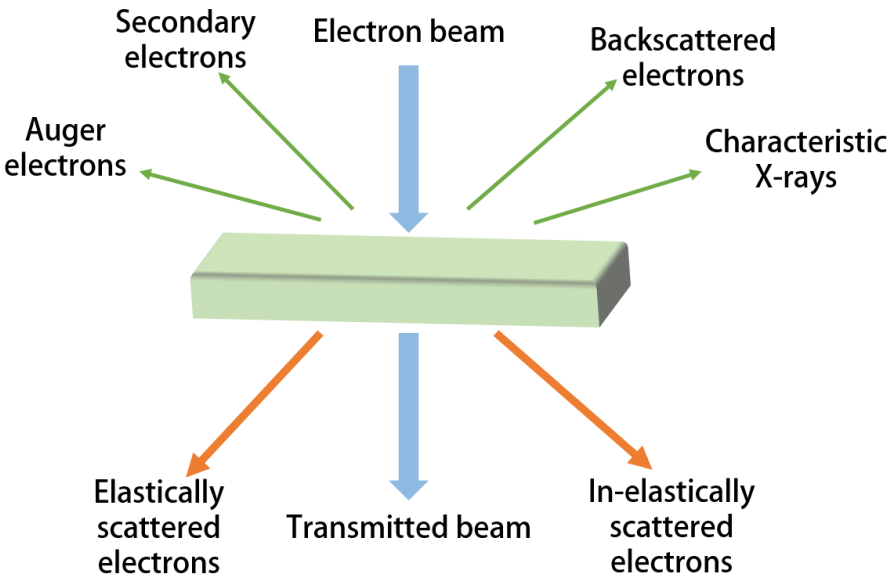

Figure 2-1 Interaction between an electron beam and a specimen.

2.2.1. Scanning electron microscopy

Scientists can acquire structural and compositional information by collecting and analysing electron–specimen interaction products. In SEM, backscattered electrons and secondary electrons are used for imaging to acquire structural information and the surface morphology of materials while characteristic x-rays are collected for compositional analysis[221, 222].

A typical SEM has a complicated structure that generally consists of several important parts including a vacuum system, an electron gun, magnetic lenses, various signal detectors, a sample stage and a control system. The principle of an SEM is schematically shown in Figure 2-2. Electrons are generated from an electron filament and accelerated through the voltage difference between a cathode and an anode in the electron gun. A high-energy focused electron beam is then formed by focusing the electrons through a series of magnetic lenses. After passing through the scanning coils, the electron beam is directed onto the specimen.

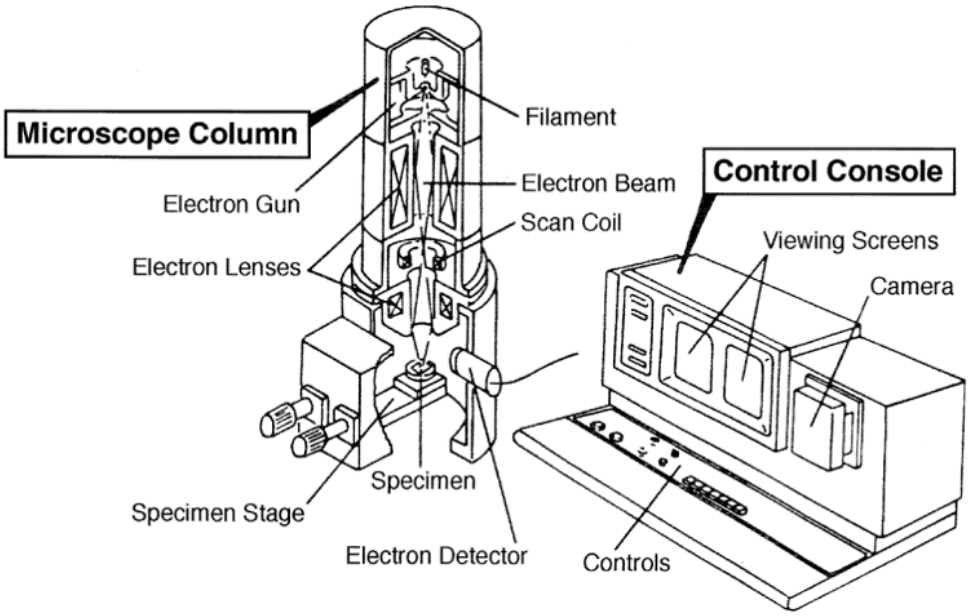

Figure 2-2 The working principle of an SEM [223].

When the electron beam interacts with a specimen on the surface, some secondary electrons are generated. These secondary electrons are weakly bound, conduction-band electrons that possess relatively low energy. Some secondary electrons are absorbed by the specimen, while others escape from the specimen's surface. The escaped secondary electrons that carry information about the sample surface will then be captured by a secondary electron detector that is located 52° from the angle of the microscopic column. The collected secondary electrons contain information about the surface morphology of the specimen, which can be seen from the image variation. As the generation of secondary electrons' signal is affected by the topography of the specimen surface, the edges of the sample surface produce more secondary electrons, which make them brighter than other parts of the image.

SEM possesses a large depth of field that allows for the acceptable focus range of the sample. Within this focus range, different lengths of depth can be focused at the same time. Taking advantage of the large depth of field, the SEM can be used to take three-dimensional images for some materials with nanoscale dimensions.

2.2.2. Focused ion beam

Electrons that are used for imaging in the SEM and TEM are not the only sources that can be accelerated and focused by electric and magnetic fields. Ions, which are atoms with net positive or negative electrical charges arising from unequal numbers of total electrons and protons, can also be accelerated and focused by electric and magnetic fields. The mass of the lightest ion is almost 2000 times higher than that of an electron, while the heaviest ion can be 500,000 times heavier. While the relatively light-weight electrons can result in the emission of secondary electrons by interacting with the sample surface, heavy ions can be used to directly modify or mill the specimen surface by sputtering atoms or molecules from the surface. By carefully controlling the parameters of an ion beam, precise nanoscale milling is possible to perform. Further, when an ion beam interacts with a sample surface, secondary electrons are generated to allow for the production of high-spatial-resolution images.

The focused ion beam (FIB) technique has been widely used in material science and technological applications over the past decade because of its high-resolution imaging and nanomachining capabilities[224]. Most commercial FIBs supplement the Ga-ion's FIB column with an additional SEM column to form a dual-beam platform (FIB-SEM) for simultaneous electron-beam imaging, electron-beam deposition and ion-beam milling. The first FIB instrument was developed based on the field-ion microscope[224] and advanced high-resolution liquid-metal ion sources. Later, FIB was used for mask and circuit repair in the semiconductor industry of the 1980s. FIB has been used in research laboratories since the 1990s.

The liquid-metal ion source is the most widely used ion source type in commercial FIB systems[225]. Among all liquid-metal ion sources, the Ga-based blunt needle source is widely used because of its relatively low melting temperature and high stability. The working principle of the FIB system is illustrated in Figure 2-3. When ions are generated by the gun, they are trained to a beam and focused on the sample using a condenser and an objective lens. By

switching different beam-defining apertures, the beam diameter and current can be chosen. The imaging resolution and machining precision are determined by the size and shape of the beam intensity profile—in most cases, the smaller the beam diameter, the higher the resolution and milling precision. After the interaction between the ion beam and the specimen, the emitted secondary electrons, x-rays and sputtered particles can be collected for imaging purposes.

Electrons from the electron beam in the FIB-SEM system or the secondary electrons generated by the beam–specimen interaction can be used to crack hydrocarbon precursor gases, resulting in electron deposition in some conductive material, including tungsten, platinum and carbon[224]. This local deposition of conductive material allows for an in-situ lift-out technique for micro/nano manipulation in the FIB-SEM chamber, which makes the FIB instrument more functional for materials scientists.

2.2.3. Transmission electron microscopy

There are normally five important parts in a commercial TEM: power supply, vacuum, lighting, imaging and recording systems. The basic principle of the TEM is similar to that of the optical microscope, though the light source is electrons instead of the visible light used for the TEM. The resolution of an optical microscope (~200 nm) is determined by the wavelength of the light source. Compared with visible light, high-energy electrons possess much shorter wavelengths, providing theoretically ultrahigh resolution for the TEM of smaller than ~ 0.1 nm. Owing to the ultrahigh resolution, the TEM has arguably become the most powerful structural characterisation tool for material science and engineering[226].

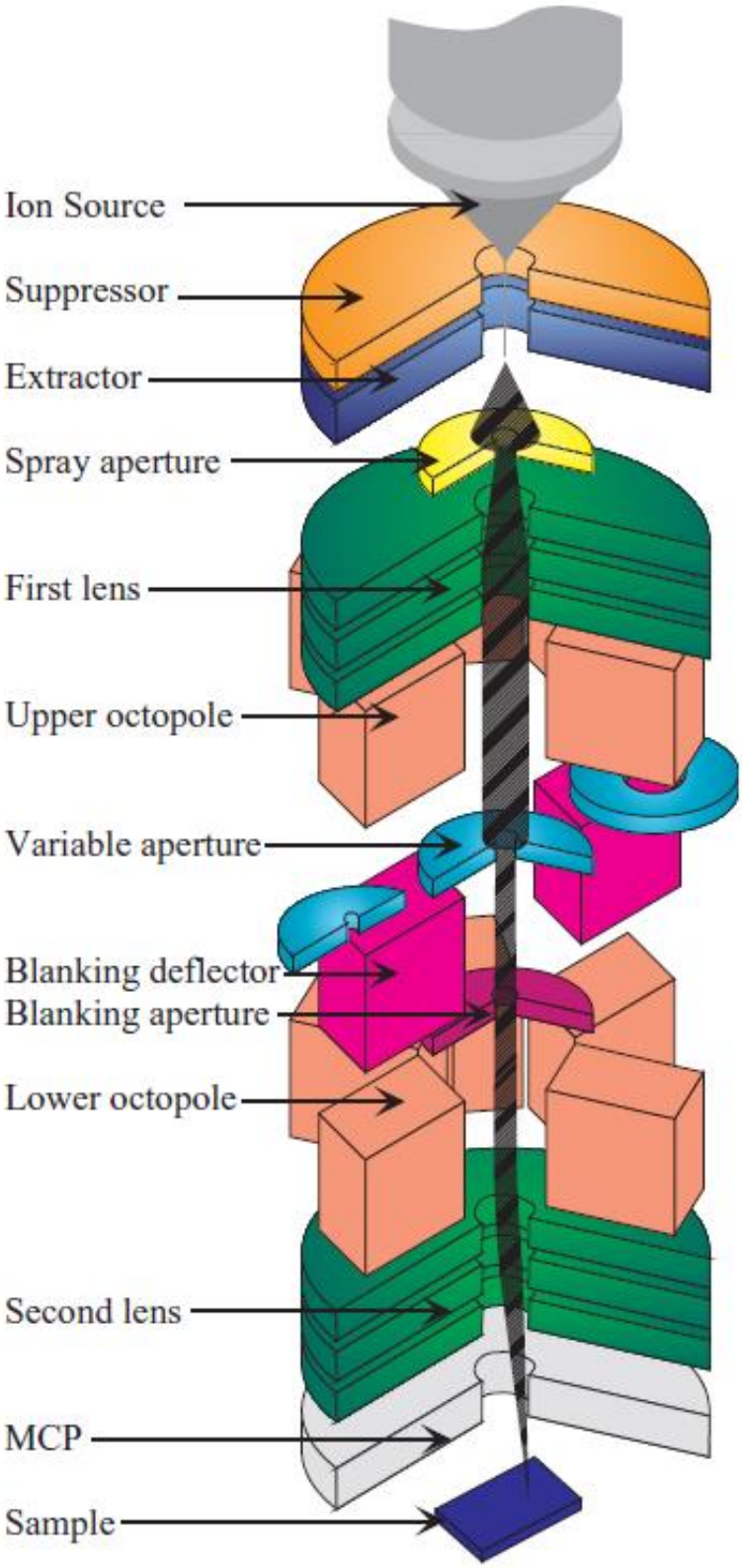

Figure 2-3 The working principle of a FIB [227].

In the lighting system, electrons are generated by an electron gun. Electron sources that are used in the electron gun can be either thermionic sources or field-emission sources. Generated electrons are accelerated by voltages ranging from 80–1000 kV in the gun, forming high-energy electron flows. By travelling past the condenser lens, the high-energy electron flow is refined to an electron beam and focused onto the specimen. To enable electrons to forward scatter and/or transmit through the specimen, a thin specimen thickness of less than a few hundred nanometres is usually required for conventional TEM imaging, while high-resolution TEM imaging necessitates a thickness of smaller than 100 nm. By detecting the forward scattering and/or transmitting electrons, structural information for the specimen can be attained. After passing through the specimen, the electron beam is focused by the objective lens and magnified by the intermediate lens. The image and diffraction pattern are then projected onto the imaging screen.

In addition to imaging the real space of the specimen, information about crystal structures from the reciprocal space is also captured through electron diffractions. In modern TEMs, the imaging mode and the diffraction mode can be easily substituted for one another. Figure 2-4 illustrates the electron paths for both the imaging and the diffraction modes.

Two special planes, the back focal plane and the image plane, form in the TEM column. The diffraction pattern is located on the back focal plane, which contains structural information about materials in the reciprocal space. An objective aperture can be used to allow one (or several) of the scattered beams to pass through for imaging. A dark-field image is formed using a scattered beam. A bright-field image is formed using the transmitted beam. An area of interest consisting of desired information can be selected by inserting an intermediate aperture. A subsequently obtained diffraction pattern is termed the selected area’s electron diffraction pattern. Finally, an image or an electron diffraction pattern can be seen on the viewing screen

after the object in the image plane or the back focal plane has been magnified by the projection lens.

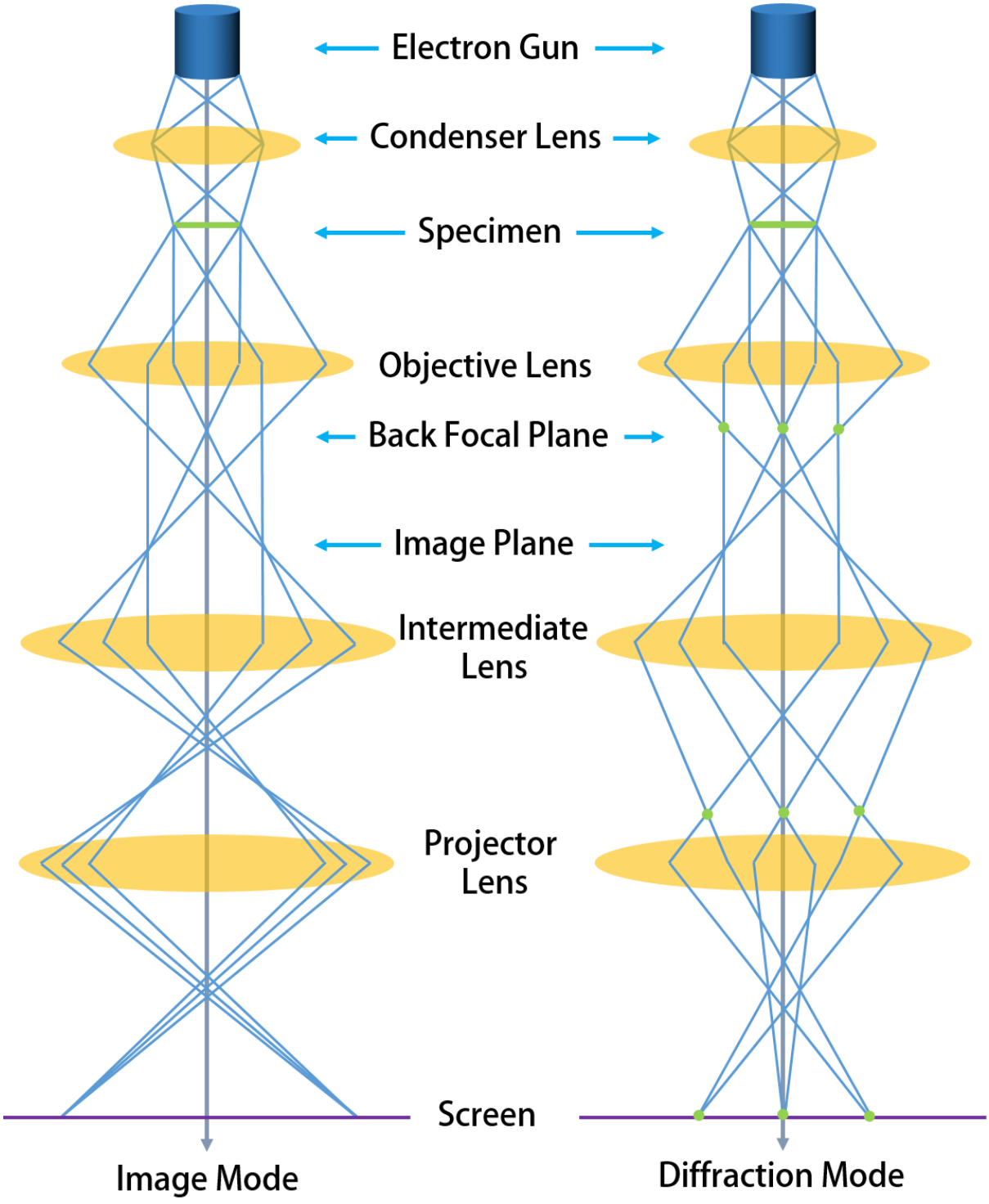

Figure 2-4 The electron paths for the imaging and the diffraction modes in a TEM.

Photographic films were once used to record images. Today, images can be observed and recorded by a high-resolution charge-coupled device (CCD) camera. By using a state-of-the-art CCD camera, in-situ TEM experimental processes can be video recorded to understand the dynamic structural evolution of materials under various conditions.

While TEM has been a powerful tool for the structural characterisation of materials and biological specimens, a number of problems exist in the current TEM system. The preparation of TEM samples is a time-consuming process because the sample thickness is usually restricted to less than a few hundred nanometres. Within this thickness range, most oxide materials, including multiferroic materials, can easily be destroyed. Special precaution is required to avoid physical and chemical destruction during the sample preparation process. In addition, structures and/or chemical compositions that are sensitive to the electron beam can be altered or damaged by overexposure.

2.2.4. Scanning transmission electron microscopy

A scanning transmission electron microscope (STEM)[228] combines the principles of SEM and TEM and can perform as either type of instrument. The state-of-the-art aberration-corrected STEM is capable of providing information on elemental composition and electronic structures with ultrahigh resolution—it has the capacity to capture a single atom[229, 230]. The STEM can form a focused electron beam that scans across the sample and images by detecting electronic signals—which is similar to a SEM. However, contrary to that of SEM, the specimen used in STEM is a thin specimen, allowing for transmission modes when imaging and leading to improved spatial resolution.

Different detectors in the STEM provide different complementary views of materials. One advantage of the STEM is that it has multiple detectors operating simultaneously to acquire the maximum possible amount of information. Compared with an SEM, which works

at relatively low voltages, an STEM operates at much higher accelerating voltages between 80 and 300 kV. Increases in accelerating voltage lead to more successful specimen penetration and decreased electron wavelength, allowing for higher spatial resolution and for the observation of actual atomic configurations.

The working principle of an aberration-corrected STEM is shown in Figure 2-5. After they are generated and accelerated by the electron gun, electrons are focused onto the specimen by condenser lenses and an objective lens. The electron beam scanned across the sample using a set of scan coils. An objective aperture is used to limit the maximum angle of the scanning electron beam. Several detectors are used simultaneously to provide different complementary information and to capture different signals for forming different types of STEM images. The annular dark-field detector is used to exclude the transmitted beam and to collect scattered electrons to form dark-field images. The post-specimen lenses outside the incident beam cone can be used to change the inner angle of the annular dark-field detector. Changing the inner angle enhances the contrast of the atomic-number-dependent image. Images produced by high-angle scattered electrons, which are collected by the angle-changed annular dark-field detector, are called high-angle annular dark-field (HAADF) images or Z-contrast images.

HAADF images have been widely used to analyse crystal structures, domain structures and compositional variation in different materials because of their highly sensitive contrast to the average local atomic number[165, 184, 231].

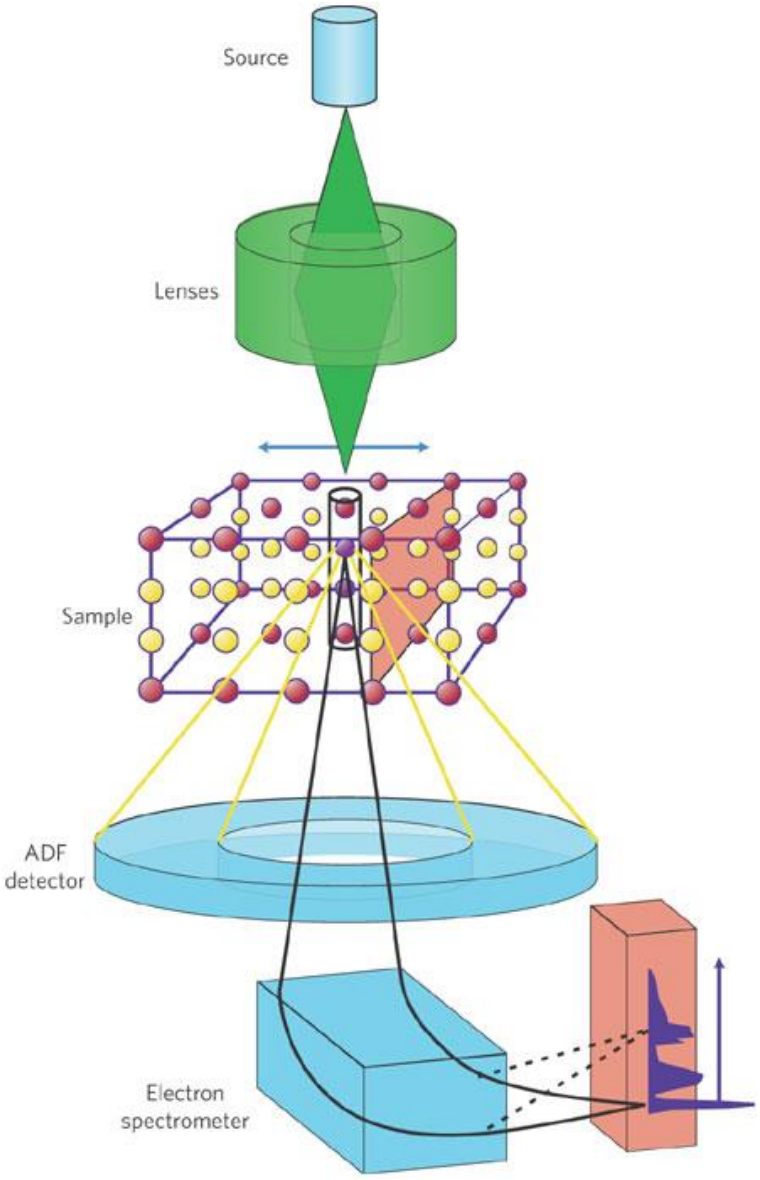

Figure 2-5 The working principle of a STEM [232].

2.3. In-situ nanomechanical–electrical testing system

To investigate and accurately analyse how domain switching kinetics is affected by external stress and bias and different types of crystalline defects, four essential requirements have to be satisfied[233]: (i) the nature of pre-existing defects has to be clearly characterised; (ii) accurate measurement of the time-forces displacement relationship is necessary for the investigation of the mechanical loading effect on domain switching kinetics; (iii) adequate accuracy of current and voltage measurements is needed to analyse the effect of external

electrical bias; and (iv) real-time structural observation of experimental processes for dynamical investigation is necessary.

Many techniques have been used to investigate domain switching behaviours in ferroelectric/ferroelastic materials, including piezoresponse force microscopy[234-236], polarised light microscopy[195, 237], x-ray diffraction[238] and time-resolved photoemission electron microscopy[239]. Recent advances in in-situ TEM techniques have allowed for direct investigation of domain switching kinetics with ultrahigh spatial and temporal resolution[145, 184, 190]. With in-situ TEM techniques, it is now possible to simultaneously apply multiple types of external stimuli to ferroelectric/ferroelastic materials and to observe the corresponding polarisation switching behaviour in real time.

The first in-situ deformation experiment using a contact probe in a TEM was conducted in 1970[240]. Following this, in-situ deformation techniques have developed rapidly and the actuated piezo-driven diamond indenter has been used routinely. Advanced depth-sensing transducers, accurate displacement-control feedback and the capability of connecting a conductive indentor to an electrical characterisation module have increased the sensitivity of deformation experiments and allowed for simultaneous electromechanical characterisation. Recently, miniature and commercialised in-situ TEM testing devices have been developed by Hysitron© and NanoFactory© and have been extensively used for in-situ TEM mechanical and electrical tests.

2.3.1. The PI 95 PicoIndenter

The PI 95 TEM PicoIndenter is the world's first fully fledged depth-sensing indenter, developed by Hysitron, which allows for the real-time observation of electromechanical testing inside a TEM[241].

The combination of a micro/nanomechanical testing system and a high-resolution TEM facilitates observation of the mechanical responses of ferroelectric materials at micro/nanoscales as well as the time synchronisation between load-displacement curves and their corresponding structural evolutions. This powerful capacity makes it possible to realise real-time observation of domain switching kinetics under external mechanical loading. The successful integration of the PI 95 PicoIndenter with an electrical characterisation module (ECM) even provides a solution for simultaneous in-situ mechanical and electrical loadings. The Hysitron PI 95 PicoIndenter TEM holder and an enlarged image of the front end are shown in Figure 2-6. Via a path between the conductive probe and the sample, an electrical bias can be applied for the continuous measurement of electrical signals as a function of the applied force to and the displacement of the probe. Such electrical testing can also be used to achieve a comprehensive understanding of the electromechanical properties of micro/nanostructures.

Figure 2-6 The PI 95 TEM PicoIndenter holder[241].

2.3.2. Push-to-pull device

The potential applications of microscale/nanoscale ferroelastic materials have attracted considerable research interest. However, understanding the mechanical behaviours and ferroelastic domain switching mechanisms for such small-scale materials is no easy task because of the lack of appropriate techniques that can be applied in high-resolution microscopes. Compression testing—to gain better insight into mechanical behaviour using pillars or particles in an electron microscope—has been carried out in some research groups; however, there are few reports on tensile experiments in this area. To accommodate the requirements for the tensile testing of materials at small scales, a push-to-pull (PTP) device—an in-situ tensile apparatus that is designed by Hysitron to work seamlessly with the PI 95 PicoIndenter in TEM—is used.

The PTP apparatus allows for quantitative tensile load-displacement measurement as well as simultaneously real-time imaging of microstructural evolution. It can also serve as a strain sensor and an energy buffer as well as a device for force calibration.

Figure 2-7 shows an SEM image of a PTP device. In the figure, the ‘mobile’ part is connected to the ‘fixed’ part via four arms. A specimen is fixed on the gap between the ‘mobile’ and the ‘fixed’ platforms, as depicted within the red-coloured circle. By applying a compression force to the front end of the ‘mobile’ part, a tensile stress is applied to the specimen.

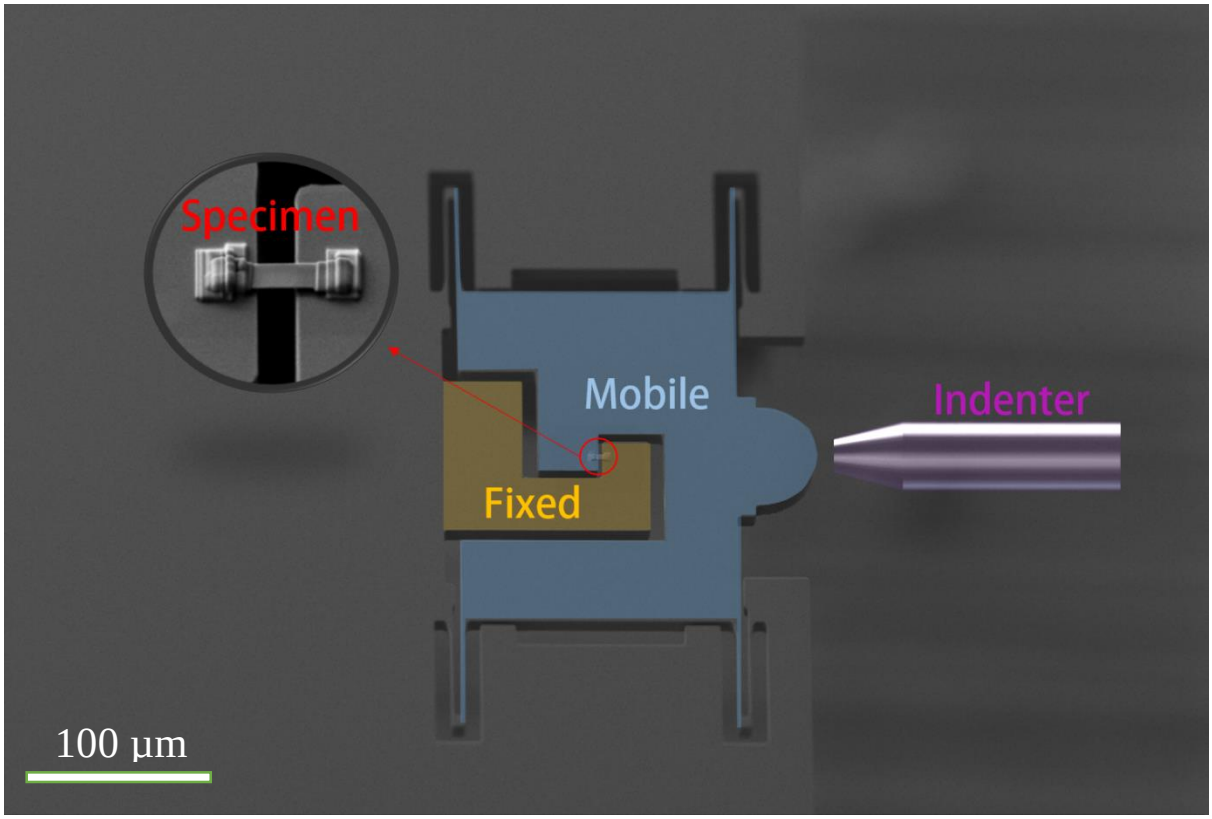

Figure 2-7 A SEM image of the PTP device.

2.4. Specimen preparation for electron microscopy

2.4.1. TEM specimen preparation

Thin foil specimens are required for electron-beam transmission during TEM observation. A sample thickness of less than a few hundred nanometres for low-resolution TEM images and less than a hundred nanometres for high-resolution TEM imaging is necessary, as discussed in Section 2.2.3.

For ferroelectric single-crystal TEM samples, an ion-beam thinning method is used. The specimen-preparation procedure is as follows:

(i) Use a diamond scribe to cleave a sample into small pieces 1 mm wide and 3 mm long. Clean the cleaved specimen using acetone and ethanol to remove contamination on the specimen surface.

(ii) Fix a cleaved specimen to a tripod insert with the desired crystal orientation facing up and perpendicular to the tripod insert using superglue. Wait for 20 minutes until the superglue is cured. Fix the tripod insert onto the tripod and adjust the angle of the tripod to ensure the top flat surface of the sample runs parallel to the surface of the grinding plate. Polish the specimen gradually with 30 µm, 15 µm, 9 µm, 3 µm and 1 µm diamond lapping films and water until the scratches on the surface are minimised and the surface becomes as shiny as a mirror. Place the specimen into acetone to dismount it and clean the specimen with ethanol.

(iii) Cleave a Si wafer to the same size as the tripod insert with a diamond scribe. Fix the Si wafer onto the tripod insert using superglue and wait for 20 minutes until it cures. Adjust the angle of the tripod and polish the Si wafer to ensure that the surface of the Si wafer runs parallel to the surface of the grinding plate. Fix the polished specimen onto the Si wafer using superglue with the polished side facing the wafer. Wait for a night to ensure that the superglue has perfectly cured.

(iv) Adjust the angle of the tripod to polish to a wedge shape. Polish the specimen gradually using 30 µm, 15 µm, 9 µm, 3 µm and 1 µm diamond lapping films and water. Keep polishing until part of the specimen disappears. Dismount the sample using acetone and clean the sample properly using ethanol. Fix the specimen onto a copper ring using epoxy and leave overnight to cure.

(v) Fix the specimen onto the stage of the Gatan 601 precise ion-beam polishing system. Fill the cooling chamber with liquid nitrogen to prevent damage or contamination that can be caused by the energy transformation during the thinning process. Set the Argon ion energy to 3.5 keV while maintaining the

current between 10 μA to 15 μA. Use a double beam with one gun positioned at the top and the other at the bottom. Set the inclination angle—the angle between the gun and the specimen surface—to seven degrees. The thinning duration depends on the sample thickness and will generally last for around three hours. After some materials from the edge of the specimen are removed, the specimen can be taken out for observation under the TEM.

2.4.2. In-situ nanomechanical–electrical testing specimen preparation

The Zeiss Auriga SEM-FIB dual-beam system is used for preparing in-situ nanomechanical–electrical testing specimens. The specimen-preparation procedure is as follows:

(i) Mechanically polish a bulk specimen to a thickness of ~ 1 μm on its edges using the specimen-preparation procedures (i)–(iv) provided in Section 2.4.1. Fix the specimen onto a Pi 95 PicoIndenter TEM mount using carbon tape and fix the mount onto a 36° pretilt SEM stage with carbon tape and conductive silver paint.

(ii) In the SEM-FIB dual-beam system, mill a long bar with dimensions of 70 μm × 9 μm × 1 μm (length × width × height) from the thin edge of the specimen. Transfer the long specimen bar to a pre-cut copper platform using a tungsten manipulator. Use platinum deposition to fix the specimen bar onto the copper platform as shown in Figure 2-8.

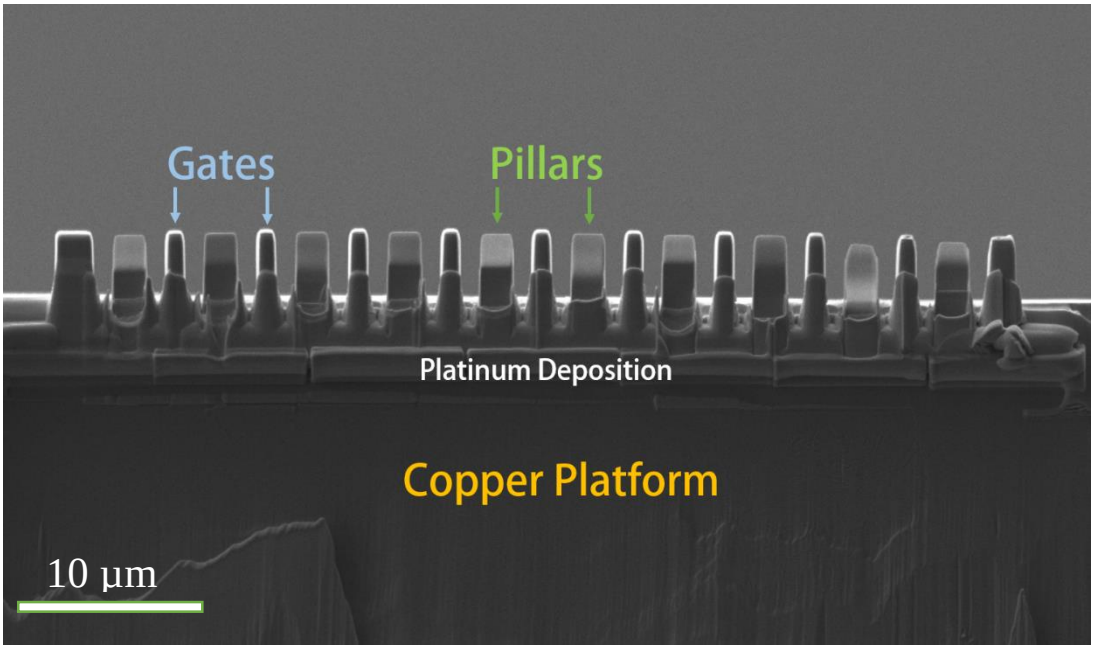

Figure 2-8 An SEM image of the specimen setup on a copper platform.

(iii) Coarse mill the pillars from the long bar using 30 kV and 50 nA to the dimensions of 2 µm × 3 µm × 0.4 µm (length × width × thickness). Between two neighbouring thin pillars, a thick pillar should be left that effectively prevents material redeposition from one pillar to another during the FIB processing. Fine mill the pillars using 10 kV and 10 nA to the dimensions of 2 µm × 3 µm × 0.06 µm.

2.5. Phase-field modelling

Microstructures that are compositionally and structurally inhomogeneous will arise during the processing of materials. Microstructural evolution—including chemical reactions and phase transformation—is commonly observed in different material-related areas. In many situations, there exist phases with different compositions, structures (including different structural, electrical or magnetic domains), spatial distributions, grain orientations and structural defects in materials. Such structural variants normally possess nano-/microscale intermediate mesoscopic length scales. The physical properties of materials are determined by

microstructures that consist of different sizes, shapes and other spatially distributed structural features.

Microstructural evolution takes place under different external stimuli such as electrical biases, mechanical loading, heating, cooling and magnetic fields. Evolution occurs to reduce the total free energy in a system, which includes elastic strain energy, interfacial energy, electrostatic energy and chemical free energy. Today, a number of approaches are used to model the microstructure evolution. A conventional approach is to treat regions that separate compositional or structural domains as mathematically sharp interfaces. The interfacial velocity of the sharp interface is used as part of the boundary conditions or calculated for interfacial mobility, which requires the tracking of the positions of the sharp interface. This approach is practical for one-dimensional systems, but impractical for three-dimensional microstructures. Recently, various types of microstructure evolutions have been modelled by a powerful method called the phase-field approach.

The phase-field approach is based on the diffuse-interface theory that was developed by Van der Waals and Cahn and Hilliard[242, 243]. The famous continuum, the Cahn-Hilliard nonlinear diffusion equation[244], and the time-dependent Ginzburg-Landau equation[245] are used to describe temporal microstructural evolutions in the phase-field approach. The phase-field approach describes the mesoscale microstructure phenomena and reveals sharp/thin interface information with a particular limit[246].

Today, phase-field models have been applied to many types of situations, including solidification[247], solid-state phase transformation[248], microstructure evolution under different external stimuli[190], dislocation dynamics[184] and crack propagation[249]. In these applications, the phase-field models treat both the structural/compositional information and the interfaces as a whole by using a number of field variables that are continuous across the interfacial regions.

Therefore, the interfaces are diffuse. Two types of field variables are used in phase-field models: conserved and non-conserved variables. The total free energy of a microstructure is then described by these conserved and non-conserved variables, as shown below[242, 243, 250]:

$$F = \int [f(c_1, c_2, c_3, \dots, c_{n-1}, c_n, \eta_1, \eta_2, \eta_3, \dots, \eta_{p-1}, \eta_p) + \sum_{i=1}^{n} \alpha_i (\nabla c_i)^2 + \sum_{i=1}^{3} \sum_{j=1}^{3} \sum_{k=1}^{p} \beta_{ij} \nabla_i \eta_k \nabla_j \eta_k] d^3r + \iint G(r - r') d^3r d^3r',$$

Here, *f* is a function of conserved variables (c_i) and non-conserved variables (η_i) and represents the local free-energy density. The values α_i and β_{ij} are the gradient energy coefficients. The first integral part of the equation describes the free energy from the short-range interactions, while the second integral part describes the total free energy from the long-range interactions, including electric and electrostatic interactions. By changing the field variables to the total free energy, phase-field models can be applied to variable fields as discussed above[250].

Chapter 3

The manipulation of nanoscale domain switching using an electron beam with omnidirectional electric field distribution

3.1. Introduction

Ferroelectrics—including typical ferroelectrics and improper ferroelectrics—results from the displacement of ions leading to spontaneous polarisation[161] where the internal electric field points towards a specific direction. Because of the electrically switchable nature of polarisation[251, 252] in ferroelectric domains, ferroelectric materials[153, 154, 253] are important for various types of electronic applications[77, 254, 255]. The interest in these materials comes not only from their unique intrinsic piezoelectric and pyroelectric properties, but also from the ability to precisely manipulate and control their ferroelectric domains at a micro-[256] or even nanoscale[257, 258]. Although increasing temperature[159, 207] and applying strain[190] both introduce additional energy that could lead to atomic redistribution, it is difficult to use these two methods for precise ferroelectric domain manipulation. Applying an external electric field[145, 167, 208, 259, 260] is the easiest way to manipulate ferroelectric domains at an ambient temperature. This can be achieved using scanning probe microscopes that work in contact mode, including the atomic force microscope[261], the piezoforce microscope[262] and the scanning nonlinear dielectric microscope [208]. For example, the scanning nonlinear dielectric microscope has been used to manipulate ferroelectric domains with a spatial resolution of ~ 10 nm[263]. However, the contact

mode leads to serious abrasions on the probe tip and the ferroelectric materials[208]. This problem can be overcome by introducing an electric field using a non-contact mode. The SEM, as a non-contact mode microscope, has been used for the manipulation of ferroelectric domains. In the SEM, electrons are trapped on the sample surface, forming a vertical electric field that changes the local polarisation. However, this method usually has a poor patterning resolution[162] as a consequence of non-uniform electron charges through the sample thickness. Nevertheless, the use of SEM to manipulate ferroelectric domains provides a way of using an electron beam (e-beam) for domain patterning.

Here, I demonstrate experimentally that an e-beam from the TEM can be used to precisely and reversibly control ferroelectric nanodomain morphology without contacting the material. An e-beam has been widely used for imaging and for the heating of local materials[264]. However, its capability for generating a controllable, local, omnidirectional electric field has not been explored. Compared with existing domain manipulation techniques, TEM presents an ultrahigh spatial resolution of smaller than ~ 0.2 nm and local nanoscale charges that generate an electric field along all directions, which potentially allows for nanoscale domain writing.

The $YMnO_3$ used in this experiment is improper ferroelectric with corner-sharing MnO_5 trigonal bipyramids tilted periodically[158]. The displacement of Y ions along the c axis or the <0001> direction occurs below the Curie temperature of ~ 1300 K[163], leading to the loss of crystal centrosymmetry. The periodic tilting of MnO_5 bipyramids enlarges the unit cell by three times and leads to so-called trimerisation transition[161], forming three types of antiphase domains: α, β, and γ. By mutually interlocking with positive and negative ferroelectric domains, six distinctive domains (α+, γ−, β+, α-, γ+ and β−) are alternatively allocated and form a vortex-like domain pattern[161]. Coupling the trimerisation and the displacement effect, $YMnO_3$ consists of only 180° ferroelectric domains with the opposite electric polarisation directions running along the c axis. Further, the high coercive field of $YMnO_3$ makes it an ideal

material for this study. With only 180° ferroelectric domain structures, the theoretical model on how the electric field is generated in the e-beam irradiation region can be easily set up. Since the coercive field for $YMnO_3$ is high, the domain can be manipulated manually by the e-beam in TEM.

$YMnO_3$ single crystals were grown by a floating-zone method in an infrared radiation furnace equipped with four 1000 W halogen lamps[265]. The feed rods for the crystal growth were prepared by the conventional solid-state method. Stoichiometric Y_2O_3 and Mn_2O_3 were weighed and mixed in an agate mortar, pressed at 200 MPa into pellets and then sintered at 1150 1C for 24 hours. The polycrystalline pellets were reground and pressed into cylindrical rods with diameters of 8 mm and lengths of 110 mm. The rods were hydrostatically pressed under a pressure of 70 MPa and then sintered at 1350°C for 20 hours. After sintering, a 20 mm long rod was cut to serve as the seed. The crystal growth speed was maintained at 5 mm, accompanied by a counter-rotation of the feed and seed rods at 20 rpm to ensure the efficient mixing of the liquid and homogeneous temperature distribution in the molten zone.

E-beam irradiation and TEM observation were carried out using a JEOL 3000F microscope operated at 300 kV. The dose rate for the e-beam was ~ $0.07 A/cm^2$—a low current density level that would not cause detectable sample damage even after prolonged (hundreds of seconds) e-beam illumination[266]. Before irradiation, the e-beam was spread and enlarged to prevent a major charge accumulation in the observed area. The e-beam was then focused on a small area of the required dimensions and the illumination time was recorded. Once the designated time had been reached, the e-beam was immediately spread to facilitate image acquisition and then shut down for 10 minutes to ensure enough time for the charge to evacuate from the sample. This process was repeated until the maximum designated time had been reached.

3.2. The manipulation of nanoscale domain switching using an electron beam

Figure 3-1 shows the evolution of a single domain under the e-beam in TEM and provides schematic diagrams that explain the evolution. Figure 3-1 (a) shows a typical dark-field TEM image of a vortex-like domain pattern viewed along a $<1\bar{1}00>$ direction and imaged using the $000\bar{2}$ diffraction spot (circled as the corresponding diffraction pattern).

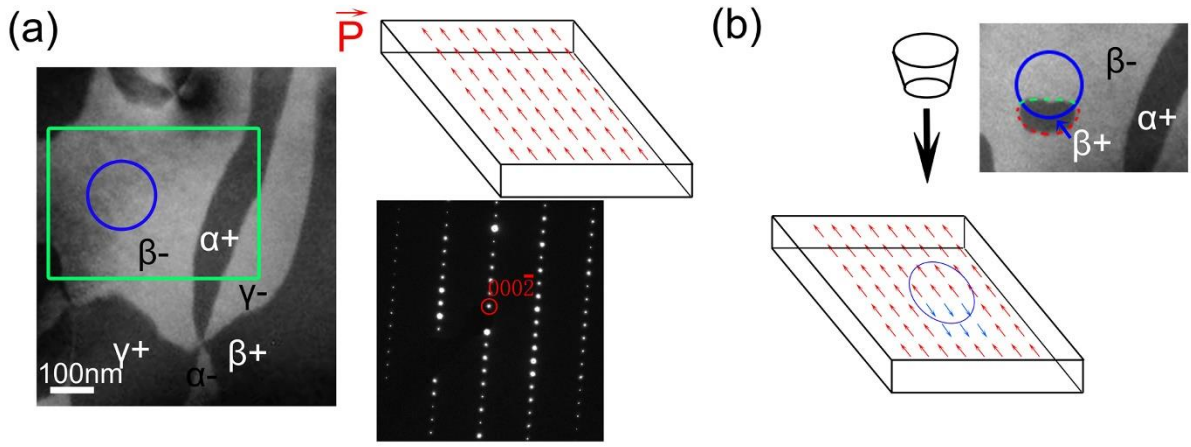

Figure 3-1 (a) A dark-field TEM image and its corresponding diffraction pattern. The area that was later subjected to local e-beam illumination was extracted from the green box. The blue circle indicates the exact e-beam illumination area. The polarisation of the white contrast domain (β−) is schematically drawn by red arrows. **(b)** After e-beam illumination, a newly formed β+ domain with dark contrast is seen and its corresponding polarisation is shown at the bottom.

Diffraction images of domains with positive and negative 180° polarisation appear contrasted as dark and bright respectively under kinematical diffraction conditions[267]. However, this contrast does not differentiate α, β, and γ domains with the same polarisation directions. Six distinctive domains (α+, β+ and γ+ in dark contrast and α–, β– and γ– in bright contrast) are shown in Figure 3-1 (a). The area indicated by a blue circle with a radius of ~ 60 nm in the β- domain was exposed to an e-beam. Figure 3-1 (b) presents an image of the area marked by the green rectangle in Figure 3-1 (a) after e-beam illumination. The hat-shaped area at the lower part of the blue circle was converted to dark contrast, indicating the redirection of

polarisation in the area—that is, the transformation from β− to β+. The redirection occurred because the component of the external electric field along the z-axis (E_z) in the hat-shaped area was equal to or larger than the coercive field (E_c) of the material and was in the opposite direction to the original polarisation.

Figure 3-2 (a) shows another vortex-like domain structure imaged using the $000\bar{2}$ diffraction spot. After e-beam illumination with a radius of ~ 100 nm as shown in Figure 3-2 (b), the α+ domain changed its morphology from the original protrusion shape (red-dashed lines) to a concave shape (green-dashed lines) through the shrinkage of the α+ domain at the lower part of the blue circle and the slight expansion of the α+ domain at the upper part of the blue circle, indicating that the areas at the upper part and the lower part around the e-beam illuminated zone evolved in opposite ways. Note that the area of domain switching at the lower part, around the e-beam-illuminated patch, is larger than that around the upper part of the e-beam-illuminated area in Figure 3-2 (b). This was determined by the original domain morphology and the position of the e-beam. Interestingly, the expanded β- and γ- domains did not merge, but were separated by a thin antiphase domain wall with dark contrast. An antiphase domain wall provides a defective area, avoiding the merging of the two neighbouring domains into one domain, which minimises the total system energy[166, 168]. The moving of the antiphase domain walls in this experiment is strong evidence of the mutual interlocking[161] of ferroelectric and antiphase domains in $YMnO_3$.

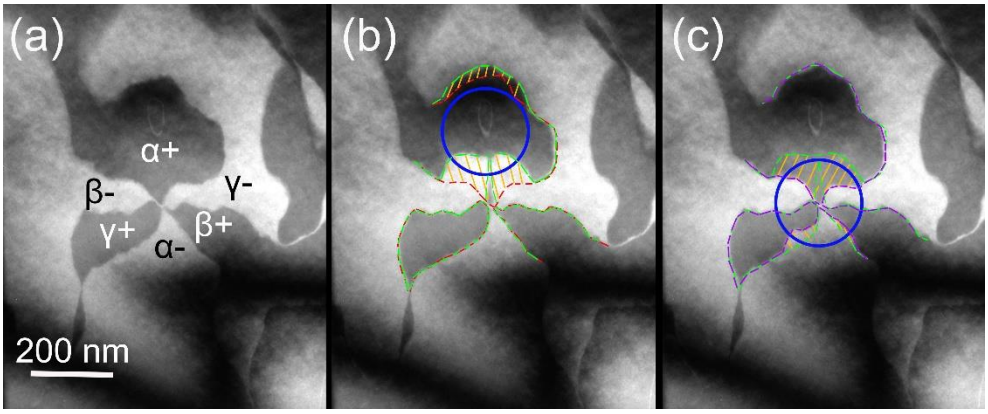

Figure 3-2 (a) A dark-field TEM image using the $\mathbf{000\bar{2}}$ diffraction spot. **(b)** Domain configurations after exposure to the e-beam. The blue circle indicates the e-beam illumination area. The red and green-dashed lines represent the domain boundaries before and after the illumination respectively. **(c)** Domain configurations after shifting the e-beam to a new position. The green and purple-dashed lines represent the domain boundaries before and after the illumination respectively.

Interestingly, a domain that was exposed to one end of the e-beam would return to its original structure if subsequently exposed to the opposite end of the e-beam. This was seen by moving the e-beam downward, as shown in Figure 3-2 (c). The previously expanded β− and γ− domains (the green-dashed lines) shown in Figure 3-2 (b) were then exposed to the upper part of the e-beam and this resulted in the shrinkage of the β− and γ− domains and the recovery of the α+ domain area (the purple-dashed lines) to almost its original shape. This result indicates that domain writing using the e-beam is erasable. At the same time, the α- domain that was exposed to the lower part of the e-beam was also expanded, which produced similar results to the expansion of the β− and γ− domains shown in Figure 3-2 (b). Note that the e-beam-induced domain morphology was stable and remained the same after one month. This stable switching is because of the creation and/or motion of ferroelectric and antiphase domain walls, which provided additional internal energy to resist the relaxation for nanoscale domain recovery.

3.3. Discussion

To explain these phenomena, a theoretical model was built. Figure 3-3 shows a schematic of an e-beam illuminating the blue circular area of a thin dielectric film in vacuum. While most of the electrons in the e-beam will transmit through the sample, a small amount of charges will be trapped in the thin film through mechanisms that will be discussed below, and the number of these charges will increase over time before an equilibrium is reached[268]. Both the transmitting electrons and the trapped charges contribute to a locally generated omnidirectional electric field.

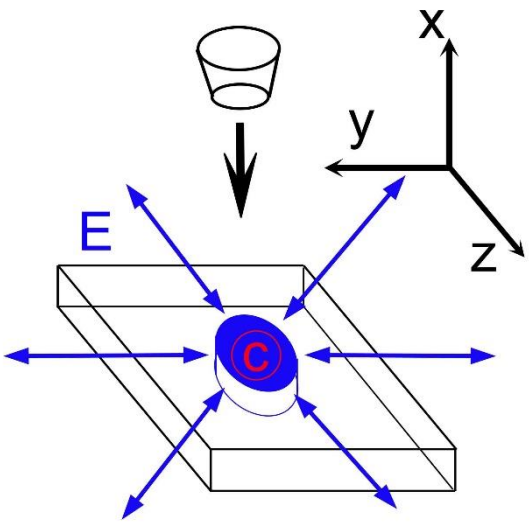

Figure 3-3 A schematic showing the omnidirectional electric field (E) induced by e-beam illumination in a thin-film specimen. The blue circle indicates the e-beam illuminated area and the letter 'C' represents charges.

In the following discussion, a situation is considered in which a ferroelectric material consists of only 180° ferroelectric domains and the polarisation directions are defined as parallel to the ±z-axis. Under these circumstances, a domain structure will be redirected only if the component of the external electric field along the z-axis (see Figure 3-3) is larger than the coercive field of the material and trained in the opposite direction to the original polarisation[161]. The external electric field components running along all other directions

perpendicular to the z-axis have no effect on redirecting the polarisation direction. Therefore, only E_z is considered below:

Theoretically, the z-axis component of the electric field (E_z) at any position (r, θ) can be expressed using the following equations:

$$E(r,\theta)_z = E_{z_1} + E_{z_2} \quad (3\text{-}1)$$

Here, E_{z_1} and E_{z_2} are the electric fields induced by the continuously passing electrons and trapped charges respectively.

3.3.1. Electron-beam intensity distribution in the illuminated area of the TEM

Understanding the e-beam intensity distribution is a prerequisite for the calculation of the electric field generated by the e-beam in TEM. The e-beam intensity distribution was measured by not placing a sample in the TEM. Figure 3-4 shows (a) an e-beam with a radius r = 48 nm and (b) the corresponding intensity profile across the diameter (the blue line in (a)) of the e-beam. Consistent with a previous report[268], the intensity profile in Figure 3-4 (b), which was extracted using a Gatan DigitalMicrograph, presents a Gaussian distribution with the small peak located at the centre of the e-beam. Given that the central peak is small and is in fact negligible compared to the overall e-beam intensity, it is a reasonable approximation to treat the e-beam-illuminated cylindrical volume as a uniformly charged body for continuously passing electrons. The intensities of e-beams with different radii were also measured and showed the same uniform distribution as in Figure 3-4 (b).

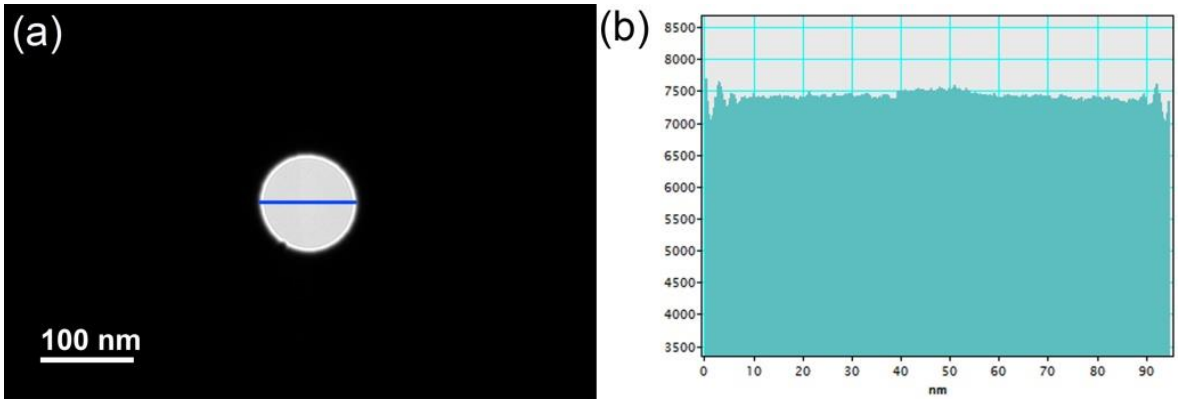

Figure 3-4 (a) An e-beam with a radius r = 48 nm. **(b)** The corresponding intensity profile across the diameter of the e-beam.

3.3.2. Electric field distribution

The following model describes the electric field generated in a thin film by e-beam illumination. The overall electric field comprises two parts—E_{r,θ_1} and E_{r,θ_2}—that are induced by continuously passing electrons and trapped charges respectively. E_{r,θ_1} and E_{r,θ_2} are discussed separately below.

3.3.2.1. The electric field induced by continuously passing electrons

As shown in Figure 3-5 (a), the specimen plane or the plane perpendicular to the e-beam direction is defined as the y–z plane. The e-beam illuminated volume of the thin film is charged and indicated using a pink colour. A cylindrical-shaped Gaussian surface[269] is built to include the charged volume in such a way that the symmetrical axis (the vertical green-dashed line in Figure 3-5 (a)) of the Gaussian surface coincides with that of the charged volume. The cylindrical-shaped Gaussian surface has its top surface (marked by a red solid circle) and its bottom surface (indicated by a blue-dashed circle) aligned with the top and bottom surfaces of the specimen respectively and, therefore, its side wall is of the same height as the specimen's thickness (see Figure 3-5 (a)). Based on Gaussian's law[269], the following equation can be achieved:

$$\oiint \overrightarrow{E_1} * d\vec{s} = \iint_{\text{top surface}} \overrightarrow{E_1} * d\vec{s} + \iint_{\text{bottom surface}} \overrightarrow{E_1} * d\vec{s} + \iint_{\text{side surface}} \overrightarrow{E_1} * d\vec{s} = \frac{Q_p}{\varepsilon_0} \quad (3\text{-}2)$$

Here, $\overrightarrow{E_1}$ is the electric field induced only by continuously passing electrons, ε_0 is the vacuum dielectric permittivity and Q_p indicates the total charge of the electrons passing through the enclosed volume. Because the electron beam can be treated as an infinitely long cylinder compared with the sample thickness and the top and bottom surface normals are parallel to the electric field, the integral results for both surfaces are zero. Therefore, equation (3-2) can be written as:

$$\oiint \overrightarrow{E_1} * d\vec{s} = \iint_{\text{side surface}} \overrightarrow{E_1} * d\vec{s} = \frac{Q_p}{\varepsilon_0} \quad (3\text{-}3)$$

Further, because the cylindrical side surface is perpendicular to the y–z plane:

$$\oiint \overrightarrow{E_1} * d\vec{s} = \int_0^{2\pi} E_{r,\theta_1} ds = \int_0^{2\pi} E_{r,\theta_1} * r h \, d\theta = \frac{Q_p}{\varepsilon_0} \quad (3\text{-}4)$$

Here, r is the distance between the origin and the point (r, θ); θ is the angle between the z-axis and r as shown in Figure 3-5 (b); h is the thickness of the thin film; and E_{r,θ_1} is the radial electric field at point (r, θ) on the y–z plane, which is not a function of the angle θ. Therefore, equation (3-4) can be simplified as:

$$2\pi r h \varepsilon_0 E_{r,\theta_1} = Q_p \quad (3\text{-}5)$$

Assuming uniform charge distribution within the e-beam-illuminated area, as discussed in Section 3.3.1, according to Coulomb's law[269]:

$$\begin{cases} Q_p = \rho\pi r^2 h & (r \le R) \\ Q_p = \rho\pi R^2 h & (r > R) \end{cases} \quad (3\text{-}6)$$

Here, ρ is the charge volume density and R is the radius of the illuminated area. When $r \le R$, the Gaussian surface should be built with a radius that is smaller than the radius of the illuminated area in Figure 3-5 (a).

The number of electrons continuously passing through the thin film is in a dynamic state of equilibrium. Its charge volume density is determined by the electron velocity:

$$\rho = \frac{I}{v\pi R^2} \tag{3-7}$$

Here, I is the current and v is the electron velocity.

Combining equations (3-5), (3-6) and (3-7), the electric field generated by continuously passing electrons is indicated by the following:

$$\begin{cases} E_{r,\theta_1} = \frac{rI}{2\pi v R^2 \varepsilon_0} & (r \leq R) \\ E_{r,\theta_1} = \frac{I}{2\pi v r \varepsilon_0} & (r > R) \end{cases} \tag{3-8}$$

The $YMnO_3$ used in my study has a hexagonal structure with only 180° ferroelectric domains. Assuming the polarisation directions run along the ±z directions, then only the electric field component along the z direction E_{z_1} contributes to the domain switching. The effective electric field at (r, θ) is, therefore, E_{z_1}:

$$E_{z_1} = E_{r,\theta_1}\cos\theta = \begin{cases} \frac{rI\cos\theta}{2\pi v R^2 \varepsilon_0} & (r \leq R) \\ \frac{I\cos\theta}{2\pi v r \varepsilon_0} & (r > R) \end{cases} \tag{3-9}$$

As shown in Section 3.3.1., the e-beam intensity has a Gaussian distribution[270] with a negligible small peak and can thus be approximately treated as having a uniform distribution. If the e-beam intensity remains constant, it is reasonable to assume that the rates of electrons entering and exiting the thin film are also constant and that, therefore, the number of passing electrons in the blue cylinder for the thin film is also constant.

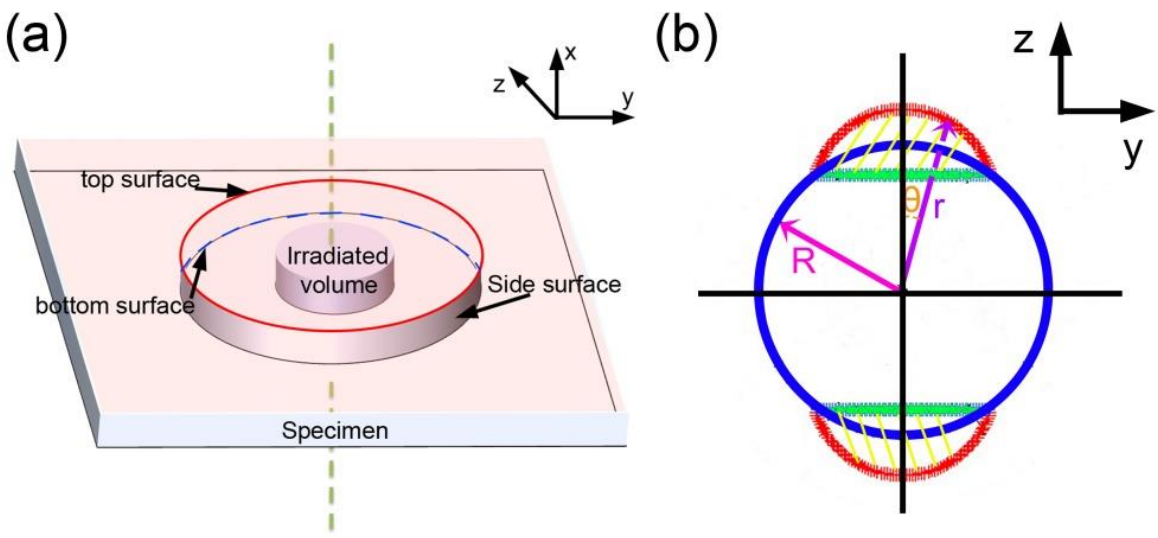

Figure 3-5 (a) A cylindrical-shaped Gaussian surface. **(b)** A theoretic model for the electric-field-magnitude distribution generated by continuously passing electrons. The blue circle indicates the e-beam illumination area. The red and green curves present the boundaries with E_z as equal to E_c; areas with yellow shadow show E_z as equal to or larger than E_c.

My experiments worked with the following values: the radius of the e-beam-illuminated area R = 100 nm, the e-beam current intensity I = 20 pA, the vacuum dielectric permittivity ε_0 = $8.85*10^{-12}$ C^2/m^2*N and the electron velocity v = $2.33*10^8$ m/s for the accelerating voltage of 300 kV. Using equation (3-9), the magnitude of the time-independent component—E_{z_1} = $2.43*10^{-7}$ kV/cm for r = 100 nm—is eight orders smaller than the coercive field of 40 kV/cm for $YMnO_3$[161] and therefore is negligible.

3.3.2.2. Electric fields induced by trapped charges (assuming that the electrons are uniformly distributed within the e-beam-illuminated volume)

Electrons in the e-beam were uniformly distributed within the illuminated area. Therefore, the trapped charges in the sample were initially assumed to be also uniformly distributed. For a thin-film sample with a thickness of ~ 100 nm, the uniformly charged area could be treated as a uniformly charged disc. The electric field E_{r,θ_2} for a uniformly charged disc on the y–z plane is derived as[271]:

$$E_{r,\theta_2} = \frac{dV_{r,\theta_2}}{dr} = \begin{cases} \frac{Q_t}{R\pi^2\varepsilon_0} * \frac{dG\left[\left(\frac{r}{R}\right)^2\right]}{dr}; & 0 < r \le R \\ \frac{Q_t}{R\pi^2\varepsilon_0} * \frac{d\left\{\left(\frac{r}{R}\right) * G\left[\left(\frac{R}{r}\right)^2\right] + \frac{1-\left(\frac{r}{R}\right)^2}{\left(\frac{r}{R}\right)} * K\left[\left(\frac{R}{r}\right)^2\right]\right\}}{dr}; & R < r < \infty \end{cases} \quad (3\text{-}10)$$

Here:

$$G(m) = \int_0^{\frac{\pi}{2}} d\theta \sqrt{1 - m * \sin^2\theta} \quad (3\text{-}11)$$

Further:

$$K(m) = \int_0^{\frac{\pi}{2}} \frac{d\theta}{\sqrt{1 - m * \sin^2\theta}} \quad (3\text{-}12)$$

In this equation, Q_t indicates the total trapped charges, m indicates a variance corresponding to G(m).

By assuming that the electric field required for domain switching is E_{r,θ_2} = 40 kV/cm, the radius of the e-beam illuminated area is R = 100 nm and the electric field of 40 kV/cm is achieved at r = 50 nm; the required charge density (absolute value) $|J|$ calculated from equations (3-10, 3-11 and 3-12) is approximately 1.4×10^{-3} q_e/nm^2 (1 q_e = 1 electron charge).

The effective electric field E_{z_2} at (r,θ) is the z-axis component of E_{z_2}; therefore:

$$E_{z_2} = E_{r,\theta_2} \cos\theta \quad (3\text{-}13)$$

Based on equations (3-10 to 3-13), the areas with $E_{z_2} \geq E_c$ are sketched in Figure 3-6 with red and green lines indicating the boundaries of the areas. The value of the electric field in the areas marked with yellow shadows tracing the illumination boundary is infinitely large and contradicts the experimental results shown in Figures 3-1 and 3-2. Therefore, the distribution of trapped charges does not suddenly drop to zero at r = R and the trapped charges distribution should be non-uniform.

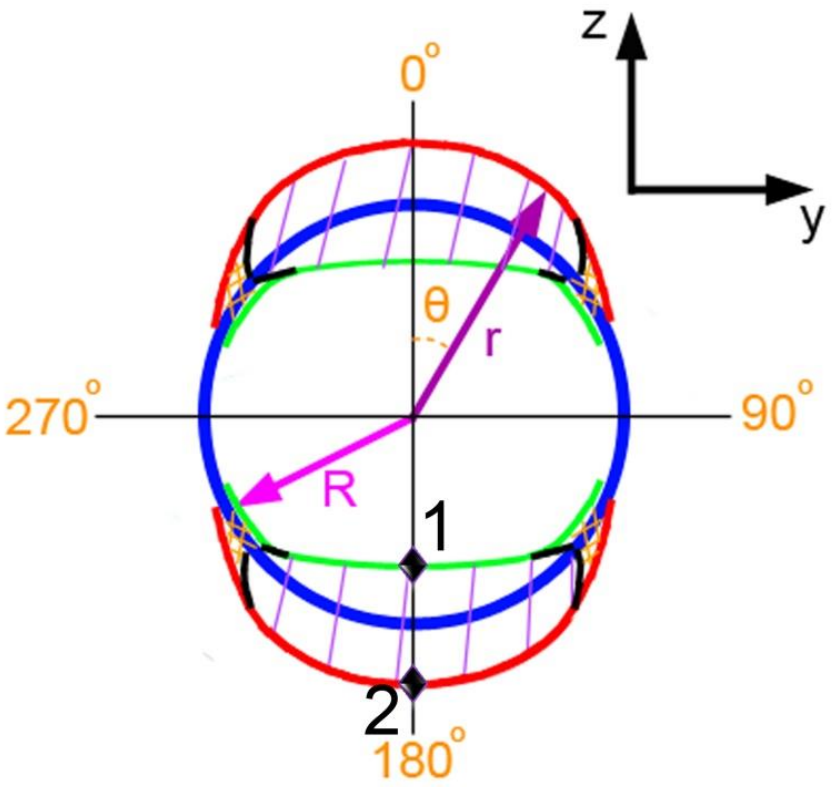

Figure 3-6 A theoretic model for the electric-field-magnitude distribution generated by uniformly distributed trapped charges. The blue circle indicates the e-beam illumination area. The red and green curves present the boundaries with E_z equal to E_c; areas with yellow shadow show E_z as equal to or larger than E_c.

3.3.3. Experimental results

Theoretical calculations concerning the magnitude of the time-independent electric field under the influence of continuously passing electrons show that E_{z_1} = 2.43*10^{-7} kV/cm for r = 100 nm, which is eight orders smaller than the coercive field of 40 kV/cm for $YMnO_3$ [161] and is therefore negligible. The electric field to which the trapped charges contributed is therefore the major element for domain reorientation.

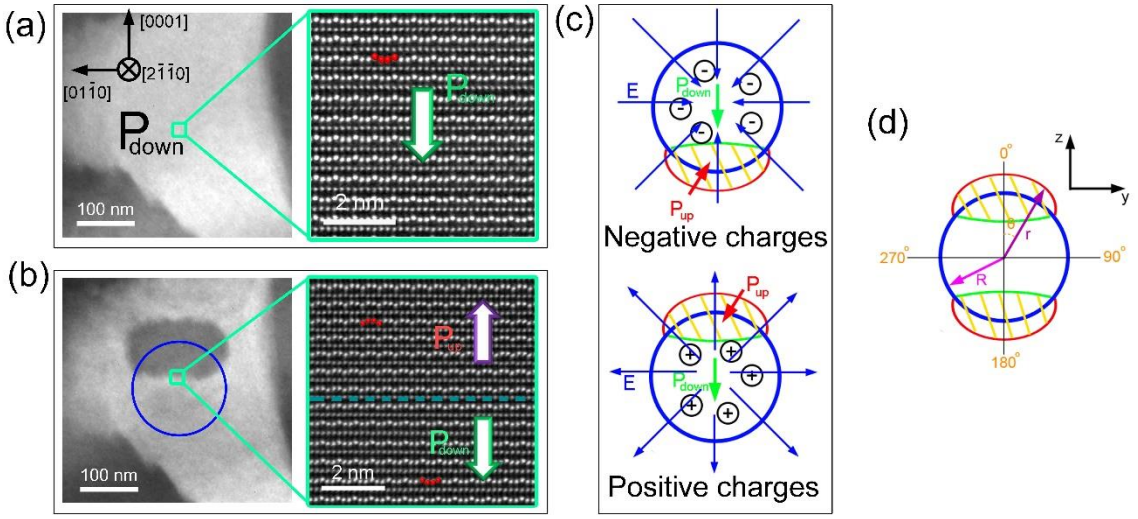

Figure 3-7 (a–b) TEM (left) and HAADF-STEM (right) images showing polarisation before and after e-beam irradiation. **(c)** Schematic drawings of electric fields generated by negative and positive charges. The areas where domain switching would occur are indicated with yellow shadow bounded by red and green boundary lines.

When an e-beam interacts with thin-film oxide specimens, there may be a few interaction effects, including electron accumulation in the illuminated area[268, 272, 273], secondary electron emissions[274] and the introduction of oxygen vacancies[275]. While electron accumulation leads to negative charges in the e-beam-illuminated area, the latter two cases introduce positive charges. Therefore, it is important to identify the sign of the total trapped charges in the e-beam-illuminated area. Figure 3-7 (a) shows a TEM image of a domain of bright contrast taken from a <2$\bar{1}\bar{1}$0> zone-axis. A high-angle annular dark-field scanning (HAADF) STEM image taken from the green-square area indicates that the polarisation in the domain is down-poled (P_{down}). Four red dots are marked in Figure 3-7 (a), which indicates the positions of yttrium ions that are used to identify the polarisation direction[167, 265]. Figure 3-7 (b) shows the results of e-beam irradiation in the blue-circled area. Domain switching occurred in the upper part of the irradiation area. The HAADF-STEM image in Figure 3-7 (b), taken at the domain boundary, confirms that the polarisation in the dark-contrast area is up-poled (P_{up}) while the polarisation in the bright-contrast area remains the same.

The effects of electric fields generated by negative and positive charges on domain switching are illustrated in Figure 3-7 (c). Negative charges result in the electric field directions pointing towards the centre of the irradiation area. In this case, the polarisation in the lower part of the irradiation area will be reversed. Positive charges will lead the electric field directions to point outwards, causing domain switching in the upper part of the irradiation area. The experimental results adhere to the latter case, indicating that the total trapped charges are positive and that they are attributed to the knockout of elastic and inelastic auger and photoelectrons (secondary electrons) as well as to oxygen anions by the e-beam[276].

Because assuming uniform charge distribution in the e-beam-illuminated area leads to infinite electric fields at the edge of the e-beam illuminated area, as a result of the sudden drop of the electrostatic potential at the edge, charges should be distributed in a non-uniform way (but still with axial symmetry) in the e-beam-illuminated area. Nevertheless, an assumption of the uniform distribution of charges within the e-beam-illuminated area can be used to estimate the amount of charges required for domain switching. The calculated value of the charge density needed for domain switching is ~ 1.4×10^{-3} q_e/nm^2. Gatel et al. reported that the e-beam illumination of insulated oxide MgO nanocubes leads to a positive charge density of 8.6×10^{-3} q_e/nm^2 [274], which is five times higher than the value of 1.4×10^{-3} $q_e/nm.^2$ The total positive charge density of $YMnO_3$ would be similar to that of MgO, because it also led to domain switching. The experimental results that provided exact information about the switched domain area can be used for data fitting to ascertain the value of E_{z_2} in equation (3-1) as a function of position and e-beam-illumination time.

Based on the experimental results, the two areas in which $E_{z_2} \geq E_c$—where E_c is the value of the coercive field—in a ferroelectric material are schematically drawn and covered with yellow shadow in Figure 3-7 (d). E_{z_2}, in the top and bottom yellow-shadowed areas, points in

opposite directions and, therefore, has opposite effects when redirecting the polarisation. These are the two areas where the local polarisation can be redirected when its direction runs antiparallel to E_{z_2}, which explains the phenomena shown in Figures 3-1 and 3-2.

3.3.4. Electric fields induced by trapped charges

The experiment results showed that the magnitude of the electric field generated by trapped charges depends on the relative location of the measured spot (r, θ), the total charge of electrons Q_t as a function of the illumination time t, and the illumination volume V which includes the radius of the illuminated area R and the specimen thickness h. Without knowing the real distribution of the trapped charges, it is impossible to theoretically model the exact shape and size of the areas for $E_{z_2} \geq E_c$. Because a domain switch occurs when $E_{z_2} \geq E_c$ and when it runs opposite to the polarisation direction, the shape and size of an area in which $E_{z_2} \geq E_c$ can be experimentally determined. It is expected that $E_{z_2} = E_c$ at the boundary of the switched area. Figure 3-8 demonstrates how E_{z_2} is calculated within a switched domain area. As shown in Figure 3-8 (a), a point (r_i, θ_i) is located at the edge of a switched area (a red-dashed curve), where E_{z_2} = E_c at time t = t_1. Since the following relationship $E_{z_2} = E(r_i, \theta_i)_2 * \cos\theta$ is satisfied, the $E(r_i, \theta_i)_2$ can be calculated. Because $E(r_i, \theta_i)_2$ is of axial symmetry—that is, $E(r_i, \theta_i)_2$ is only a function of r—$E(r_i, \theta_i)_2 = E(r_i)_2$, where θ varies from 0° to 360°. Because $E_{z_2} = E(r_i)_2 * \cos\theta$ = Ec at the boundary of the switched domain area, the value of $E(r_i)_2$ at points 1, 2 and 3 in Figure 3-8 can be calculated based on the experimental data. A series of $E(r_i)_2$ is therefore achieved. In terms of fitting the experimental $E(r_i)_2$ using Matlab coding (see Figure 3-8 (b)), $E(r_i)_2$ is proportional to the shape function $S\left(\frac{r}{R}\right)$ and $F\left(\frac{r}{R}\right)$ at t = t_1 as follows:

$$E(r_i)_2 \propto \begin{cases} S\left(\frac{r}{R}\right) = 93.5\left(\frac{r}{R}\right) - 34.9\left(\frac{r}{R}\right)^2 & 0 < r \leq R \\ F\left(\frac{r}{R}\right) = -23 + 155.7\left(\frac{r}{R}\right) - 75.5\left(\frac{r}{R}\right)^2 & R < r < \infty \end{cases} \quad (3\text{-}14)$$

Therefore, the shape of E_{z_2} > E_c can be calculated at t = t_1 using the following equation:

$$E_{z_2} \propto \begin{cases} S\left(\frac{r}{R}\right) = \left[93.5\left(\frac{r}{R}\right) - 34.9\left(\frac{r}{R}\right)^2\right] * \cos\theta & 0 < r \leq R \\ F\left(\frac{r}{R}\right) = \left[-23 + 155.7\left(\frac{r}{R}\right) - 75.5\left(\frac{r}{R}\right)^2\right] * \cos\theta & R < r < \infty \end{cases} \quad (3\text{-}15)$$

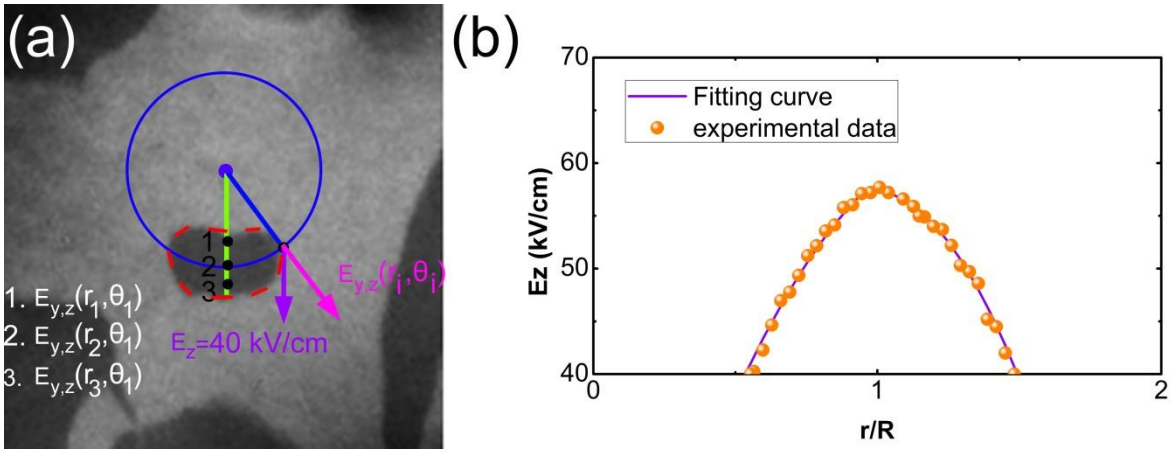

Figure 3-8 (a) A schematic demonstration of how $\boldsymbol{E_{z_2}}$ is calculated within a switched domain area. **(b)** Fitting experimental data.

3.3.5. The effect of e-beam exposure time on the generated electric field

As the value of the charges, which determines the size of the areas where $E_{z_2} \geq E_c$, is a function of time, the size of a manipulated domain area can be controlled by the e-beam-illumination duration. A series of focused e-beam-illumination experiments with the illumination durations set at 10, 30, 50, 100, 200 and 600 seconds was carried out (see Figures 3-9(a)–(g)). Figure 3-9 (a) shows the initial morphology of a domain (α+) structure before focused e-beam illumination. After focused e-beam illumination for 10 seconds, the

morphology remained unchanged (see Figure 3-9 (b)), which indicates that the maximum value of E_{z_2} at 10 seconds is smaller than the coercive field of 40 kV/cm. At 30 seconds (see Figure 3-9 (c)), a nanoscale α- domain nucleated at the upper part of the e-beam-illuminated area, as indicated by the hat-like red-dashed lines, indicating that the E_{z_2} in the α− area is larger than the coercive field of 40 kV/cm. Further increasing the e-beam illumination time led to a further expansion of the α- domain, but the expansion rate diminished gradually, as confirmed by the TEM images at 50, 100, 200 and 600 seconds in Figures 3-9 (d) to 3-9 (g). Figure 3-9 (h) illustrates the experimental E_{z_2}–r curves (dots) for e-beam illumination durations of 30, 50, 100, 200 and 600 seconds. After achieving the E_{z_2}–r curves at different e-beam-illumination durations, the contribution of trapped charges to E_{z_2} as a function of time for any position was achieved, as shown in the inset image for Figure 3-9 (h). After fitting the experimental data as shown in Figure 3-9 (h) using Matlab coding, the electric field E_{z_2} had the following relationship with the illumination time t:

$$E_{z_2} \propto T(t) = \frac{5t}{(5t+100)} \tag{3-16}$$

Here, t is the illumination time and $T(t)$ is the electron accumulation-efficiency function in terms of time t, which is fitted as $T(t) = \frac{5t}{(5t+100)}$ and shown in Figure 3-9.

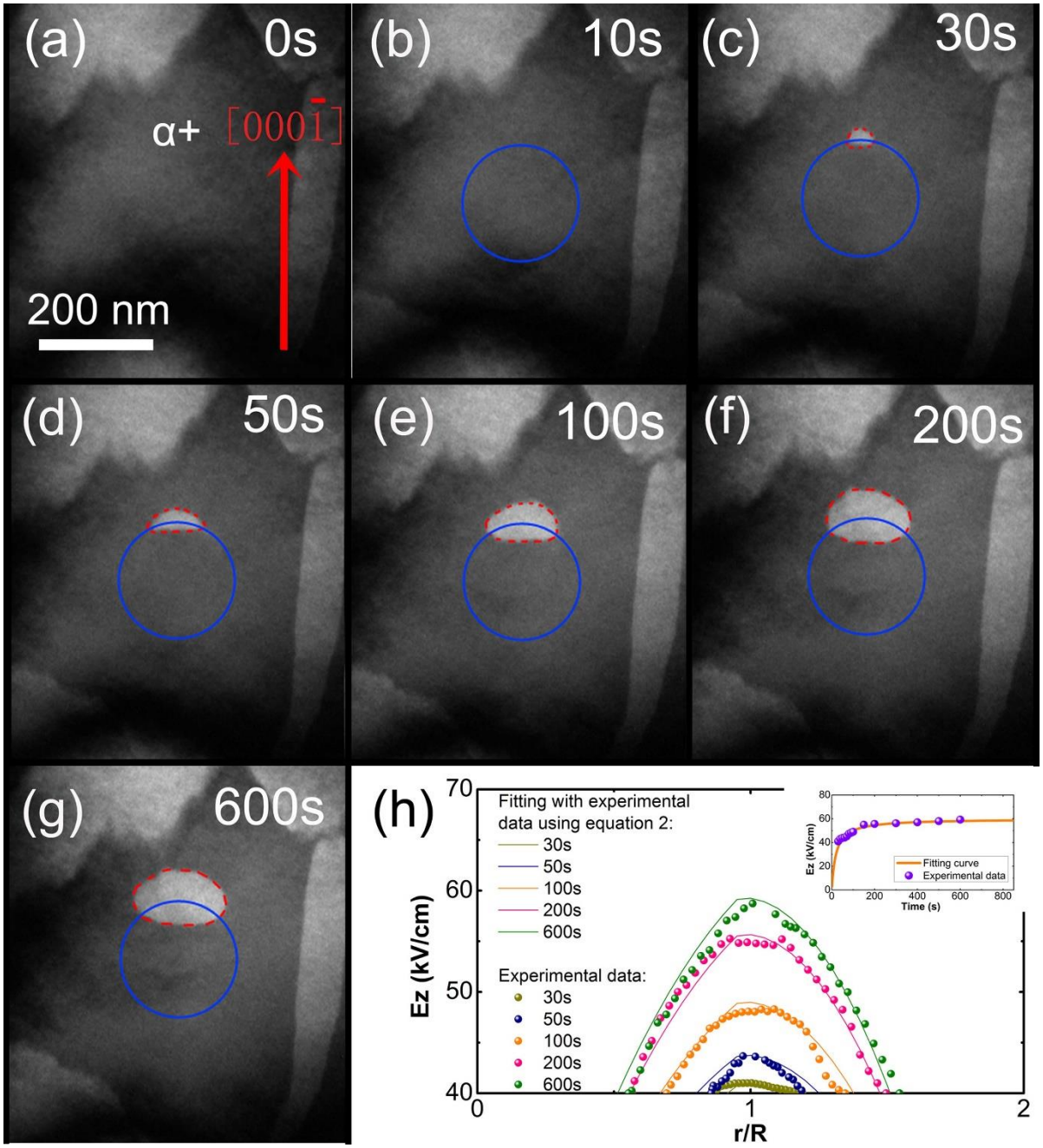

Figure 3-9 (a–g) A series of dark-field images showing the domain evolution under e-beam illumination at t = 0 s, 10 s, 30 s, 50 s, 100 s, 200 s and 600 s respectively. Blue circles represent the illumination area. Red-dashed curve include the experimental converted α-domain area. **(h)** Experimental E_z as opposed to r plots at different illumination times and the corresponding fitting curves using equation (2). The inset shows the fitting curve to the experimental E_z as a function of time.

In equations (3-15) and (3-16), the electric field generated by the accumulation of trapped charges in Figure 3-9 is therefore derived as:

$$E_{z_2} = \begin{cases} \left(\frac{5t}{(5t+100)}\right) * \left(93.5 * \left(\frac{r}{R}\right) - 34.9 * \left(\frac{r}{R}\right)^2\right) * \cos\theta\,; & 0 < r \leq R \\ \left(\frac{5t}{(5t+100)}\right) * \left(-23 + 155.7 * \left(\frac{r}{R}\right) - 75.5 * \left(\frac{r}{R}\right)^2\right) * \cos\theta\,; R < r < \infty \end{cases} \quad (3\text{-}17)$$

As the illumination volume and the electron accumulation ability for different materials also affect the electric field, the general equations are derived as follows:

$$E_{z_2} = \begin{cases} \eta * V(h,R) * \left(\frac{5t}{(5t+100)}\right) * \left(93.5 * \left(\frac{r}{R}\right) - 34.9 * \left(\frac{r}{R}\right)^2\right) * \cos\theta\,; & 0 < r \leq R \\ \eta * V(h,R) * \left(\frac{5t}{(5t+100)}\right) * \left(-23 + 155.7 * \left(\frac{r}{R}\right) - 75.5 * \left(\frac{r}{R}\right)^2\right) * \cos\theta\,; R < r < \infty \end{cases} \quad (3\text{-}18)$$

Here, η is a constant and V(h, R) is the volume function for the electric field generated by trapped charges. It is difficult to experimentally fit this function. Equation (3-17) is a special instance of equation (3-18) where the volume function and η are equal to one.

Using this equation, the calculated maximum electric field generated at 10 seconds in Figure 3-9 (b) was 20 kV/cm, which is smaller than the coercive field. Therefore no domain reorientation occurred at t = 10 s.

It was found that the shapes in Figure 3-9 adhered to the calculated E_{z_2}–r curves (solid lines) using equation (3-17) when the illumination volume was kept constant, although there were small deviations in different experiments.

3.3.6. Electron-beam manipulation of domain patterns

By taking advantage of this controllable, erasable and highly precise positioning technique, domain patterning with high spatial resolution is achievable. Figure 3-10 (a) demonstrates dark-field TEM images of four randomly selected, original domain areas. Using an e-beam with a radius of 100 nm, the letters U, S, Y and D—an abbreviation for the University of Sydney—were written in each of the four areas (see Figure 3-10 (b)). It can be

observed that some thin white and black straight lines pass through the patterns. These lines are antiphase domain walls. To avoid antiphase domain boundaries affecting the pattern quality, poled $YMnO_3$ samples or other ferroelectric materials with large single domain areas may be used.

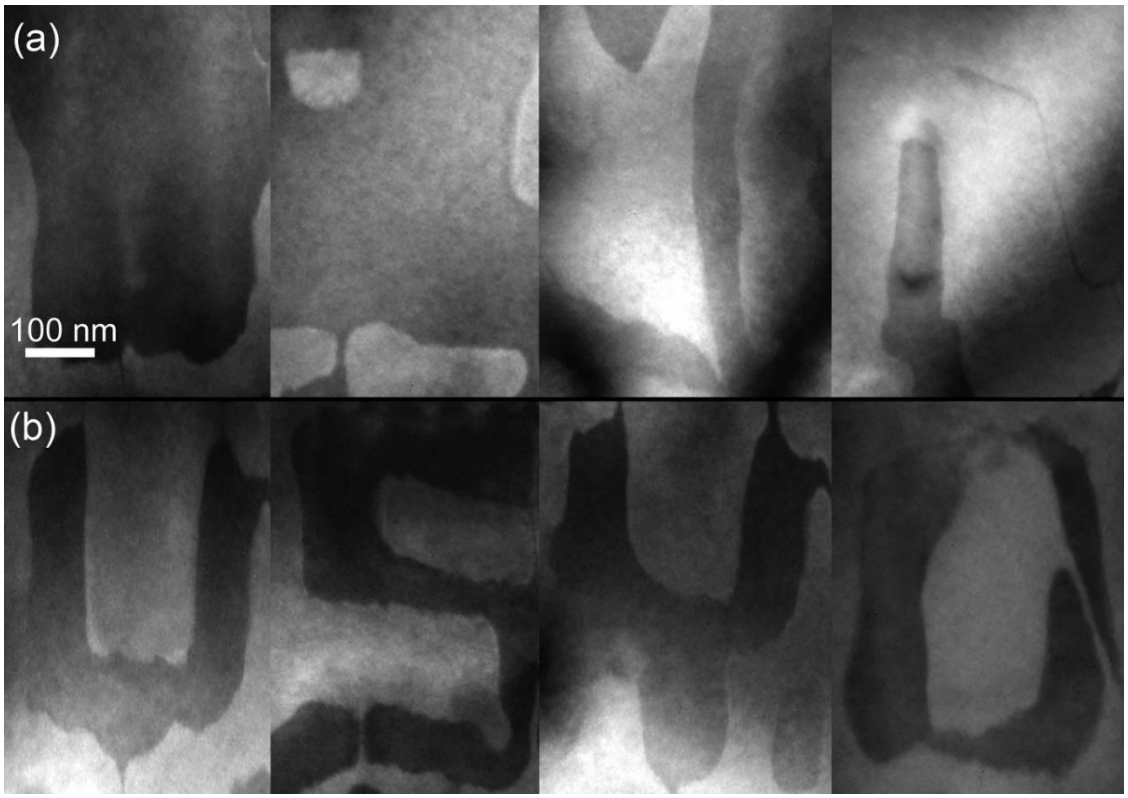

Figure 3-10 (a) Initial domain configurations in four areas before e-beam illumination. **(b)** Letters U, S, Y and D were written on the areas in (a) via e-beam illumination.

3.3.7. The effect of long-time electron-beam illumination on the crystalline microstructure

The e-beam illumination with a radius of 50 nm is gentle and, therefore, does not lead to any detectable specimen damage. Figure 3-11 shows two typical high-resolution TEM images taken from a single area before (see Figure. 3-11 (a)) and after (see Figure 3-11 (b)) exposure to the e-beam with a radius of 50 nm for 600 seconds. The structure remained the same as that

before the prolonged e-beam illumination. The inset in Figure 3-11 presents enlarged Fourier-filtered images clearly showing a perfect crystalline structure before and after e-beam illumination. In fact, the e-beam intensity for domain reversal is lower than that of high-resolution imaging (but the high-resolution imaging takes a much shorter time), as evidenced by the e-beam diameters used for domain reversal (50 nm) and for high-resolution imaging (~ 20 nm, which is more focused). However, long-term exposure to an e-beam could introduce point defects—for example, oxygen vacancies—which are not detectable by conventional high-resolution TEM. These point defects would contribute to the net local charges.

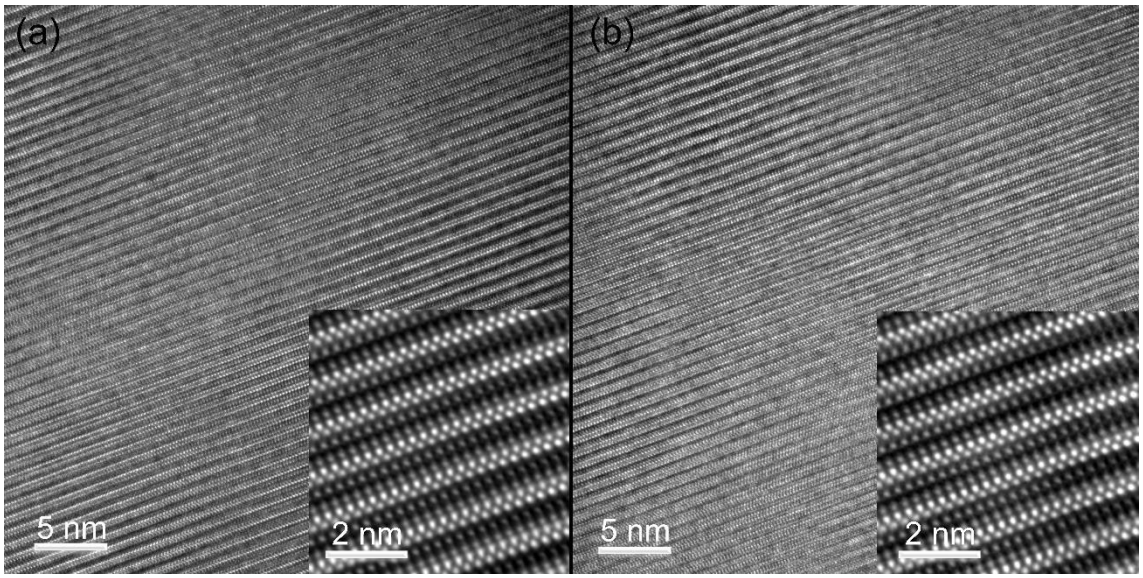

Figure 3-11 Typical high-resolution TEM images with inset enlarged Fourier-filtered images of an area before **(a)** and after e-beam irradiation for 600 s **(b)**.

3.4. Summary

In conclusion, I demonstrate erasable stable ferroelectric nanodomain manipulation in thin-film ferroelectric materials using an e-beam. The experiment results and theoretical analysis indicate that the accumulation of positive charges in the thin film plays the key role in generating an electric field for ferroelectric nanodomain manipulation switching. This method

requires no pre-poling, no electrode and no physical contact with a tip or any other manipulator and, therefore, would be ideal for manufacturing miniature and integrated electronic devices. My results also indicate that caution is needed in the electron microscopy investigation of ferroelectric domain structures to avoid any artificial effects caused by e-beam illumination[265].

Chapter 4

Domain switching kinetics by mechanical and electrical stimulation in relaxor-based ferroelectrics for non-volatile memories

4.1. Introduction

In non-volatile ferroelectric devices, two opposite polarisation directions act as logical signals, serving as memory bits which can be written and read by applying electric fields[76, 165]. However, the instability of written ferroelectric domains—for example, time-dependent ferroelectric backswitching—has been a long-standing problem that causes significant data loss[193, 199, 277-279]. Such backswitching results from the surface electrostatic or internal built-in elastic energy[199, 280, 281] and has higher impact on domains of small sizes. Small domain sizes are critical for high-density storage[257]. The relaxation of high-energy domain walls significantly drives ferroelectric backswitching when the switched domain sizes are small[199]. Recently, ferroelastic domain switching by electrical stimulus has also been considered for memory applications[176, 197]. However, the high levels of elastic strain energy accompanying ferroelastic domain switching tend to relax the switched domains, causing ferroelastic backswitching of zero bias[176, 282]. Both ferroelectric and ferroelastic backswitching suggest a lack of reliability in domain switching under electrical stimulus. Mechanical excitation is another possible way for controlling ferroelectric/ferroelastic domain switching[80, 283]. Mechanical writing of ferroelectric polarisation in a $BaTiO_3$ film has been achieved[80] where

polarisation is 180° reversed by mechanical loading as a result of a large strain gradient applied to the film surface by a probe via the mechanism of flexoelectricity[191, 284]. Although stable domain patterns undertaken for days without relaxation are generated by mechanical writing, written domains are not reversible because of the unidirectional nature of the mechanical loading. Therefore, a new approach is required to overcome the abovementioned limitations, using either electrical or mechanical excitation for memory applications of ferroelectric materials.

Relaxor-based ferroelectric single crystals[285, 286] have recently attracted significant attention because of their unique hysteresis behaviour, their ultrahigh piezo-electric properties, their electromechanical coupling factors[6] and their chemical composition, which is in the vicinity of the MPB. Compared with normal ferroelectrics, relaxor-based ferroelectrics in MPB have abnormally small levels of domain-wall energy, small coercive fields[287] and miniature domain sizes, which allow for the easy redistribution of invariant domain populations[145] that exhibit different domain switching kinetics under external stimuli. This raises the possibility of utilising different domain switching kinetics to overcome the abovementioned difficulties. However, the majority of work on such relaxor-based ferroelectric materials has focused on macroscopic material responses under electric loading or mechanical loading[6, 209, 288]; little has been discovered about microscopic responses.

For this research, we used an in-situ TEM[145, 150, 167] and phase-field modelling[250] to explore the ferroelastic domain switching kinetics under applied electrical and/or mechanical stimuli in relaxor PMN-33%PT single crystals. It was found that ferroelastic domain structures in PMN-33%PT single crystals are fully recoverable under a mechanical loading–unloading cycle (a mechanically reversible state) before electrical biasing. After applying a bias, domains become sensitive to mechanical load and exhibit only partial recovery (a mechanically irreversible state). However, the mechanically irreversible state returns to the mechanically

reversible state after another mechanical loading–unloading cycle. Our results provide a new approach for recovering ferroelastic domain structures via the successive cycling of mechanical and electrical stimuli. Based on these discoveries, instead of trying to overcome the intrinsic instability of written ferroelectric domains, we propose a conceptual strategy to take advantage of the mechanically irreversible state and the mechanically reversible state for reliable bit writing and reading in non-volatile memory devices. This expands the number of potential candidate materials for non-volatile memory devices.

Figure 4-1 (a) presents a schematic of the in-situ experimental setup. A bulk PMN-33%PT was fixed on a Cu plate using Pt deposition. Multiple PMN-33%PT pillars with dimensions of 2.0 μm × 1.6 μm × 0.06 μm (length × width × thickness) were produced using mechanical grinding and FIB processing. During the sample preparation using FIB, a thin damaged amorphous layer was introduced on the surface of the pillar. A small current was used to control the thickness of the damage layer to around 3-5 nm which does not affect the domain switching kinetic in our experiments. Experiments on bulk TEM samples prepared by a normal TEM sample preparation method suggested that FIB affects little for the proposed domain switching kinetic. In-situ mechanical and electrical stimulations under a TEM were applied by a conductive tip. The Cu plate acted as one electrode and the conductive tip acted as the other electrode. A typical domain configuration observed from a pillar is presented in Figure 4-1 (b). Two types of domains appear with different contrasts.

PMN-xPT with the composition x = 33% is found at MPB with a monoclinic structure[132, 289]. The ferroelectric adaptive phase theory[126, 129, 290] suggests that monoclinic phases, consisting of the miniaturisation of stress-accommodating tetragonal domains, are micro-domain-averaged tetragonal phases. A moderate constraint on the pillar exerted by the PMN-PT-base single crystal is thus prone to head-to-tail, 90° ferroelastic domain configuration. This is confirmed by the STEM-HAADF images shown in Figure 4-1(b). Through the measurement

of the displacement between the Pb cations and their surrounding Mg/Nb/Ti cations in the HAADF images[184, 231], domains with light contrast (e.g., the c-domain) have their polarisation directed upward (see the bottom-left HAADF image) and domains with dark contrast (e.g., the a-domain) have their polarisation pointing to the right (see the top-right HAADF image), indicating that neighbouring domains have a head-to-tail, 90° domain relationship. All STEM images were Fourier filtered using a lattice mask to reduce noise. Atomic positions were determined by fitting the STEM images as two dimensional Gaussian peaks using a Ranger 2.4 script in Matlab. Atomic displacement was calculated using Matlab and presented as the difference vector between the centre of a B-site cation and the centres of its four nearest neighbouring A-site cations.The 90° domain boundaries in Figure 4-1 (b) are indicated using blue-dashed lines. Two parallel green lines were drawn in Figure 4-1 (b) to indicate the area of focus for the following investigation of external-stimulation-induced domain switching phenomena.

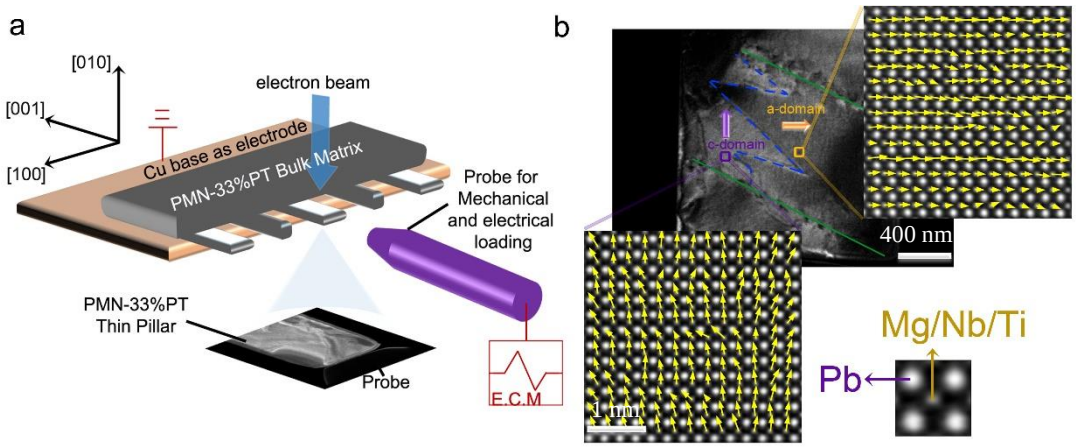

Figure 4-1 (a) Schematic diagram of experimental setup. A bulk PMN-33%PT matrix with thin pillars was fixed on a grounded Cu platform using Pt deposition. A conductive tip connected to the ECM acts as an indenter and electrode for mechanical and electrical loading. The actual allocation of the pillar and the tip was captured by the enlarged TEM image. **(b)** Dark-field TEM image and STEM-HAADF images showing a head-to-tail, tetragonal a/c-domain configuration. Domain walls are indicated using blue-dashed lines. Two parallel green lines indicate the area investigated in this study.

4.2. In-situ experiment and phase-field modelling

4.2.1. An initial mechanical loading cycle

Stress was applied to the pillars by moving the flat conductive tip towards the pillars in the displacement-control mode with a displacement rate of 3 nm/s when approaching and −4 nm/s when retracting, causing the asymmetry of the curve. The evolution of domain configuration during a mechanical loading–unloading cycle and the related load/bias–time curves (bias = 0) are shown in Figures 4-2 (a) and 4-2 (b) respectively. Points 1 (before loading), 2, 3 and 4 in Figure 4-2(b) correspond to the first, second, third and fourth domain configurations in Figure 4-2(a).

Under increasing loads, the c-domain shrank and the a-domain expanded through the motion of the 90° domain boundaries towards the c-domain. The initiation of domain switching starts from the domain boundaries. When the applied load reached 22 μN, the whole area was mostly occupied by the a-domain. Upon unloading, the domain configuration evolved in the opposite direction and the original domain configuration was fully recovered. Because the loading and unloading processes were displacements controlled with constant displacement rates, the approximate linear load–time curve for approaching and retraction and the intersecting fully reversible load-displacement curve in Figure 4-2(b) indicate that the deformation process of the pillar was elastic without significant bending. The maximum load was always kept to ~ 28 μN to ensure the comparability of different loading/unloading experiments. The maximum load corresponded to an applied stress of ~ 300 MPa, which is very small and, therefore, did not damage the material[190, 291].

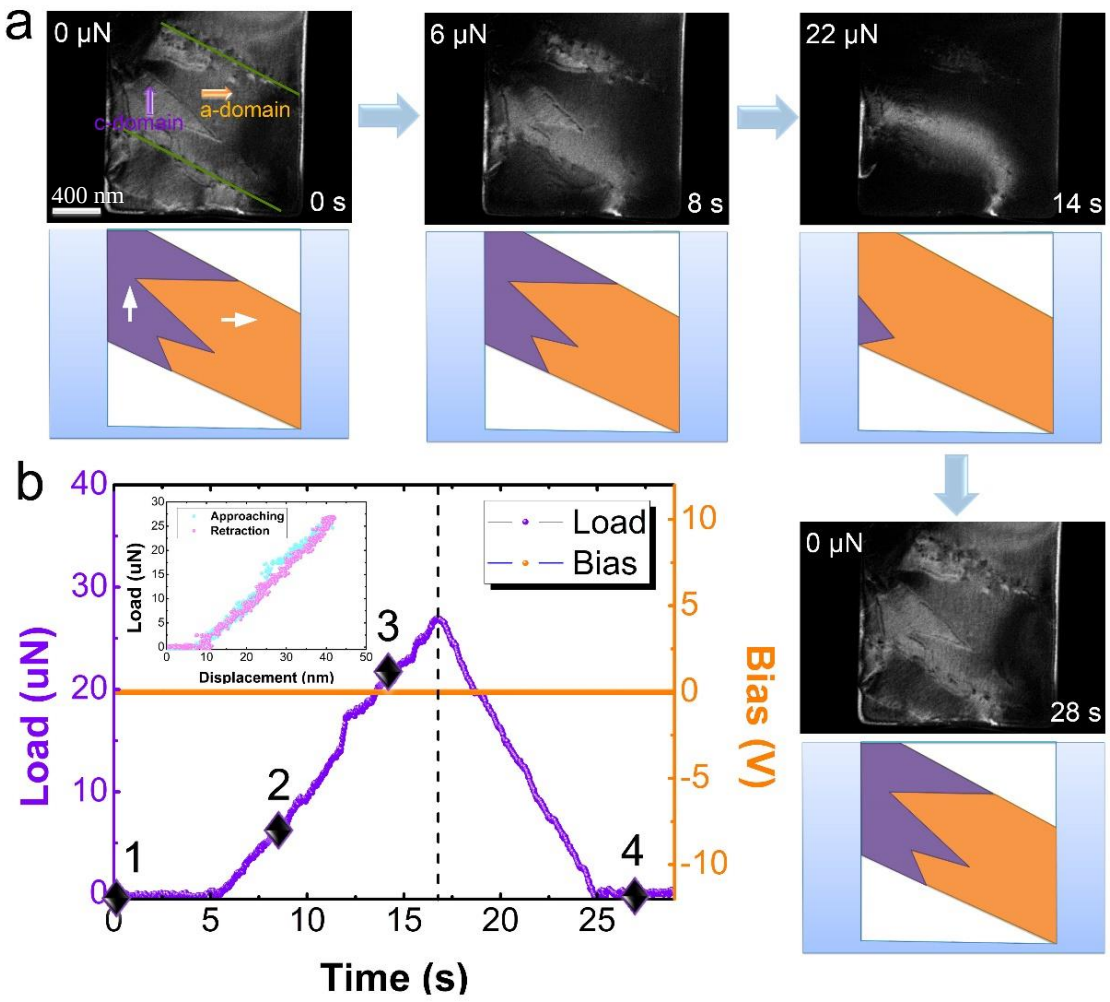

Figure 4-2 (a) A series of images showing the evolution of ferroelastic domains under mechanical excitation. Domains were fully reversed after a mechanical loading–unloading cycle. **(b)** A load/bias versus time curve showing the real-time application of a mechanical load with zero bias. Numbers 1–4 correspond to the image order of a–d and indicate their relative positions on the curve. A load as opposed to a displacement curve is shown in the insect graph.

4.2.2. An electrical loading cycle following a mechanical loading cycle

The effect of a voltage bias on domain configuration is presented in Figure 4-3 (a). The corresponding load/bias–time curve (external load = 0) is illustrated in Figure 4-3 (b). Again, points 1, 2, 3 and 4 in Figure 4-3 (b) correspond to the first, second, third and fourth images in Figure 4-3 (a). Gentle contact between the conductive tip and the pillar was maintained for the closed-loop electrical loading experiment. The bias was raised from 0 V to +10 V for between

five and 15 seconds with a ramping rate of one volt per second, as shown in Figure 4-3 (b). Although no mechanical load was applied, a small load was still detected, which was caused by the electrostrictive effect on the ferroelectric materials. With the increase of the bias from 0 V to +2 V, the domain configuration did not change as the initiation energy for domain motion was not reached. Further increasing the bias resulted in the shrinkage of the a-domain and the simultaneous expansion of the c-domain. When the bias was increased to +10 V, almost the whole area was occupied by a single c-domain, as can be seen in the third image in Figure 4-3 (a); after the retraction of the bias at 15 seconds, the a-domain backswitched and was gradually stabilised at 20 seconds, as shown in Figure 4-3 (a). A comparison of the initial and final domain configurations shows that the area of the c-domain increased after an electrical loading cycle—that is, the domain configuration was only partially recovered. The obtained domain was stable for weeks and kept the same morphology as that shown in the last image in Figure 4-3 (a).

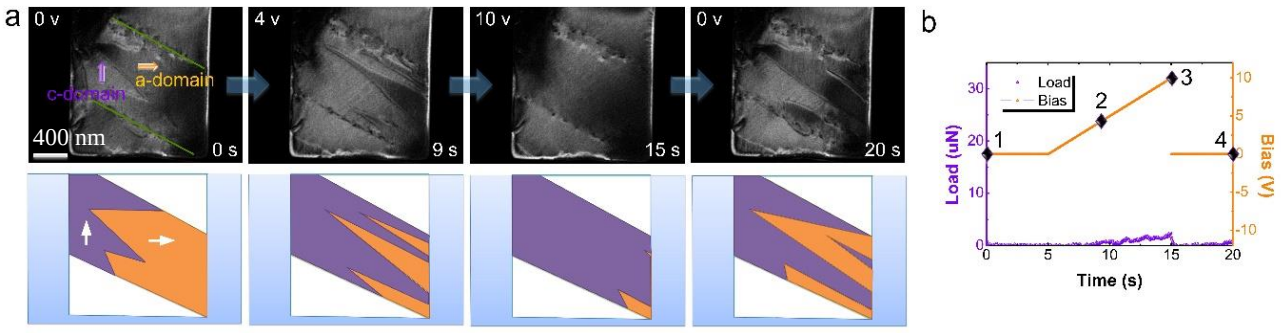

Figure 4-3 (a) A series of images showing the evolution of ferroelastic domains under electrical loading. **(b)** A load/bias–time curve. No mechanical load was applied during the whole process. The bias was applied from 0 V (5 s) to +10 V (15 s) with a ramping rate of 1 V/s.

4.2.3. The phase-field method*

The ferroelastic domain switching process under electrical and mechanical stimuli is simulated via a phase-field model[250] in which the time evolution of polarisation $P_i(i=1,2,3)$ is governed by the Ginzburg-Landau equation:

$$\frac{\partial P_i}{\partial t} = -L\frac{\delta F}{\delta P_i}. \tag{4-1}$$

Here, L is the kinetic coefficient and the total free energy of the system is $F = \int_V \left[f_{bulk}(P_i) + f_{grad}(P_{i,j}) + f_{elas}(P_i, \varepsilon_{ij}) + f_{elec}(P_i, E_i) \right] dV$. The stress-free energy density of PMN-33%PT is described using a sixth-order Landau polynomial:

$$\begin{aligned} f_{bulk} = {} & \alpha_1\left(P_1^2 + P_2^2 + P_3^2\right) + \alpha_{11}\left(P_1^4 + P_2^4 + P_3^4\right) + \alpha_{12}\left(P_1^2P_2^2 + P_1^2P_3^2 + P_2^2P_3^2\right) + \\ & \alpha_{111}\left(P_1^6 + P_2^6 + P_3^6\right) + \alpha_{112}\left[P_1^2\left(P_2^4 + P_3^4\right) + P_2^2\left(P_1^4 + P_3^4\right) + P_3^2\left(P_1^4 + P_2^4\right)\right] + \alpha_{123}P_1^2P_2^2P_3^2 \end{aligned}, \tag{4-2}$$

Here, all the coefficients— $\alpha_1 = -3.39\times10^7\ \mathrm{C^{-2}m^2N}$, $\alpha_{11} = -5.65\times10^8\ \mathrm{C^{-4}m^6N}$, $\alpha_{12} = -1.19\times10^9\ \mathrm{C^{-4}m^6N}$, $\alpha_{111} = 6.05\times10^9\ \mathrm{C^{-6}m^{10}N}$, $\alpha_{112} = 1.94\times10^{10}\ \mathrm{C^{-6}m^{10}N}$, $\alpha_{123} = 3.75\times10^{10}\ \mathrm{C^{-6}m^{10}N}$—are obtained from our thermodynamic study. Isotropic domain-wall energy density is expressed as[184, 292]:

$$f_{grad} = \frac{G_{1111}}{2}\left(P_{1,1}^2 + P_{2,2}^2 + P_{3,3}^2 + P_{1,2}^2 + P_{1,3}^2 + P_{2,1}^2 + P_{2,3}^2 + P_{3,1}^2 + P_{3,2}^2\right), \tag{4-3}$$

*The phase-field modelling was conducted by Dr. Liang Hong under the guidance of Prof. Long-Qing Chen from Pennsylvania State University. (With permission from Dr. Liang Hong and Prof. Long-Qing Chen)

In this case, the gradient energy coefficient is chosen to be $G_{1111}/G_{110} = 0.6$ in reduced units, where G_{110} is related to the voxel size Δ of the computational model by $\Delta = \sqrt{G_{110}/|\alpha_1|_{T=27\,^\circ\mathrm{C}}}$. Polarisation rotation induces spontaneous lattice deformation (ε_{ij}^0) which is related to P_i via $\varepsilon_{ij}^0 = Q_{ijkl} P_k P_l$. Further, Q_{ijkl} signify electrostrictive coefficients measured by experiments. Thus, the elastic energy density associated with the total strain (ε_{ij}) of the pillar is[292]:

$$f_{elas} = \frac{1}{2} c_{ijkl} \left(\varepsilon_{ij} - \varepsilon_{ij}^0\right)\left(\varepsilon_{kl} - \varepsilon_{kl}^0\right), \tag{4-4}$$

Here, c_{ijkl} is the elastic stiffness tensor. In the present simulations, clamped boundary conditions are applied to the interface of the pillar and base substrate. The homogeneous strain $\bar{\varepsilon}_{33} = (1/V)\int_V \varepsilon_{33}^0 dV + s_{3333}\sigma_{33}^{appl}$[293], where s_{ijkl} is the elastic compliance tensor. The strain field is solved through the mechanical equilibrium condition $\sigma_{ij,j} = 0$ by using the microelasticity theory[294] of Khachaturyan and Shatalov. The elastic constants and the electrostrictive coefficients can be found in the work of Zhang[144] and Lu[295] respectively. The electric energy density is[296, 297]:

$$f_{elec} = -\frac{1}{2}\varepsilon_0 k_{ij} E_i E_j - E_i P_i, \tag{4-5}$$

In this case, ε_0 is the vacuum permittivity and k_{ij} is the relative background dielectric constant tensor. For the sake of simplicity, we assume $k_{ij} = 0$ if $i \neq j$. The electric field E_i is composed of an external electric field E_i^{ext} and an electrostatic field E_i^{sta} generated by the bound polarisation charges. A periodical boundary condition is applied to solve the electrostatic equilibrium condition $-\varepsilon_0 k_{ij}\varphi_{,ji} + P_{i,i} = 0$, where $E_i^{sta} = -\varphi_{,i}$.

A three-dimensional simulation was first conducted, whereby the ferroelastic phase boundary orientation was normal to 100 and the phase-transition kinetics was the same as that shown in the two-dimensional simulation. Therefore, to save computational time, this study adopts a two-dimensional simulation (using a regular grid of $1\Delta \times 128\Delta \times 128\Delta$ voxels) with periodic boundary conditions along all dimensions. The voxel size is $\Delta = 1\,\mathrm{nm}$. The semi-implicit Fourier-spectral method[298] is used to solve equation (4-1). The system is first endowed with a tetragonal a/c-domain structure with a 90° domain wall. Then, the system is relaxed to equilibrium (after 40,000 time steps) to obtain the initial domain configuration. The fraction of a-domain in the initial ferroelastic domain configuration is minimised according to the constraint[198]. Since we cannot exactly measure the constraint condition of the PMN-33%PT pillar, there is one order of magnitude's difference in the applied external stimuli for the experiment and simulation. Such difference can be affected by various factors; for example, the number of domain variants, nucleation behaviours and defects[299]. However, this does not affect the proposed mechanism discussed in this study.

4.2.4. Phase-field calculations and simulations

The stress applied to initiate domain-wall motion in this sample is around 40 MPa, which is well below the values for other reported materials[190]. This type of domain-wall motion is easily triggered as a result of the unpinning effect on the domain walls, which is commonly observed in relaxors around MPB[300, 301]. Given the unit-cell volume of PMN-33%PT at a room temperature of 64.9 $Å^3$ [287], our phase-field calculation gives the energy of the single tetragonal a- and c-domains in the PMN-33%PT pillar as -0.443 meV and -1.05 meV respectively—two orders of magnitude smaller than the energy (~100 meV) of tetragonal domains in conventional ferroelectric materials[302]. Note that the domain energy calculated is low because the energy of defects is not included and domain nucleation behaviours are simplified. This low energy is a reference value compared with the zero domain energy in the paraelectric state. The exclusion

of other types of energy does not affect the conclusion drawn in this chapter. This reversible domain switching in a mechanical loading–unloading cycle is caused by two factors. First, a small external field can activate the mobile domain wall's motion as a consequence of the small energy barrier among the tetragonal domains[287]; this accords with the easy polarisation rotation around MPB. Second, an elastic constraint to the PMN-33%PT pillar causes remarkably different stress states for in-plane a-domains and out-of-plane c-domains, resulting in an asymmetric energy barrier between the two domains. In particular, domain transition from a-domain to c-domain provides a lower energy barrier, as shown in Figure 4-4 (a).

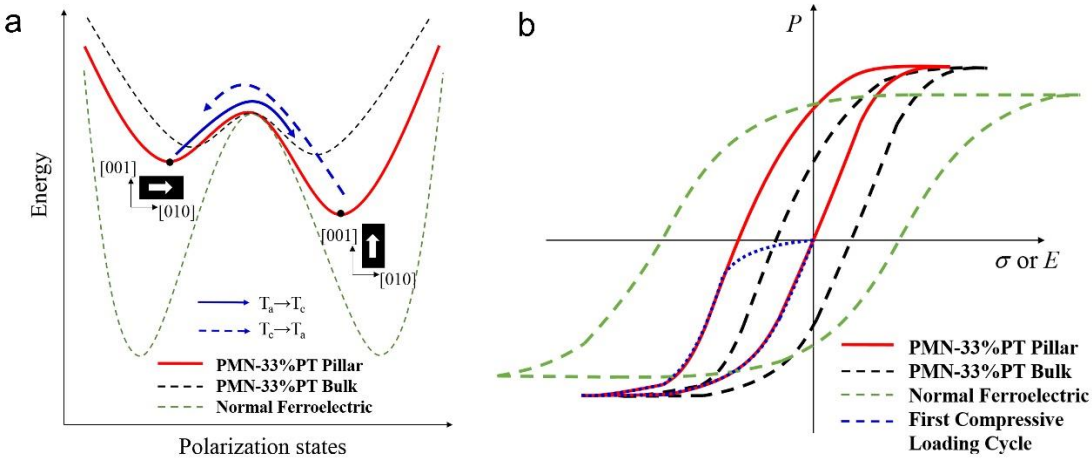

Figure 4-4 (a) Schematic illustration of the asymmetric energy barrier among the tetragonal ferroelastic domains of a PMN-33%PT pillar. Mechanical constraint exerted on the pillar breaks the original symmetric energy barrier of the PMN-33%PT bulk single crystal, resulting in an easier domain transition from a-domain to c-domain compared to the reverse transition path. Such different transition rates will not be obvious in normal ferroelectrics because of the large energy barriers. **(b)** Schematic illustration of a displaced hysteresis loop of a PMN-33%PT pillar in comparison to the hysteresis loops of a bulk relaxor single crystal and normal ferroelectrics.

Compared to the hysteresis loop of conventional ferroelectrics (the green-dashed line), the hysteresis of the bulk PMN-33%PT single crystal is slim with a small coercive field[6]. An asymmetric energy barrier of the PMN-33%PT pillar displaces the slim hysteresis to the left (the red solid line), making the initial ferroelastic domain structure closer to the domain state at the positive coercive field, as shown in Figure 4-4 (b). As a result, the compressive loading–

unloading cycle (the dashed blue line in Figure 4-4 (b)) can recover the initial ferroelastic domain structure.

Such reversible hysteresis loops have been observed in a <001> poled relaxor $Pb(Zn_{1/3}Nb_{2/3})O_3$-$PbTiO_3$ single crystal with easily activated 71° domain rotation[6]. In an aged $BaTiO_3$ single crystal, the defect-induced internal field pins and retracts the ferroelastic domain-wall movement, producing reversible domain switching[303]. However, these two reversible phase transition processes are studied based on observations at a macro-scale, where the effects of the complex domain structure and heterogeneous nucleation are difficult to explicitly investigate. The present study, which utilises asymmetric domain transition kinetics among tetragonal a- and c-domains in the ubiquitous microscopic 90° head-to-tail ferroelastic domain configuration, provides a new approach for reversible domain switching.

In agreement with the experimental results, phase-field modelling also suggests that the stable domain configuration in a tetragonal ferroelectric holds {101} 90° ferroelastic domain walls, which move in the direction of normal to domain-wall planes under the mechanical loading as shown in Figure 4-5 (a). The polarisation rotation only occurs around the domain walls and the polarisation direction within the bulk domains does not change[175]. One interesting feature of this initial ferroelastic domain configuration in the PMN-33%PT pillar is that this domain state is located around the positive coercive field. This is because of the asymmetric and low energy barriers between the tetragonal a- and c-domains (as shown in Figures 4-4 (a) and 4-4 (b)). When a compressive loading–unloading cycle is applied, phase-field modelling suggests a recoverable domain switching, as shown in Figures 4-5 (a) and 4-5 (b).

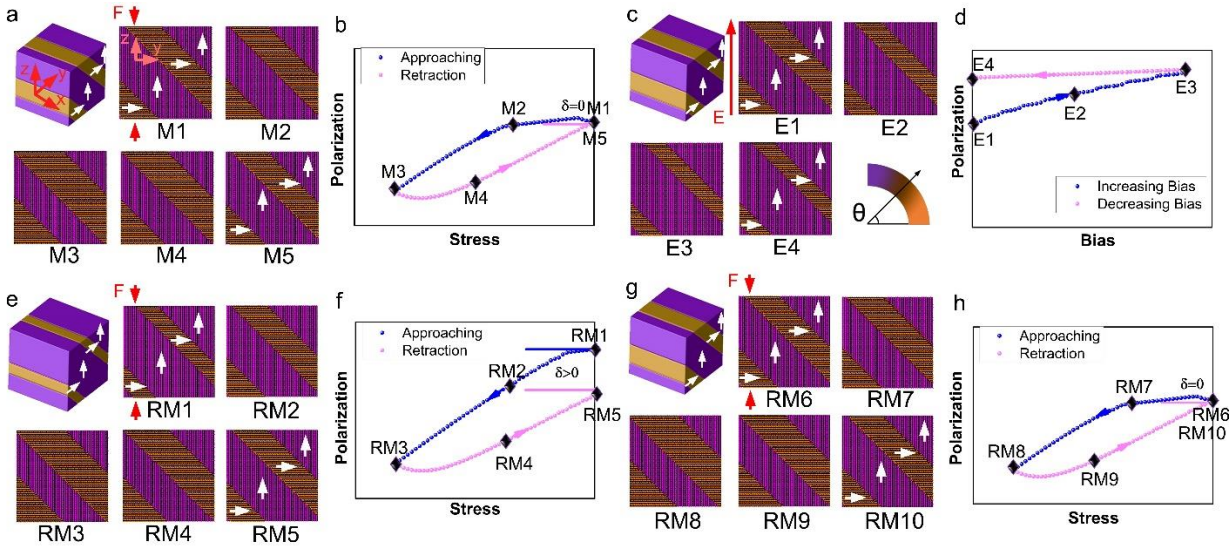

Figure 4-5 (a, c, e, g) Ferroelastic domain switching under a mechanical loading cycle, an electrical loading cycle, a mechanical loading and a repeat mechanical loading cycle respectively. White arrows represent the direction of polarisation. **(b, d, f, h)** A closed, open, open, closed polarisations–load curve corresponding to the phase-field modelling, respectively. The blue line indicates the approach (or increase of bias) and the pink line indicates the retraction (or decrease of bias) at the tip.

The change in the polarisation state δ before and after this mechanical cycle is zero. A nucleation regime to activate the domain transition from the c-domain to the a-domain exists at the beginning of the compressive loading process (see Figures 4-4 (b) and 4-5 (b)). After the domain-wall movement is activated, the polarisation varies linearly according to external stimuli, resulting from the soft pinning force upon the domain wall in the PMN-33%PT pillar. When a positive voltage bias is applied to the initial ferroelastic domain structure, an incubation stage for domain-wall movement to promote transition from a-domain to c-domain is not obvious (see Figures 4-5 (c) and 4-5 (d)). However, in the voltage bias unloading process, domain-wall movement is pinned as a consequence of the requirement of large activation energy. Thus, the domain structure cannot be reversed in this electrical loading–unloading cycle, as is shown in Figures 4-5 (c) and 4-5 (d).

Interestingly, applying mechanical loading after a cycle of electrical loading shows that the generated polarisation introduced in an electrical loading–unloading cycle is erased by

mechanical compression (Fig. 4-5(e)). In consistence to Fig. 4-4(b), the original ferroelastic domain configuration is recovered by applying a mechanical loading–unloading cycle. As a result, the stress-polarisation loop is not a closed one (Fig. 4-5(f)), i.e., the change of polarisation δ is not zero. After the first mechanical loading–unloading cycle after electrical cycles, the second mechanical loading–unloading cycle is applied, in which reversible domain switching is recovered again as shown in Fig. 4-5(g) and 4-5(h). The phase-field simulation results are consistent to the proposed domain switching kinetics as shown in Fig. 4-4(b).

4.2.5. A mechanical loading cycle following an electrical loading cycle

To confirm the phase-field simulation, an experiment on mechanical loading–unloading cycles following an electrical loading cycle was conducted. After an electrical loading cycle, mechanical loading–unloading cycles were applied to the same area, as shown in Figure 4-6. The load/bias–time curve for the first mechanical loading cycle is shown in Figure 4-6 (b). The domain configuration shown in the first image in Figure 4-6 (a) was the backswitched configuration after an electrical loading cycle (see the last image in Figure 4-3 (a)). Again, increasing mechanical loading led to the expansion of the a-domain that reached its maximum size under the highest load. After unloading, the a-domain shrank but did not return to its original size and shape—that is, the size of the c-domain was smaller than it was before mechanical loading, which confirms the simulation result depicted in Figure 4-5: that domain switching is partially reversed.

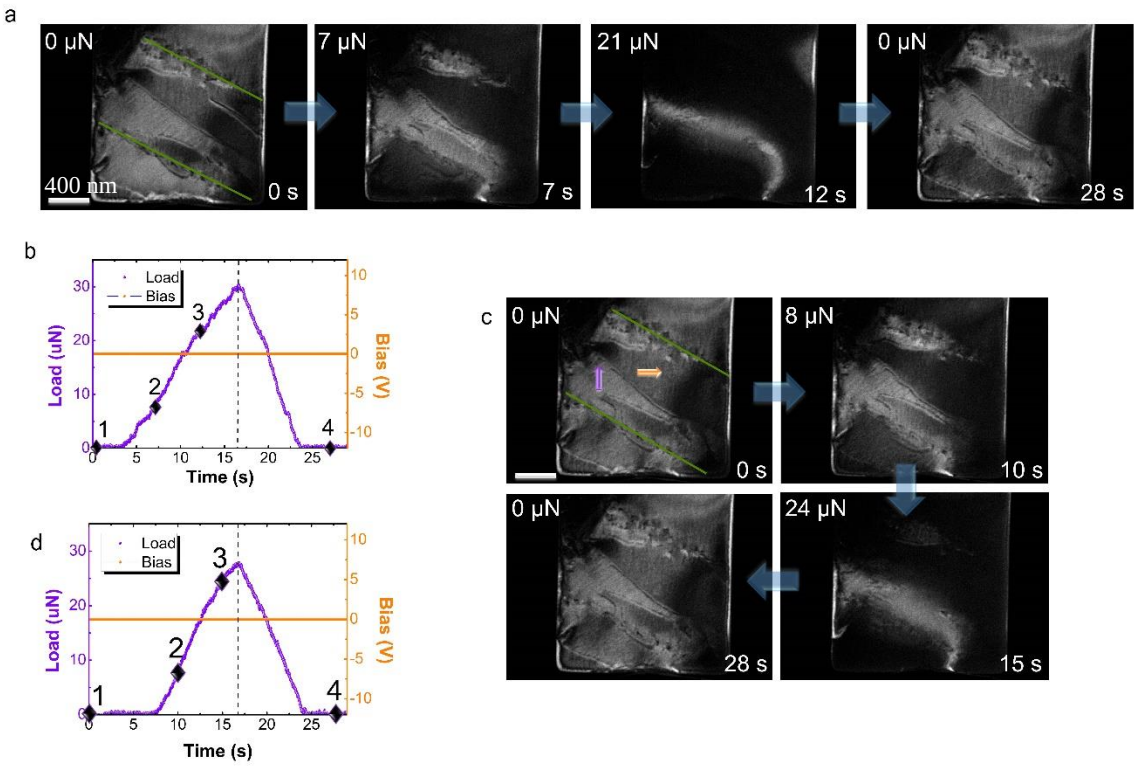

Figure 4-6 A series of images of ferroelastic domains responding to the first mechanical loading–unloading cycle **(a)** and the second mechanical loading–unloading cycle (**c)** after an electrical loading cycle. **(b, d)** The corresponding load/bias–time curves in which the highest load was restricted to ~ 28 μN.

4.2.6. A mechanical loading cycle following a mechanical loading cycle

The effects of mechanical loading on the second and subsequent mechanical loading cycles are shown in Figure 4-6 (c) and the corresponding load–time curve is presented in Figure 4-6 (d). The initial domain configuration (see the first image in Figure 4-6 (c)) is the same as the final domain configuration presented in the final image of Figure 4-6 (a). After a complete mechanical loading–unloading cycle, the domain configuration returned to its original structure, suggesting that the previous mechanically irreversible state (see Figure 4-6 (a)) was converted to a mechanically reversible state after the first mechanical loading–unloading cycle. The mutually combining effect of two continuous mechanical cycles indicates that the reversible nature of the ferroelastic domains is repeatable.

4.2.7. An electrical loading cycle following an electrical loading cycle

Figure 4-7 shows the ferroelastic domain evolution during two repeated electrical loading cycles that was conducted to investigate the effect of electrical loading on mechanically irreversible domains. Figure 4-7 (a) shows head-to-tail, 90° domains during the first electrical loading cycle. A bias was increased from 0 V to +10 V at a rate of 1 V/s and maintained at +10 V for 10 seconds as shown in Figure 4-7 (c). The experiment showed that maintaining the bias at +10 V for a time does not have any impact on the results. The c-domain expanded and dominated most of the observed area after unloading, as shown in the fourth image in Figure 4-7 (a). The domain structure evolution during the second loading cycle is shown in Figure 4-7 (b). The same load function was applied, as depicted in Figure 4-7 (d). Domain configuration did not change after the second electrical loading cycle.

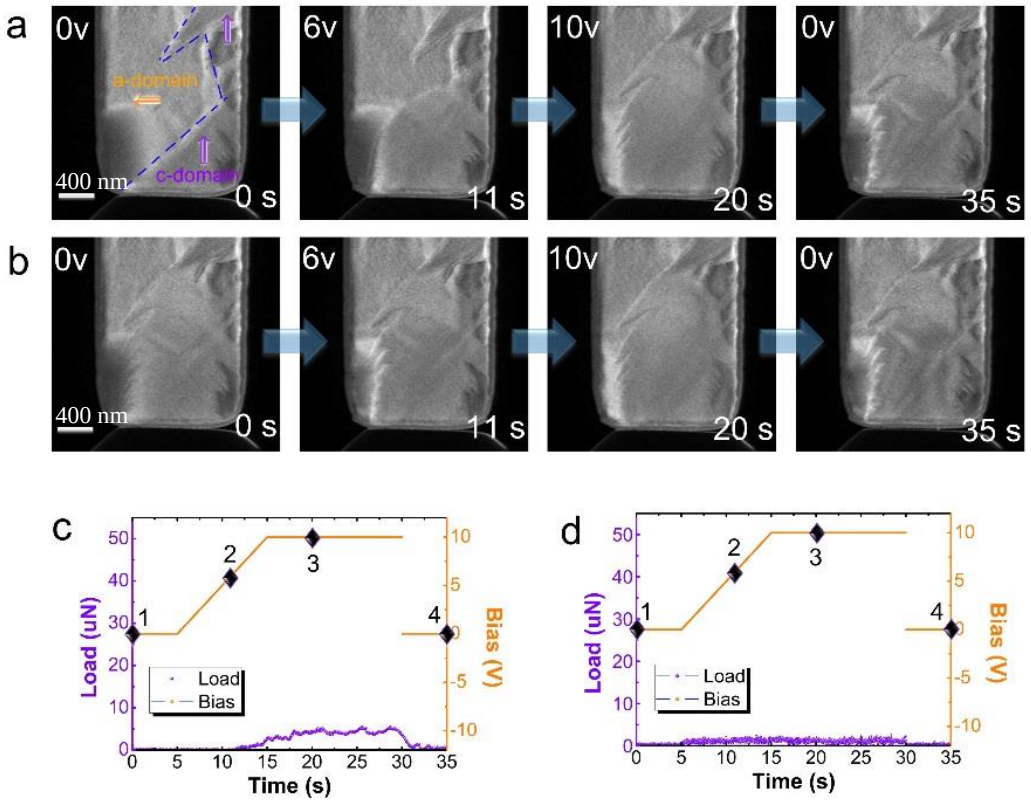

Figure 4-7 (a, b) A series of images showing the evolution of ferroelastic domains under electrical loading. **(c, d)** A load/bias–time curve to (a) and (b) respectively.

Following the two electrical loading cycles, the domains were subjected to a mechanical loading of ~ 47 μN to investigate their mechanical reversibility, as shown in Figure 4-8 (the load function is presented in Figure 4-8 (c)). The a-domain shrank and returned to its pre-electrical loading morphology, as illustrated by the first image of Figure 4-7 (a). Ferroelastic domains and polarisation partially reversed (relative to the final image of Figure 4-7(a)), indicating that the domains, after the second electrical loading cycle, are still mechanically irreversible. Figures 4-8 (b) 4-8 (d) indicate the effects of the second round of mechanical loading and the corresponding load function. Full recovery of domain structures was observed.

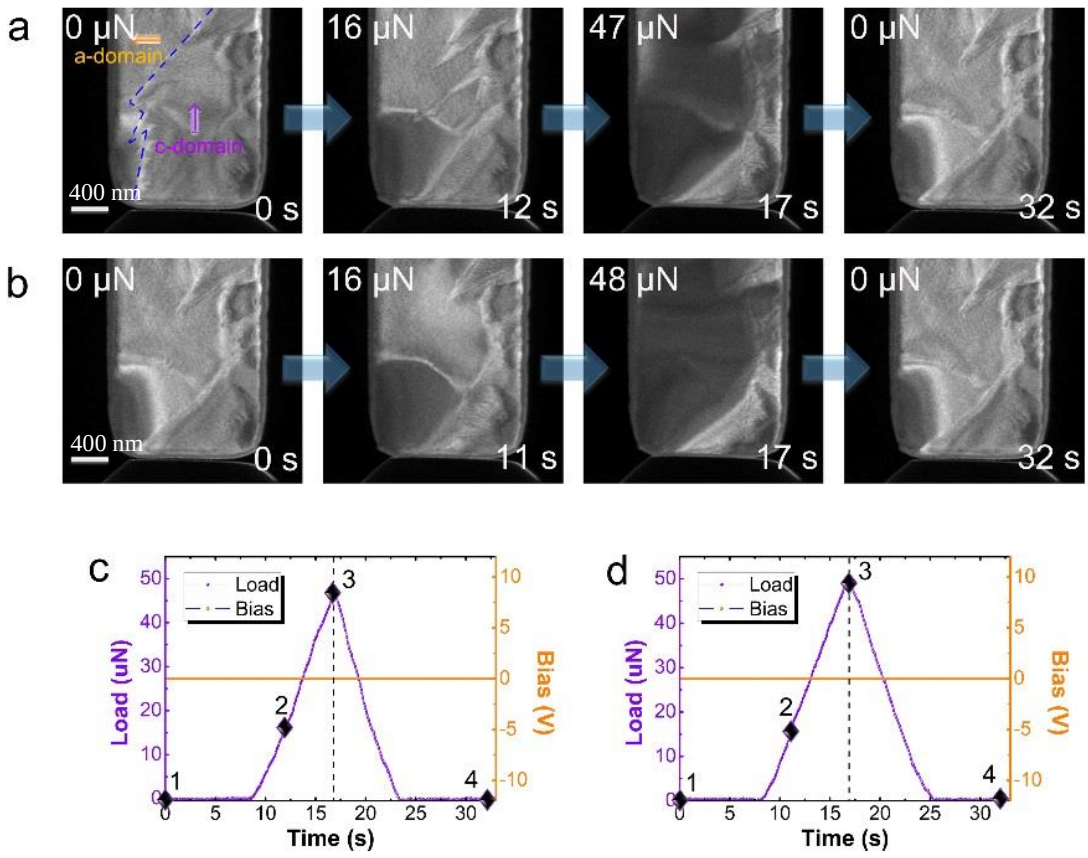

Figure 4-8 (a, b) A series of images showing the evolution of ferroelastic domains under mechanical loading. **(c, d)** A load/bias–time curve to **(a)** and **(b)** respectively.

4.2.8. The repeating of loading cycle tests for ferroelastic domain switching

The observed phenomenon is repeatable for either the same or different pillars. Section 4.2.7 shows the same phenomenon in a different pillar compared with that of the main text. More pillars were tested (not shown here) using the same method and confirming the same observation. Figure 4-9 shows series images for the repetition of loading cycles two, five and 10 times, wherein all logical expressions are valid.

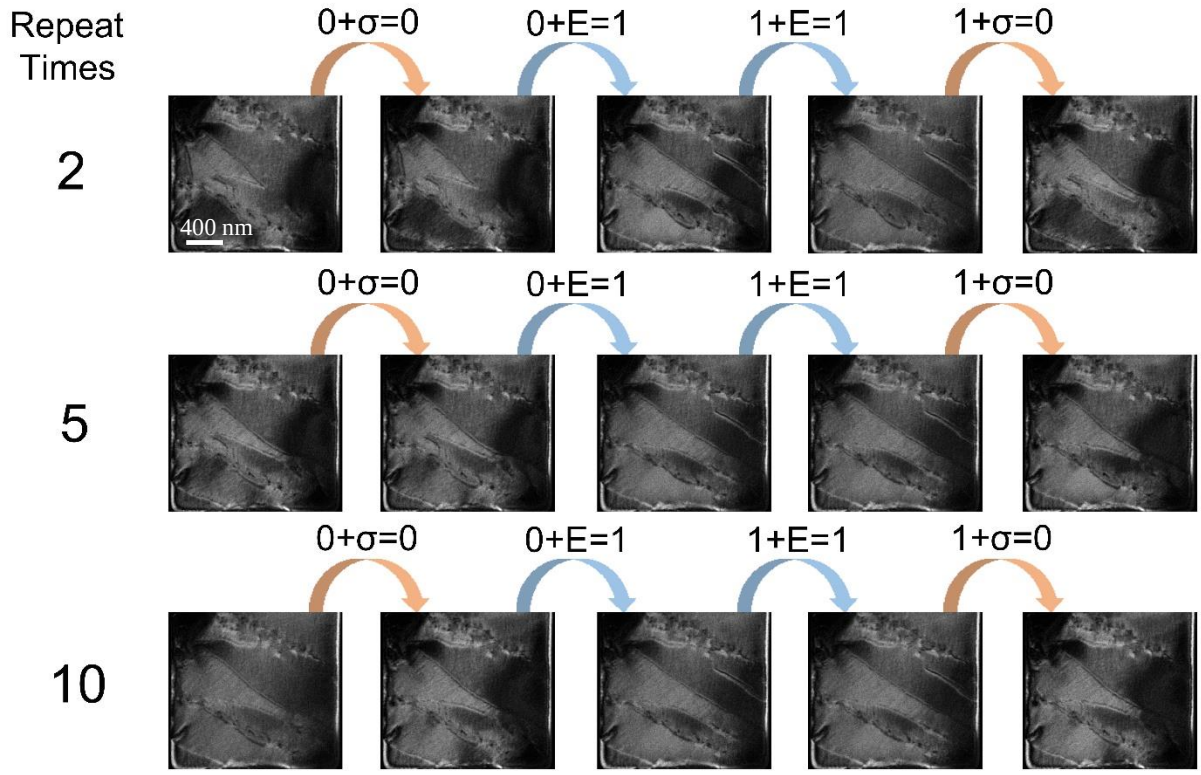

Figure 4-9 All logical expressions are valid even after 10 repetitions.

4.3. Writing and reading bit processes

It is now clear that an electrical loading–unloading cycle introduces the mechanically irreversible state and a subsequent mechanical loading–unloading cycle brings the domain configuration back to the mechanically reversible state. By taking advantage of these phenomena, an advanced writing and reading approach for non-volatile memories is proposed. In the following discussion, the mechanically reversible state—that is, $\delta = 0$ in the polarisation–

stress curve after a mechanical loading–unloading cycle—is defined as the logical signal 0, while the mechanically irreversible state—that is, δ>0 after a mechanical loading–unloading cycle—is defined as the logical signal 1.

When a-domains in a mechanically reversible state is subjected to a mechanical loading cycle, the mechanically reversible state remains. This provides the first logical expression:

$$Reversible\ state + mechanical\ loading\ cycle = reversible\ state$$

$$0 + \sigma = 0 \tag{4-6}$$

If the mechanically reversible state is subjected to an electrical loading cycle, it becomes a mechanically irreversible state, which can be expressed by:

$$Reversible\ state + electrical\ loading\ cycle = irreversible\ state$$

$$0 + E = 1 \tag{4-7}$$

When a mechanically irreversible domain experiences a mechanical loading cycle, its state switches to a mechanically reversible one:

$$Irreversible\ state + mechanical\ loading\ cycle = reversible\ state$$

$$1 + \sigma = 0 \tag{4-8}$$

Mechanically irreversible domains remain after another electrical loading cycle, therefore:

$$Irreversible\ state + electrical\ loading\ cycle = irreversible\ state$$

$$1 + E = 1 \tag{4-9}$$

These four logical expressions provide the fundamental rules for logical identification for writing and reading bits. The ways of writing bits by mechanical and electrical excitations and reading bits by mechanical excitation are illustrated in Figure 4-10 (a), in which a 4-cell

matrix has the original logical states of Aa(1), Ab(1), Ba(0) and Bb(0) (see the first matrix in Figure 4-10 (a)). Based on the four logical expressions, applying mechanical stress to cells Aa and Ba and electrical loading to cells Ab and Bb leads to the logical states of Aa(0), Ab(1), Ba(0) and Bb(1), as shown in the second matrix in Figure 4-10 (a). Reading the logical states in the four cells is achieved by applying mechanical stress to each of the cells and this process results in a logical state of zero for all four cells, as shown in the third matrix in Figure 4-10 (a). Local polarisation change (δ) before and after mechanical excitation is used to determine the logical signal of each cell during reading. Aa and Ba follow rule (1) where $\delta = 0$, while Ab and Bb follow rule (3) where $\delta \neq 0$. As has been defined above, we receive a reading of zero if $\delta = 0$ and of one if $\delta \neq 0$, as shown in Figure 4-10 (b).

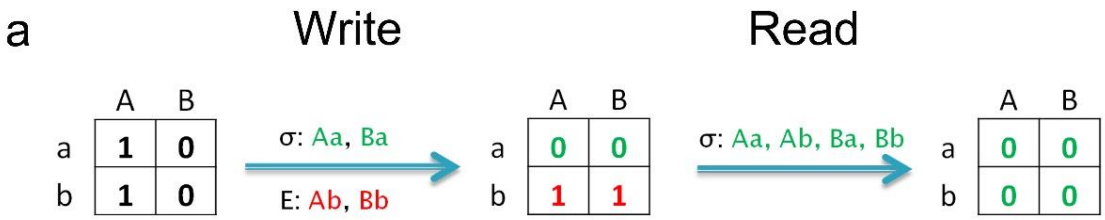

b

Cell	Before	σ	After	Detect	Read
Aa	0	→	0	δ=0	0
Ab	1	→	0	δ≠0	1
Ba	0	→	0	δ=0	0
Bb	1	→	0	δ≠0	1

Figure 4-10 (a) Mechanically reversible domains are denoted as the logical signal 0, while mechanically irreversible domains are signified by the logical signal 1. In the writing process, by applying the bias to cells Ab and Bb and mechanical loading to cells Aa and Ba, the logical states of the four cells become Aa(0), Ab(1), Ba(0) and Bb(1), which are independent of their initial states. In the reading process, mechanical loading is applied to the cells and transfers logical states in the cells to the mechanically reversible state (0). **(b)** By detecting the change of the polarisation δ, cells are read 0 when $\delta = 0$ or 1 when $\delta > 0$. Cells are therefore read Aa(0), Ab(1), Ba(0) and Bb(1).

The present chapter aims to provide an advanced way to achieve writing and reading for non-volatile memories, which could overcome the oft-observed, long-standing backswitching problem with ferroelectric memories. A combination of mechanical and electric routines will be utilised to realise the four logical states of Aa(1), Ab(1), Ba(0) and Bb(0) proposed by our manuscript, then the corresponding mechanical and electrical processing will be performed.

In general, compared to traditional electric writing and reading processes, ferroelectric domain writing and reading by mechanical methods has several advantages, including 1) generating stable domain patterns that exhibit no relaxation for several days after switching, 2) demonstrating no damage to the sample surface caused by a high loading force and 3) writing entirely in nanoscale with a size of less than 10 nm, which can be quite localised. The nanoscale characteristics were quite favourable for high-density memory applications[80, 304, 305]. However, the present two memory state was distinguished by whether δ equalled zero or not, causing difficulties in the designs of the corresponding reading circuit. This led me to carefully consider the future possible routines for more convenient reading and writing.

4.4. Summary

In conclusion, in-situ TEM experiments and phase-field modelling have been used to explore the mutually combined effects of mechanical stress and electric loading on the ferroelastic domain structures in PMN-33%PT. The results showed that domain structures can exist in mechanically irreversible or mechanically reversible states, depending on whether the structures have been subjected to electrical or mechanical excitation. This domain switching behaviour is different to that of other traditional ferroelectric material because of the low and asymmetric energy barriers among different domains. The extensive application of these two states can be conceptually used for non-volatile memories, representing the logical signals 0 and 1 respectively. Since the logical signals do not need to measure the polarisation states, the ferroelastic/ferroelectric domain backswitching no longer leads to data loss in the memories.

Therefore, the reliability of the non-volatile memories is significantly enhanced. Further, the new writing and reading methods allow for the use of ferroelastic domains (e.g., the 90° domains used in this investigation) and, therefore, significantly broaden the number of candidate materials for non-volatile memories.

Chapter 5

The facilitation of ferroelectric switching via the mechanical manipulation of hierarchical nanoscale domain structures

5.1. Introduction

Ferroelectric materials, exhibiting the intrinsic coupling of spontaneous polarisation and strain, have been extensively investigated for their critical applications in next-generation logical devices, non-volatile memories, actuators and sensors[76, 82, 306-308]. A low-threshold field for ferroelectric domain switching is important in advanced applications for low energy consumption. Lowering the threshold field requires comprehensive understanding of domain switching kinetics under external stimuli, including temperature[159, 289], electrical bias[145, 165, 167, 176, 199, 260, 282] and/or mechanical stress[80, 183, 283]. Recent investigations have demonstrated that domain orientation has significant effects on polarisation hysteresis, coercive fields, remnant polarisation and the dielectric and piezoelectric properties of ferroelectric materials under electrical bias stimulation[198, 309, 310]. These effects can result from the fact that the nucleation barriers for the ferroelastic domain walls are smaller in specific directions, leading to a high density of ferroelastic domain walls that promotes ferroelastic transition and consequently facilitates ferroelectric transition[176].

Previous investigations of domain switching kinetics have most often been conducted using epitaxial ferroelectric films[277, 305, 311]. While ferroelectric switching (180° domain

switching) in these films can be facilitated by ferroelastic transitions (non-180° domain switching), it usually requires the delicate selection of a crystalline direction and the proper design of epitaxial ferroelectric films[198, 311], including the selection of the substrate and film materials and film thickness. Further, the motion of the ferroelastic domain walls in epitaxial thin films is usually restricted by the elastic constraint of the substrate that limits the ferroelastic transition[190]. In bulk ferroelectric materials without constraint by any substrate, the formation of freely mobile ferroelastic domain walls requires relatively low energy, making it possible to promote ferroelectric switching via ferroelastic transition[151, 172]. Therefore, it is of significant interest to explore a controllable way to manipulate high density and freely mobile ferroelastic domain walls and to understand the microscopic mechanisms for the interaction of ferroelastic and ferroelectric switching in bulk ferroelectrics.

Recent developments in in-situ TEM have provided a platform for applying simultaneously multiple stimuli to micro- and nanoscale specimens[145, 184, 190], measuring their physical and mechanical properties and studying their structural evolutions under external stimuli. This has made it possible to conduct a real-time examination of polarisation switching. For this chapter, we applied in-situ TEM and phase-field modelling to investigate the heterogeneous ferroelastic transition process (the coexistence of nano- and micro-ferroelastic domains) by applying mechanical loading and to explore its significant assistance to ferroelectric transition under simultaneous mechanical and electrical loading in PMN-38%PT single crystals with tetragonal domains[128] at room temperature. The formation of a high density of tetragonal domains in normal ferroelectrics usually requires a biaxial constraint in thin films[177, 184]. This limits significantly the motion of ferroelastic domain walls. For relaxor-based ferroelectric PMN-38%PT, the energy barriers for domain nucleation and motion within tetragonal domains are expected to be significantly lower than those of normal ferroelectrics—for example, $PbTiO_3$ and $PbZr_{0.2}Ti_{0.8}O_3$—because they are close to the MPB of PMN-xPT[151].

As a result, it is possible to have a high density of 90° ferroelastic domains in a PMN-38%PT single crystal without it being biaxially constrained in thin films. Our phase-field simulations and in-situ TEM observations demonstrated a decreased threshold value in the external electric field for ferroelectric switching through the manipulation of ferroelastic 90^{o} nanodomains by mechanical loading. These results have significantly advanced our fundamental understanding of how mechanical loading assists polarisation reversal and provides a new way for the manipulation of high-density mobile ferroelastic domain walls in bulk single crystals.

5.2. Experiments

5.2.1. Materials synthesis and characterisation

The PMN-38%PT single crystal was grown using a modified Bridgman method. Micro-pillars were prepared using FIB milling in a Zeiss Auriga SEM. A bulk PMN-38%PT specimen was first mechanically polished to a thickness of ~ 1 μm at the edge. A long bar with dimensions of 9 μm × 70 μm × 1 μm was cut from the thin edge of the specimen using an FIB and was lifted using a tungsten manipulator and placed on a pre-cut Cu base. Pt deposition was used to fix the bar onto the Cu base. Pillars were cut from the long bar using the FIB, which was operated at 30 kV and 50 nA for coarse milling and 10 kV and 10 nA for fine milling. A thick pillar was retained between two neighbouring thin pillars, effectively preventing materials' deposition from one thin pillar to another during the FIB processing. TEM observations were carried out using a JEOL 2100 microscope operated at 200 kV. In-situ mechanical stressing and electrical biasing were conducted using a Hysitron PI 95 TEM Picoindenter with a flat conductive tip. Stress was applied to pillars by moving the flat conductive tip towards the pillars in the displacement-control mode with displacement rates for both approach and retraction of 3 nm/s. The bias was supplied by a Keithley 2602A SourceMeter integrated in the ECM. Gentle contact between the conductive tip and the pillar was held for the closed-loop electrical loading experiment. The bias was raised from 0 V to +5

V between five and 15 seconds with a ramping rate of 0.5 V/s. High-resolution STEM-HAADF images were obtained using a JEOL ARM 200 STEM equipped with a spherical-aberration corrector operated at 200 kV.

5.2.2. Experiment setup

Figure 5-1(a) presents a schematic of the in-situ experiment setup. A bulk PMN-38%PT single crystal was fixed on a Cu base using Pt deposition. Multiple PMN-38%PT pillars with dimensions of 2.0 μm × 1.3 μm × 0.08 μm (length × width × thickness) were produced using mechanical grinding, followed by FIB processing. In-situ mechanical and electrical stimuli were applied using a conductive probe under the TEM. The Cu base acted as one electrode and the conductive probe as the other electrode. A typical domain configuration observed from a pillar is presented in Figure 5-1 (b). Lamellar-like domains with bandwidths of hundreds of nanometres at a 45° inclination were found in the pillar. The STEM-HAADF technique was used to image the polarisation directions and the domain-wall structures. Figure 5-1 (b) shows an example of an HAADF image in which a domain wall separating the head-to-tail tetragonal domains was marked by a blue solid line. All domains in the pillar were examined, confirming the overall head-to-tail domain orientation of the pillar.

In this chapter, tetragonal domains with polarisation along the positive and negative [100], [010] and [001] axes are referred to as $P_1^{+/-}$, $P_2^{+/-}$ and $P_3^{+/-}$ respectively. Through the measurement of the displacement between Pb cations and their surrounding Mg/Nb/Ti cations in the HAADF image in Figure 5-1 (b)[231], the polarisations of the domains on the left (P_3^+) and right (P_1^-) sides of the domain wall were determined by pointing towards [001] and [$\bar{1}$00] respectively (see the details in the enlarged purple and orange boxes in Figure 5-1 (b)). The structure of the alternating head-to-tail, 90° domains with straight P_3^+/P_1^- domain walls inside

the initial domain configuration in this PMN-38%PT single-crystal pillar was therefore identified.

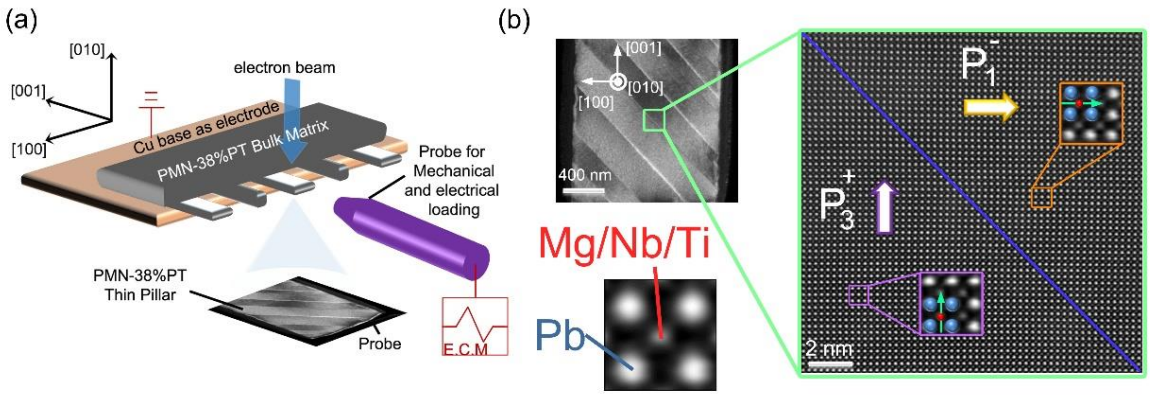

Figure 5-1 (a) Schematic diagram of the experiment setup. A bulk PMN-38%PT matrix with thin pillars was fixed to a grounded Cu platform using a Pt deposition. A conductive tip connected to the ECM acted as an indenter and electrode for the mechanical and electrical loading. The actual allocation of the pillar and the tip was captured by the enlarged TEM image. **(b)** A dark-field TEM image and an STEM-HAADF image showing a head-to-tail tetragonal domain configuration across a domain boundary as indicated by the green box. The domain wall is indicated using a blue line, while polarisations are indicated using large purple and yellow vectors. The intersecting purple and yellow boxes show the enlarged polarisations in the $\boldsymbol{P_3^+}$ and $\boldsymbol{P_1^-}$ domain areas respectively.

5.2.3. Domain switching kinetic under electric loading

An electrical-loading-induced domain switching is presented in Figures 5-2 (a)–5-2 (d). For the convenience of the discussion of the observed phenomena, domain configurations in the area highlighted by the green box in Figure 5-2 (a) are schematically drawn at the bottom of Figure 5-2, where the four drawings from the left to the right correspond to the green box area in Figures 5-2 (a)–5-2 (d). The initial domain configuration is shown in Figure 5-2 (a). With an increase in the bias from 0 V to +3 V (not shown here), the domain configuration did not change, as an electrical field is not large enough to initiate polarisation reversal[190] when $E_i \Delta P_i < 2P_s E_c$, where E_i is the electric field, ΔP_i is the change of polarisation vector, P_s is the spontaneous polarisation and E_c is the coercive field[175].

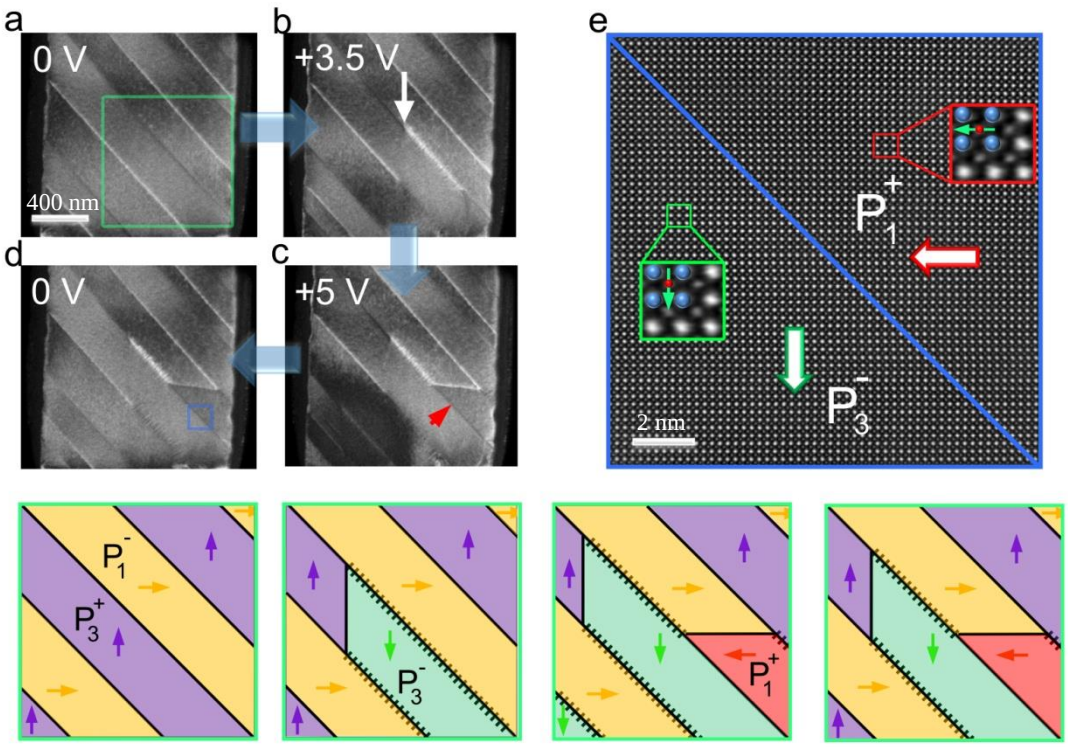

Figure 5-2 (a–d) A series of images showing the evolution of ferroelastic domains under electrical loading. On the bottom of the images are the schematic drawings of the area indicated by the green box. Drawings from left to right represent **(a–d). (e)** An STEM-HAADF image showing a head-to-tail, tetragonal domain configuration across the domain boundary, as indicated by the blue box in **(d)**. The domain wall is indicated using a blue line, while polarisations are indicated using large green and red vectors. The inset green and red boxes show enlarged HAADF images from which the local polarisation of the $\boldsymbol{P_3^-}$ and $\boldsymbol{P_1^+}$ domain areas was determined.

When the bias was larger than +3 V, a vertical domain wall formed, as is indicated by the white arrow in Figure 5-2 (b); this was followed by the expansion of the new domain with a different contrast. This process led to the formation of a zipper-like pattern accompanied by contrast reversal at the original micro-domain walls, as indicated by the white arrow (see Figure 5-2 (b)). Further increasing the bias to over +3.7 V, a horizontal domain wall formed in the neighbouring P_1^- domain. Interestingly, after the formation of the horizontal domain wall, the zipper-like pattern disappeared (as indicated by the red arrow) from between the two newly formed domains, as shown in Figure 5-2 (c). With the increase of the bias, these newly formed domains kept expanding along the original bulk domain walls. After bias unloading, partial

backswitching occurred because of the intrinsic surface electrostatic and internally spontaneous strain-induced elastic energy[280, 281], as illustrated by Figure 5-2 (d). An STEM-HAADF image from the blue box area in Figure 5-2 (d) is shown in Figure 5-2 (e). On the left and right hand sides of the domain wall, polarisation is discovered to be pointing down (P_3^-) and left (P_1^+), as indicated by the green and red arrows respectively. This indicates a new 90° head-to-tail P_3^-/P_1^+ uncharged domain wall that was formed under electrical poling. Ferroelastic domains can be reversed to 180° if an opposite electrical bias to the original dipole direction is applied[161]. When a bias is larger than +3 V, the electrical field is large enough to initiate 180° polarisation reversal, forming vertical, neutrally charged 180° domain walls in the original P_3^+ domains and minimising the electrostatic energy. Along with the formation of P_3^- domains, charged P_3^-/P_1^-, tail-to-tail domain walls were created, which is energetically unflavoured. To compensate for the significantly charged domain-wall energy and to allow for the creation of a neutral bound charge, the zipper-like domain wall was formed. Accompanying these nanodomain walls, the P_3^-/P_1^- 90° domain wall became zipper-shaped. Under an electrical field along P_3^- direction, 90° ferroelastic domain switching of P_1^- is generally unfavourable in comparison with 180° ferroelectric switching because of the large energy penalty (extra elastic energy) associated with the 90° ferroelastic reversal that occurs to accommodate such switching events[184]. Therefore, when the in-plane electrical field caused by the large bound charge density at the domain boundary was sufficiently large[184], the P_1^+ domain associated with the 180° P_1^-/P_1^+ ferroelectric domain wall formed. Because of its association with the P_1^+ expansion, the charged P_3^- / P_1^- domain wall became a neutral P_3^- / P_1^+ domain wall, resulting in the disappearance of the zipper-shaped domain wall.

5.2.4. Effects of positive and negative biases

Figure 5-3 shows the effects of positive and negative biases on ferroelectric switching. Figure 5-3 (a) exhibits the domain configuration after electric poling with a bias of +5 V—the

same configuration as that presented in Figure 5-2 (d). Applying a gradually increased negative bias gradually erased the originally switched domains (see Figures 5-3 (b)–5.3 (c)) until the switched domains were completely removed (see Figure 5-3 (d)). This domain configuration remained after unloading the electrical bias. Such completely reversible domain switching by applying opposite electrical fields returned the original domain configuration, allowing for the comparison of electrical poling effects with and without mechanical confinement.

The positive–negative cycle can be repeated. As can be seen in Figures 5-3 (e)–5.3 (h), a positive bias of +5 V was again applied to the pillar. Here, exactly the same domain configuration as that shown in Figure 5-3 (a) was achieved (see Figure 5-3 (h)).

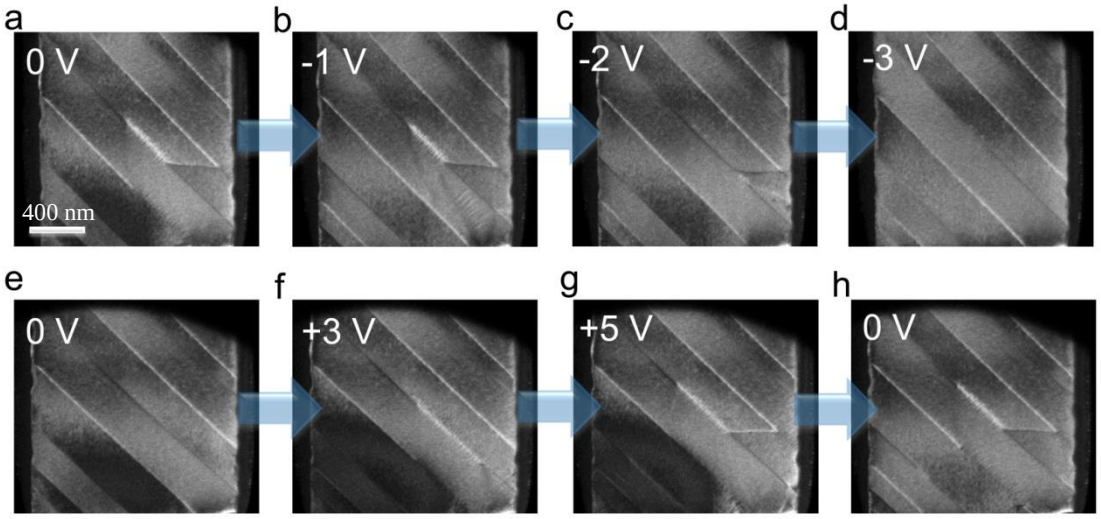

Figure 5-3 The effects of positive and negative biases on a single-crystal PMN-38%PT pillar. **(a–d)** Negative bias was applied to the pillar that was previously poled by a +5 V bias. **(e–h)** A positive bias of +5 V was repeatedly loaded onto the same pillar. The same poling result as shown in Figure 5-2 was achieved.

5.2.5. Domain switching kinetics under mechanical loading

Electrical loading led to 180° ferroelectric domain reversal in the micro-tetragonal domains but it did not alter the ferroelastic domain structure. Generally, the nucleation energy barrier of ferroelastic 90^{o} domain walls is lower than that of ferroelectric 180° domain walls in single crystals, without a significant pinning force against the 90° domain walls[176, 312]. However,

my experiment results, shown in Section 5.2.3, suggest ferroelectric switching, rather than the motion of ferroelastic domain walls. Therefore, there could be a relatively strong pinning effect on the micro-ferroelastic domain walls in the present PMN-38%PT single crystal, which could originate from the existence of oxygen vacancy, topological defects or compositional variations in relaxor-based ferroelectrics[300, 313-315].

Domain switching under mechanical loading presents a markedly different picture from electrical loading. Figures 5-4 (a)–5-4 (e) depict the evolution of domain configurations during a mechanical loading cycle (see Figure 5-4 (g)). The domain configurations in the green box area (see Figure 5-4 (a)) are schematically illustrated at different stress stages in the lower parts of Figures 5-4 (a)–5-4 (e). The initial domain configuration with alternate P_3^+/P_1^- domains is shown in Figure 5-4 (a). At the stress level of 8.6 MPa, some straight nano-bands with orientations perpendicular to the original P_3^+/P_1^- domain wall formed, as is indicated by the white arrow in Figure 5-4 (b).

Analysis of the newly formed structures (see the below Section 5.2.5.1) indicates that the straight bands are new P_1^+ domains with charge neutral head-to-tail 90° P_3^+ / P_1^+ walls perpendicular to the original micro-domain walls, as illustrated in the lower part of Figure 5-4 (b) in red colour. Upon increasing the stress to 55.8 MPa, straight bands with orientations parallel to the original micro-domain walls formed, as shown in Figure 5-4 (c). It turns out that the straight nano-bands parallel to the micro-domain walls are newly switched P_1^- domains with P_3^+/P_1^- domain walls. My experiment results show that the original micro-domain wall positions, as indicated by the dotted lines in the lower part of Figure 5-4 (c), shifted slightly as a consequence of the shrinkage of the P_3^+ domains. While the motion of the micro-domain walls was limited when the stress was further increased, the density of the new nanodomains increased dramatically (see Figure 5-4 (d)). Once the external stress was removed, the switched

domain fully reversed: the new nanodomains disappeared and the micro-domain walls returned to their original positions (see Figure 5-4 (e)). Note that the original P_1^- domains remained unchanged during the mechanical loading cycle, because P_1^- domains are favourable for compression along [001], as is schematically shown in Figure 5-4 (f). Since the pillar was close to a two-dimensional material with significant (010) surfaces, the polarisation switching to $P_2^{+/-}$ would induce a significant electrostatic field which is not desirable and therefore was not detected in the experiment. Figure 5-4 (g) shows the corresponding loading stress–time curve. Because the loading and unloading processes were displacement control with a constant displacement rate, the approximate linear stress–time curve for approach and retraction indicated that the deformation process of the pillar was elastic without obvious bending.

The application of mechanical loading significantly modified the domain orientation, which could have affected the electrical poling process. Macroscopic studies on mechanical loading with electrical poling[316] reported that the electric field–polarisation hysteresis as well as the ferroelectric properties were completely different from those that merely underwent electrical poling. Such difference was significant when the compressive stress was larger than 20 MPa. A possible mechanism was proposed whereby all P_3^+ domains were converted to a single P_1^- domain through the motion of the original micro P_3^+ / P_1^- domain walls with mechanical loadings of over 20 MPa[316, 317]. However, my experiment results proved contrary to the effectiveness of this proposed mechanism. With pinned micro-ferroelastic domain walls and relatively low energy barriers for domain nucleation and motion within micro-domains, compressive stress favoured the formation of a high density of ferroelastic 90° nanodomains inside the micro- P_3^+ domains, indicating that the difference in electrical poling dynamic was a consequence of the formation of 90° nanodomains.

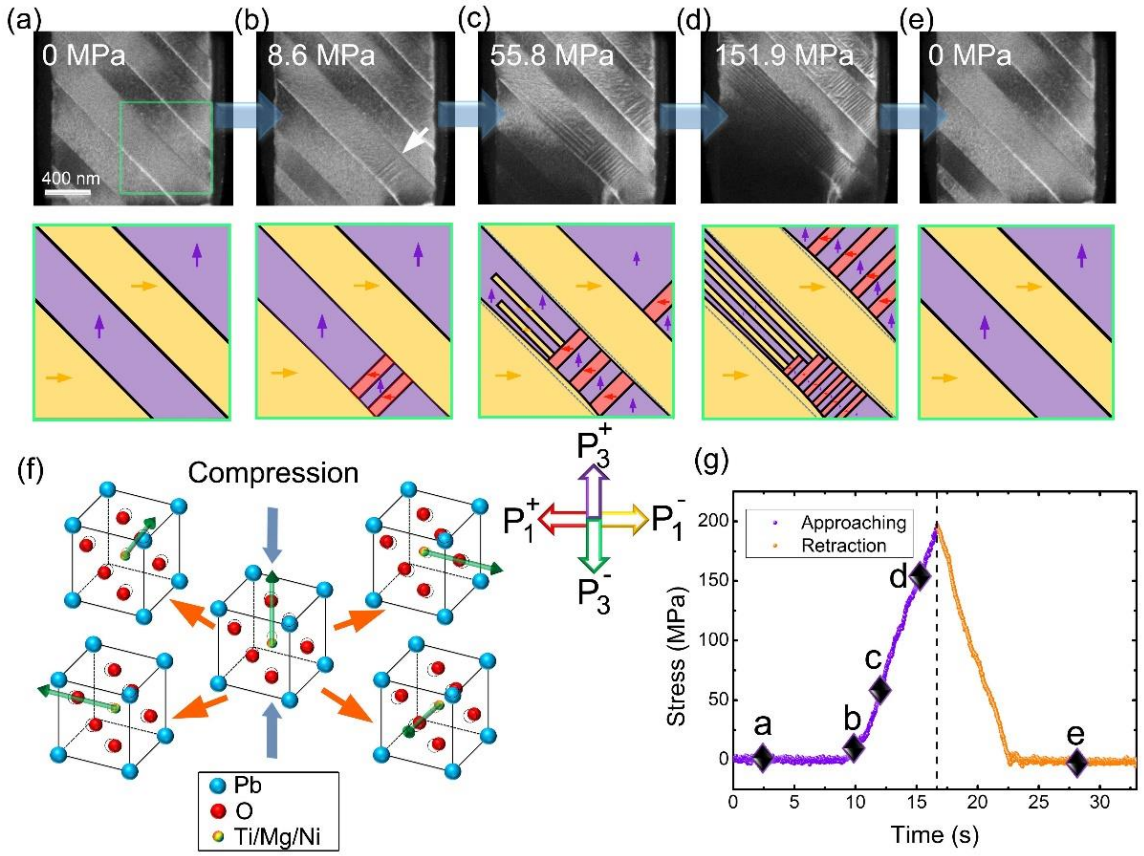

Figure 5-4 (a–e) A series of images showing the evolution of ferroelastic domains under mechanical excitation. At the bottom of each image is the schematic drawing of the domain structure from the area within the green box indicated in **(a). (f)** Schematic of the introduction of four possible types of polarisation by applying compression along [001] to the original polarisation along [001]. **(g)** A load/bias as opposed to a time curve showing the real-time application of a mechanical load with zero bias. Labels a to e correspond to the image order from a to e and indicate their relative positions on the curve.

5.2.5.1. Analysis of newly formed nanodomains

It is difficult to determine the polarisation of newly formed nanodomains under mechanical loading for the following two reasons: (1) they disappear after mechanical unloading and (2) it is not possible to conduct atomic-resolution STEM-HAADF imaging during mechanical loading. However, there is one possible way to analyse the polarisation of this type of nanodomain, as shown in Figure 5-5. When a large electrical bias was applied to a pillar with the original domain configuration depicted in Figure 5-5 (a), a completely different domain configuration with a high density of nanodomains—the same as that observed in Figure 5-4—formed, as revealed in Figure 5-5(c).

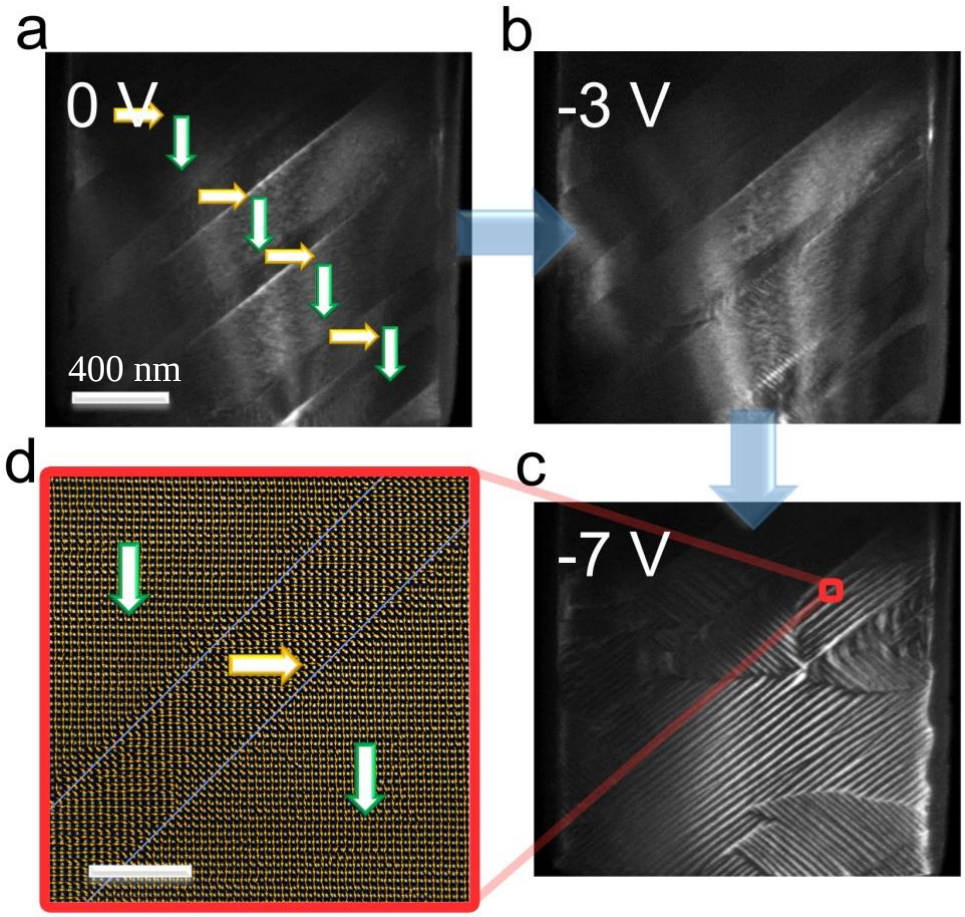

Figure 5-5 (a–c) Domain structure evolution with increasing negative bias against a pillar. **(d)** An enlarged HAADF-STEM image showing a 90° head-to-tail domain configuration.

Because the specimen was in contact with (and not mounted to) the probe during the experiment, the end that was connected to the probe was able to be slightly bended (because of the elongation of the sample) by the strong electrical-bias-induced current. Because such bending was constrained by the probe, the current distribution was non-uniform, introducing a significantly localised field that completely altered the domain configuration, leading to a strain-induced-like structure, as shown in Figure 5-4. This process was accompanied by pronounced levels of remnant strain that retained the high density of nanodomain configuration after the removal of the electrical bias, providing an opportunity to analyse the domain structure. An STEM-HAADF image obtained from the region marked with the red box in Figure 5-5 (c) clearly a shows a head-to-tail domain configuration (as seen in the enlarged STEM-HAADF image in Figure 5-5 (d)), indicating that the newly formed nanodomain walls were 90° domain walls.

5.2.5.2. Mechanical compressive loading on a bulk PMN-38PT specimen

Figure 5-6 shows a compression loading experimental result for a bulk PMN-38PT specimen. Ninety degree tetragonal nanodomains were present in the P_3 domains after mechanical stressing. Since it was a bulk specimen, the width of the specimen compared to the compression area was assumed to be infinite. Compared with the pillar sample shown earlier, this demonstrates the introduction of nanodomain arrays applied to different boundary conditions—limited width and infinite width—of the specimen.

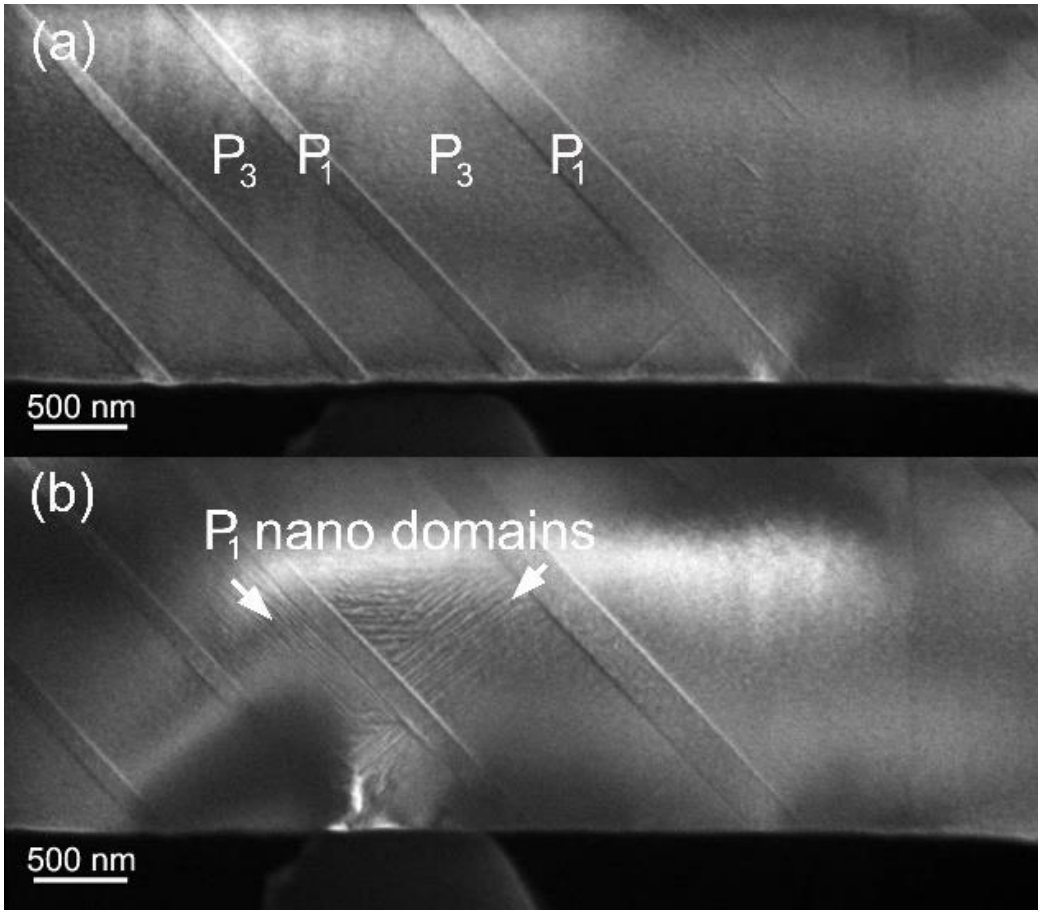

Figure 5-6 TEM images show microstructures in a bulk PMN-38PT sample **(a)** before and **(b)** after mechanical loading.

5.2.6. Phase-field simulations [†]

5.2.6.1. Phase-field model

A phase-field approach[250] was employed to study ferroelastic domain evolutions under electrical and mechanical stimuli by solving the time-dependent Ginzburg-Landau equation:

$$\frac{\partial P_i}{\partial t} = -L\frac{\delta F}{\delta P_i}, \tag{5-1}$$

Here, $P_i(i=1,2,3)$ are the three polarisation components and L is the kinetic coefficient. The total free energy of the system F is expressed as[318]:

$$F = \int_V \left[f_{bulk}(P_i) + f_{grad}(P_{i,j}) + f_{elas}(P_i, \varepsilon_{ij}) + f_{elec}(P_i, E_i) \right] dV, \tag{5-2}$$

Here, the bulk free energy f_{bulk}, the polarisation gradient energy f_{grad}, the elastic energy f_{elas} and the electric dipole interaction energy f_{elec} are included. The bulk free energy of the stress-free bulk PMN-38%PT is described using a sixth-order Landau polynomial:

$$\begin{aligned} f_{bulk} = {} & \alpha_1\left(P_1^2 + P_2^2 + P_3^2\right) + \alpha_{11}\left(P_1^4 + P_2^4 + P_3^4\right) + \alpha_{12}\left(P_1^2P_2^2 + P_1^2P_3^2 + P_2^2P_3^2\right) + \\ & \alpha_{111}\left(P_1^6 + P_2^6 + P_3^6\right) + \alpha_{112}\left[P_1^2\left(P_2^4 + P_3^4\right) + P_2^2\left(P_1^4 + P_3^4\right) + P_3^2\left(P_1^4 + P_2^4\right)\right] + \alpha_{123}P_1^2P_2^2P_3^2 \end{aligned}, \tag{5-3}$$

In this case, only α_1 is assumed to be temperature dependent and all coefficients are obtained from our thermodynamic study.

The polarisation gradient energy represents the domain-wall energy in the system. In this simulation, the isotropic gradient energy is assumed for the sake of simplicity, thus the polarisation gradient energy is expressed as[184, 292]:

[†] The phase-field modelling was conducted by Dr. Liang Hong under the guidance of Prof. Long-Qing Chen from Pennsylvania State University. (With permission from Dr. Liang Hong and Prof. Long-Qing Chen)

$$f_{grad} = \frac{G_{1111}}{2}\left(P_{1,1}^2 + P_{2,2}^2 + P_{3,3}^2 + P_{1,2}^2 + P_{1,3}^2 + P_{2,1}^2 + P_{2,3}^2 + P_{3,1}^2 + P_{3,2}^2\right), \quad (5\text{-}4)$$

Here, G_{1111} is the gradient energy coefficient.

The electrostrictive effect in PMN-38%PT produces the spontaneous deformation ε_{ij}^0 that is related to P_i. The elastic energy is[292]:

$$f_{elas} = \frac{1}{2} c_{ijkl}\left(\varepsilon_{ij} - \varepsilon_{ij}^0\right)\left(\varepsilon_{kl} - \varepsilon_{kl}^0\right), \quad (5\text{-}5)$$

Here, c_{ijkl} is the elastic stiffness tensor. The total strain $\varepsilon_{ij} = \bar{\varepsilon}_{ij} + \eta_{ij}$ is composed of the homogeneous strain $\bar{\varepsilon}_{ij}$ and the heterogeneous strain η_{ij}. The spontaneous strain is $\varepsilon_{ij}^0 = Q_{ijkl} P_k P_l$, where Q_{ijkl} signifies the electrostrictive coefficients measured by the experiments. The elastic strain is solved through the mechanical equilibrium condition $\sigma_{ij,j} = 0$ by using the microelasticity theory[294] of Khachaturyan and Shatalov.

Electrostatic energy is considered through the long-range interactions of spontaneous polarisations, which can be described as[296]:

$$f_{elec} = -\frac{1}{2}\varepsilon_0 k_{ij} E_i E_j - E_i P_i, \quad (5\text{-}6)$$

In this case, ε_0 is the vacuum permittivity and k_{ij} is the relative background dielectric constant tensor. For the sake of simplicity, we assume that $k_{ij} = 0$ when $i \neq j$. The Gauss-Seidel iteration method with an error tolerance of 10^{-4} was applied to solve the electrostatic equilibrium condition $-\varepsilon_0 k_{ij}\varphi_{,ji} + P_{i,i} = 0$ [319], where $E_i = -\varphi_{,i}$. Both the top and bottom surfaces of the PMN-38%PT pillar were shorted—that is, $\varphi = 0$ on the interface between pillar and substrate and $\varphi = \varphi^{appl}$ on the top free surface.

For the present two-dimensional simulations, a regular grid of $64\Delta \times 1\Delta \times 64\Delta$ voxels is adopted with periodic boundary conditions along all dimensions. The voxel size $\Delta = 1\,\mathrm{nm}$ is related to G_{110} by $\Delta = \sqrt{G_{110} \Big/ \left|\alpha_1^{\mathrm{PMN-33\%PT}}\right|_{T=27\,^\circ\mathrm{C}}}$. The gradient energy coefficient is chosen to be $G_{1111}/G_{110} = 0.6$ in reduced units. Here, the thermodynamic parameter of PMN-33%PT at room temperature—that is, $\alpha_1^{\mathrm{PMN-33\%PT}} = -3.46\times10^{7}\ \mathrm{C^{-2}m^{2}N}$—is chosen as the reference value for dimensionless, other ferroelectric properties in this study. The corresponding material constants for the stress-free Landau energy, the elastic constants and the elecrostrictive coefficients of PMN-38%PT are: $\alpha_1 = -4.51\times10^{7}\ \mathrm{C^{-2}m^{2}N}$, $\alpha_{11} = -5.28\times10^{8}\ \mathrm{C^{-4}m^{6}N}$, $\alpha_{12} = -1.04\times10^{9}\ \mathrm{C^{-4}m^{6}N}$, $\alpha_{111} = 5.62\times10^{9}\ \mathrm{C^{-6}m^{10}N}$, $\alpha_{112} = 1.80\times10^{10}\ \mathrm{C^{-6}m^{10}N}$, $\alpha_{123} = 3.44\times10^{10}\ \mathrm{C^{-6}m^{10}N}$, $c_{11} = 264\mathrm{GPa}$, $c_{12} = 187\mathrm{GPa}$, $c_{1111} = 43\mathrm{GPa}$, $Q_{11} = 0.062\mathrm{C^{-2}m^{4}}$, $Q_{12} = -0.025\mathrm{C^{-2}m^{4}}$, $Q_{44} = 0.027\mathrm{C^{-2}m^{4}}$. The thermodynamic study on PMN-PT will be published elsewhere. The time step is $\Delta t/t_0 = 0.03$, where $\Delta t_0 = 1\Big/\left(\left|\alpha_1^{\mathrm{PMN-33\%PT}}\right|_{T=27\,^\circ\mathrm{C}} L\right)$. We use the spontaneous polarisation constant $P_0 = 0.35\,\mathrm{C/m^{2}}$, the characteristic electric field $\phi_0 = P_0\sqrt{G_{110}\left|\alpha_1^{\mathrm{PMN-33\%PT}}\right|_{T=27\,^\circ\mathrm{C}}} = 0.012\,\mathrm{V}$ and the characteristic stress $\sigma_0 = \left|\alpha_1^{\mathrm{PMN-33\%PT}}\right|_{T=27\,^\circ\mathrm{C}} P_0^2 = 4.24\,\mathrm{MPa}$ to normalise the calculated results.

In the experimentally examined PMN-38%PT pillar, the pinned micro-domain walls restrict the elastic expansion or contraction of micro-domains along [100]. Thus, we assume a clamped x_1x_2 plane on a single micro-domain to computationally study the constraint effects on the ferroelastic domain transition process. For simulations on a domain with constraint, we have $\bar{\varepsilon}_{11} = 0$, $\bar{\varepsilon}_{33} = (1/V)\int_V \varepsilon_{33}^0 dV + s_{3333}\sigma_{33}^{appl}$ [293] and $\bar{\varepsilon}_{13} = 0$. Further, s_{ijkl} is the elastic compliance tensor and σ_{33}^{appl} is the applied stress. For simulations on a domain without constraint, $\bar{\varepsilon}_{11} = (1/V)\int_V \varepsilon_{11}^0 dV + s_{1133}\sigma_{33}^{appl}$, $\bar{\varepsilon}_{33} = (1/V)\int_V \varepsilon_{33}^0 dV + s_{3333}\sigma_{33}^{appl}$ and $\bar{\varepsilon}_{13} = 0$. The

ferroelastic energy barrier is probed by applying a variety of compressive stress to an initial P_3^+ domain and then calculating the ferroelastic energy of the stable domain structures.

5.2.6.2. Phase-field experiments

Figure 5-7 presents the results of the phase-field calculations and simulations for the domain transition kinetics of a PMN-38%PT single crystal under different loading conditions. To demonstrate the pinning effect of micro-domain walls on domain transition kinetics, we first calculated the ferroelastic energy of the tetragonal domains with and without constraint. Figure 5-7 (a) shows that, while the ferroelastic energy for a c-domain remains the same, the ferroelastic energy barrier for rotating a single c-domain to an a-domain with constraint is one order of magnitude larger than that without constraint (the energy barrier is presented by the peak energy between the two local energy minima). Therefore, the elastic energy can be easily relaxed when the micro-domain is not constrained by neighbouring domain walls. In contrast, domain transition in a micro P_3^+ domain, wherein elastic expansion or contraction along [100] is constrained by the pinned P_3^+ / P_1^- micro-domain walls, occurs via the formation of intermediate ferroelastic domains. The large elastic energy barrier for the constraint situation not only leads to the formation of an intermediate ferroelastic 90^o domain structure, it also presents an approach for reversible ferroelastic switching after external mechanical stress is removed.

When only an electrical loading is applied to a single P_3^+ domain, ferroelectric 180^o domain switching (P_3^+ to P_3^-) occurs (see Figure 5-7 (b)), which requires little change in elastic energy. When only mechanical stress is applied, multiple ferroelastic 90^o P_1 domains are produced in the pillar as shown in Figure 5-7 (c). If the compression is removed, most P_1 domains rotate back to the original tetragonal P_3^+ domain, demonstrating the reversible

ferroelastic domain transition, which is consistent with the experiment observations shown in Figure 5-4 and the calculated ferroelastic energy barrier presented in Figure 5-7 (a).

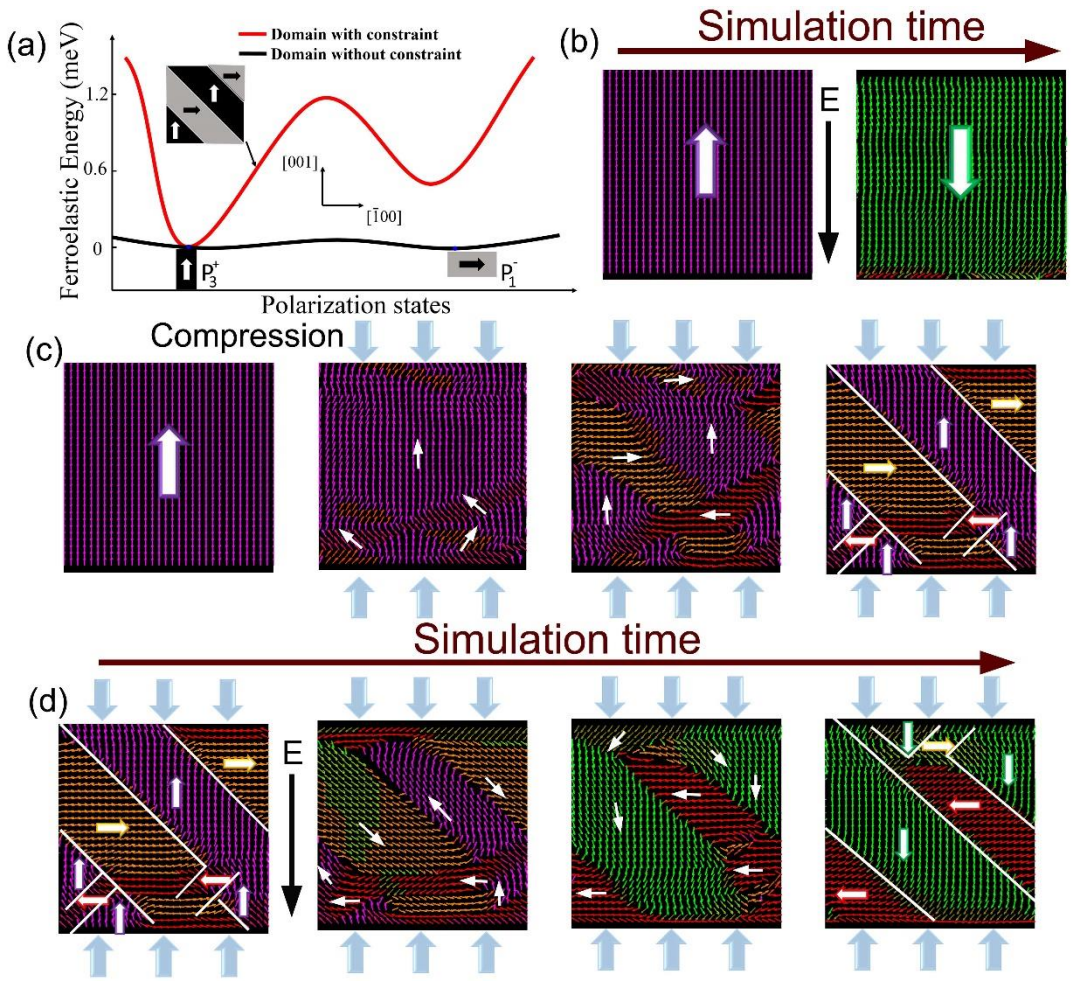

Figure 5-7 Phase-field simulation and calculation on kinetic domain transformation in PMN-38%PT single crystal. **(a)** Predicted ferroelastic energy of tetragonal domains in a PMN-38%PT single crystal. The two local minimum points in the wavy red curve represent the ferroelastic energy for a constrained c-domain and an a-domain respectively. The local maximum in the middle of the red curve represents the energy required (the energy barrier) for rotating a single c-domain to an a-domain. **(b, c, d)** Domain transition under electrical loading alone, mechanical loading alone and combined mechanical and electrical loading respectively. Instead of 180° ferroelectric switching, as shown in **(b),** continuous 90° ferroelastic domain transition is observed when mechanical loading is applied in **(c).**

The above simulation results explain very clearly the formation of the 90^o tetragonal nanodomains depicted in Figure 5-4. During the mechanical loading, the motion of the micro-

domain walls is limited by the pinning effects, leading to constraint on the micro P_3^+ domains. The resulting significant elastic energy is usually released instantly through the formation of multiple nano-sized P_1 domains.

Figure 5-7 (d) presents the effect of the formation of ferroelastic nanodomains on ferroelectric switching under combined mechanical and electrical loading by phase-field simulations. The initial state was the stable domain structure under mechanical loading that is shown in Figure 5-7 (c). Keeping the same mechanical loading, electrical loading was applied along the P_3^- direction, resulting in a fundamentally different domain switching evolution. Instead of rotating towards the poling direction, tetragonal domains rotate 90° only—that is, $P_3^+ \rightarrow P_1^-$, $P_1^+ \rightarrow P_3^-$ and $P_1^- \rightarrow P_3^-$. Under combined mechanical and electrical loadings, the ferroelectric switching proceeds via a ferroelastic domain transition and all domain walls retain a neutral charge that minimises the electrostatic fields.

5.2.7. Domain switching kinetics under combined mechanical and electrical loadings

Ninety degree domain switching with the assistance of high-density 90° nano-tetragonal domains is revealed by phase-field simulations for combined electrical and mechanical loading. An in-situ TEM study on the domain switching process under combined mechanical and electrical loading was also conducted to confirm the phase-field prediction. A combined loading was applied to the same pillar, represented in Figure 5-2.

A negative bias of –4 V was first applied to completely recover the initial domain structures shown in Figures 5-2 (a) and 5-8 (a). Then, a mechanical loading of 190 MPa along the [001] direction was applied, forming two new types of 90° nanodomain walls, as shown in Figure 5-8 (b). The mechanical stress was maintained during the subsequent electrical loading process. The domain structures for each distinct domain sub-band type shown in Figures 5-8 (a)–5-8 (d) are presented schematically in Figures 5-8 (e)–5-8 (l).

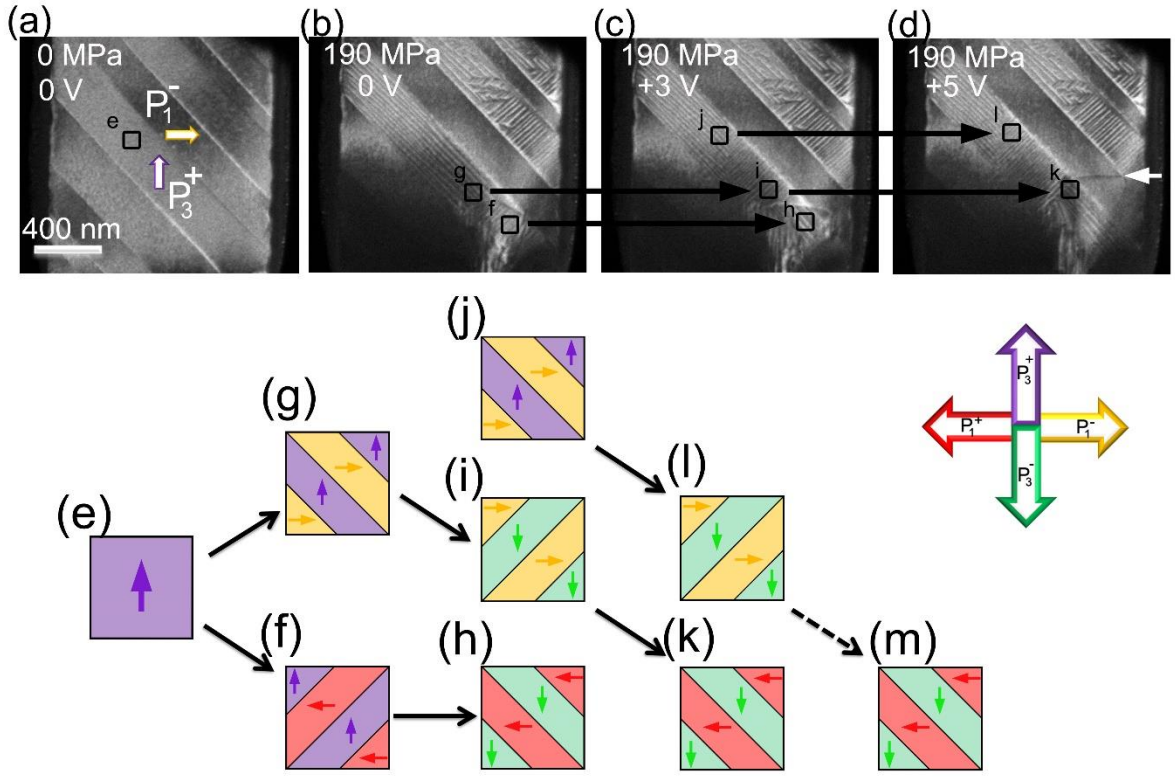

Figure 5-8 (a–d) A series of experimental images showing the evolution of ferroelastic domains under electrical loading with mechanical loading. The 180° ferroelectric domain wall $\boldsymbol{P_1^+/P_1^-}$ is indicated by the white arrow in **(d)**. **(e–m)** Illustrations of the switching process in an originally micro $\boldsymbol{P_3^+}$ domain, for the initial state **(e)**, mechanical loading only **(f, g)**, low electrical bias with mechanical loading **(h–j)**, high electrical bias with mechanical loading **(k, l)** and predicted higher electric bias with mechanical loading **(m)**.

At the initial state (Figure 5-8 (a)), the domain sub-band in area (e) is up-poled (P_3^+). With the mechanical stress, parts of P_3^+ rotate to P_1^+ (with P_3^+/P_1^+ domain walls in (f)) and P_1^- (with P_3^+/P_1^- domain walls in (g)). By applying a +3 V electrical bias, while keeping the same mechanical loading (see Figure 5-8 (c)), a 90° reorientation of domain boundaries occurred in both the (h) and (i) domain sub-bands, while the domain boundaries in (j) did not change. The 90° domain-wall rotations from (f) and (g) to (h) and (i) respectively, are intermediate states that facilitate the whole 180° domain-wall rotation by electric loading under mechanical loading. Without mechanical loading, such 90° domain-wall rotation would occur only when the electrical poling ran along the [111] direction[198].

Such interesting continuous rotation of 90° nano-tetragonal domain structures under combined electrical and mechanical excitations is closely related to ferroelastic transition. Without mechanical loading, 180° domain reversal takes place with the formation of neutrally charged 180° domain walls. Surprisingly, it is found that (f) rotates 90° to (h) when an electrical bias is applied, as shown in Figure 5-8 (c). Similarly, (g) rotates 90° to (i) (see Figure 5-8 (c)), followed by another 90° domain-wall rotation to (k) with an increase of the bias (see Figure 5-8 (d)). According to the phase-field simulations depicted in Figure 5-6 (d), the (g) state rotating to the (k) state via orthorhombic domains is an energetically favourable path when only neutrally charged domain walls exist. However, accompanying the existence of the pinned neighbouring P_1^- domain, the P_3^+/P_1^- (g) nanodomain walls energetically prefers rotating 90° (to (i)) towards P_1^- before reaching the energetically favourable state (k). Once the state (k) has been stabilised, the significantly charged domain wall between (k) and the original micro P_1^- domain will rotate the neighbouring P_1^- domains to P_1^+. The transition from (f) to (h) is also attributed to the same catalyst, whereby the neighbour switched P_1^+ domain stabilises the (h) state, making it difficult to rotate again. This is confirmed by the switching process depicted in Figure 5-8, where the neighbouring 180° P_1^-/P_1^+ domain wall, indicated by the white arrow in Figure 5-8 (d), keeps pace with the production of a stable P_3^-/P_1^+ domain structure—shown in (h) and (k). Such a stable 90° nanodomain structure (P_3^-/P_1^+) is consistent with our phase-field simulation results. Further increasing the electric field would ultimately lead to the switching of (l) to (m).

5.2.7.1. The continuous rotation of 90° nano-tetragonal domain structures during electrical poling with mechanical loading

The formation of high-density 90° nanodomain walls triggers complex 90° domain switching when electrical bias is applied. Figure 5-9 illustrates the detailed domain switching processes introduced by Xu et al.[198]—moving from (g) to (k) via (i) and from (f) to (h) in Figure

5-8. Figure 5-9 (a) represents P_3^+/P_1^- (see Figure 5-8 (g)) domains. To clearly demonstrate the transition process, the whole P_3^+/P_1^- area is divided into four parts labelled from one to four. In Part 1, the P_3^+ domain rotates 180° to P_3^-(as in Part 1 of Figure 5-9 (b)). At the same time, Parts 2 and 4 rotate 90° from P_3^+ to P_1^- and from P_1^- to P_3^- respectively, while Part 3 remains unchanged.

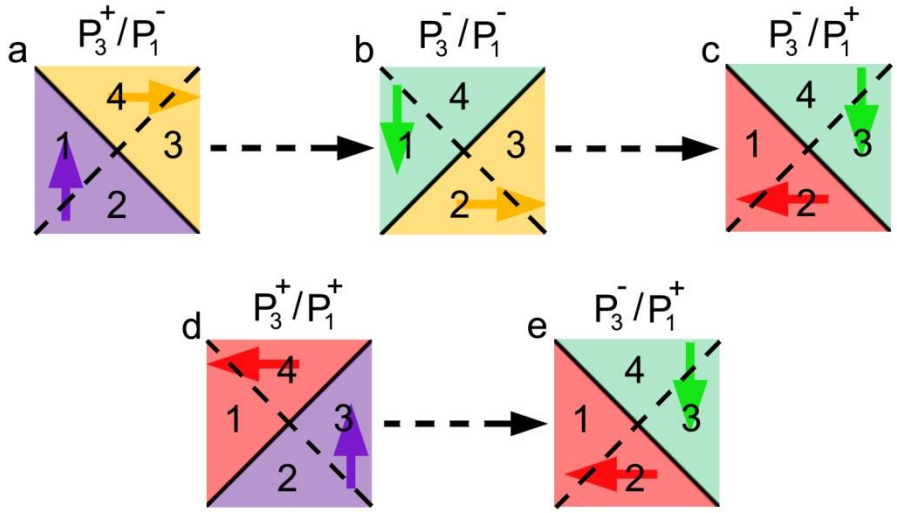

Figure 5-9 Schematic of the continuous switching processes of 90° nano-tetragonal domain structures under combined external excitation—a switching path from $\boldsymbol{P_3^+/P_1^-}$ to $\boldsymbol{P_3^-/P_1^+}$ **(a–c)** and a switching path from $\boldsymbol{P_3^+/P_1^+}$ to $\boldsymbol{P_3^-/P_1^+}$ **(d–e).** The solid black lines represent the domain walls, while the dashed black lines are used to separate sections.

Similar to the processes shown in Figures 5-9 (a)–5-9 (b), the rotation from P_3^-/P_1^- (see Figure 5-9 (b)) to P_3^-/P_1^+ (see Figure 5-9 (c)) also includes four parts: two 90° rotations from P_3^- to P_1^+ and from P_1^- to P_3^- in Parts 1 and 3 respectively, one 180° rotation from P_1^- to P_1^+ in Part 2 and the non-switched Part 4. Combining with the above two switching processes, the electrical loading under mechanical confinement rotates P_3^+/P_1^- (see Figure 5-9 (a)) 180° to P_3^-/P_1^+ (see Figure 5-9 (c)) via an intermediate domain, in which the tetragonal 90° domain wall rotates 90° (see Figure 5-9 (b)). In contrast, the 180° rotation of a single micro P_3^+ domain occurs under electrical loading only (as seen in Figure 5-2).

The rotation from P_3^+/P_1^+ to P_3^-/P_1^+ works in the same way as shown in Figures 5-9 (d) and 5-9 (e). By keeping Part 1 the same, Parts 2 and 4 perform 90° rotation from P_3^+ to P_1^+ and from P_1^+ to P_3^- respectively. The P_3^+ in Part 3 (see Figure 5-9 (d)) rotates 180° to P_3^- (see Figure 5-9 (e)). However, when the electric field is increased after this point, no more domain switching takes place in this area as a result of the neighbouring micro P_1^+ domain that restricts any further switching processes.

5.2.8. Mechanical loading facilitating ferroelectric switching

Since ferroelastic switching requires less external energy than ferroelectric switching[312, 320] and the much smaller intrinsic nucleation barrier at the 90° domain walls than at 180° domain walls, the 90° ferroelastic domain switching is easier than the 180° ferroelectric domain switching. Therefore, electronic devices that realise ferroelectric switching via controllable ferroelastic transitions are more energy efficient. The length of switched domains is an important parameter for examining ferroelectric properties, including coercive fields, remnant polarisation and electromechanical coupling factors[321].

Figure 5-10 shows how the switched domain length was measured from TEM images. In this figure, the green-dashed lines represent the 180° domain walls that are formed by applying electrical bias. For the P_3^- domain, the initial point of the domain wall starts from the micro-domain wall, indicated by a white vector in the lower-right corner. The length of the P_3^- domain is measured from this point to the 180° domain wall, tracing along the pointed micro-domain wall as indicated by the blue, double-headed arrow. Similarly, for the P_1^+ domain, the domain wall is also initiated from this point. The length of the P_1^+ domain is thus measured from this point to the horizontal 180° domain wall, as indicated by the red, double-headed arrow.

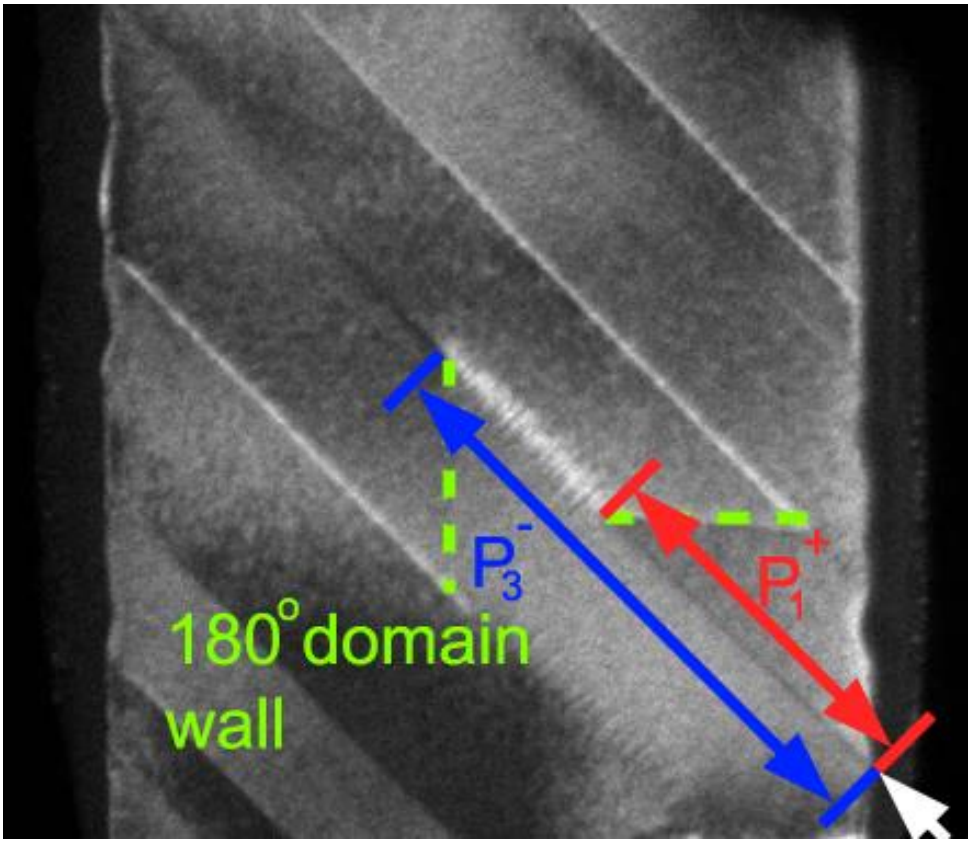

Figure 5-10 Switched domain length measurements: the green-dashed lines represent the vertical and horizontal 180° domain wall, while the blue and red vectors represent the measurements of the $\boldsymbol{P_3^-}$ and $\boldsymbol{P_1^+}$ domain lengths respectively. The white vector points to the end of the micro-domain wall, which serves as the starting point for measurement.

Figure 5-11 shows the lengths of the switched domains as a function of electric bias. The maximum switched P_3^- domain length for combined electrical and mechanical loadings was significantly larger than those without mechanical loadings. The domain switching was initiated at a bias of +2 V and +3.2 V in situations with and without mechanical loading respectively. The former was surprisingly ~ 40% lower than the latter. Nevertheless, the switched P_1^+ domain lengths (see the inset graph) were almost identical for both cases, because there was no switching assistance from the 90° nanodomains for the micro P_1^- domains.

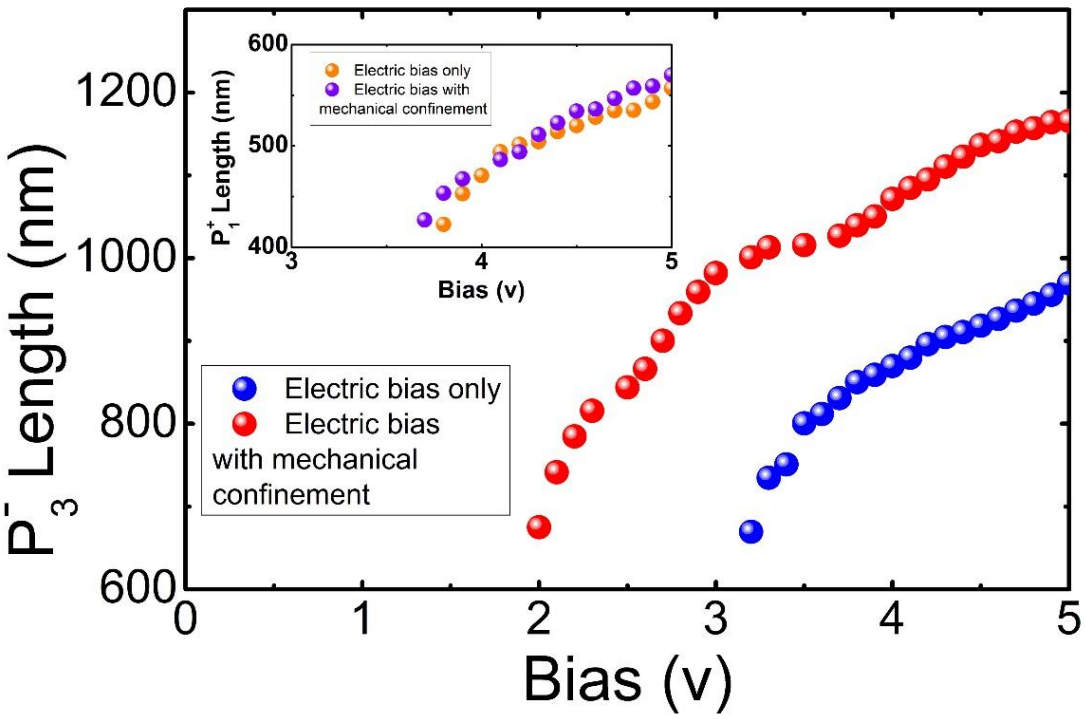

Figure 5-11 Switched domain length verses bias—a graph comparing the domain switching capabilities of electrical loading with and without mechanical loading in micro $\boldsymbol{P_3^+}$ domains and micro $\boldsymbol{P_1^-}$ domains (see the inset graph).

5.3. Summary

In summary, our in-situ electron microscopy experiments and phase-field simulations revealed the domain switching processes of ferroelectric PMN-38%PT single crystals under different external loading conditions. Hierarchical ferroelastic domain transitions were observed when significant mechanical stress was applied. Phase-field simulations confirmed experiment observations that the 90° ferroelastic transition takes place under electrical poling with mechanical loading, while 180° micro-tetragonal domain reversal occurs under electrical loading without mechanical loading. The formation of 90° nanodomains assists ferroelectric domain switching and reduces the threshold field for domain switching by 40%, indicating the unique role that mechanical loading plays during electrical poling. This study provides new

insights into achieving controllable ferroelastic transitions to facilitate ferroelectric switching in bulk ferroelectric materials.

Chapter 6

Stress-induced ‘elastic’ and ‘plastic’ ferroelectric domain switching

6.1. Introduction

Ferroelectric materials have attracted much attention for their potential use in actuators, sensors and non-volatile memories[54, 64, 77, 116, 306]. In these applications, ferroelectric materials are often subjected to various levels of mechanical loading[187, 209, 210, 288, 310], either intentionally through the design of the devices or unintentionally, as caused by environmental stresses. Mechanical loadings, including uniaxial compression[185, 189, 210] and tension[211, 322], have been reported to significantly affect spontaneous polarisation, remnant polarisation, coercive fields and the hysteresis behaviour of ferroelectric materials. Several studies[209, 210, 322] have found that, with applied stress changing from compression to tension, remnant polarisation increases and the coercive field decreases, while other studies have shown the opposite[211]. A comprehensive understanding of the dynamical microscopic structural behaviour of ferroelectric domains under stress is critical for revealing the mechanisms behind these contradictory results. However, this is not an easy task because of the difficulty of extracting structural details from conventional mechanical compression and tension experiments. A number of studies[183, 210] have been conducted to investigate microscopic domain switching kinetics under compression. I have demonstrated in Chapter 5 that a compression stress of ~ 180 MPa assists the nucleation of 90° nanodomains and decreases the coercive fields of materials. Using piezoresponse force

microscopy, Kwanlae et al.[183] reported that domain evolution processes under mechanical compression with a stress of ~ 70 MPa include the nucleation of new lamellation and the overwriting of differently oriented lamellation. These results visualised how domain switching responds to low-level mechanical compression. However, it is not clear how domain switching responds to middle-to-high levels of stress.

The coercive field[30, 301] is a measure of the ability to resist depolarisation. Macroscopic investigations on the hysteresis of ferroelectric materials have suggested that polarisation will not be eliminated permanently before the applied external field reaches the coercive field and that polarisation will be redirected permanently when the applied field exceeds the coercive field[42, 46, 279]. However, this oft-studied behaviour lacks corresponding microscopic descriptions as to how a domain reacts to the different levels of applied fields, impeding the possibility of improving the hysteresis behaviour of ferroelectric materials via domain manipulation engineering.

Here, I used an in-situ TEM to explore ferroelastic domain switching kinetics when subjected to low-to-high levels (before and after exceeding the coercive field) of mechanical compression and tension in PMN-38%PT single crystals with tetragonal domains[128]. It was found that, depending on the stress levels, the domain evolution processes exhibit an elastic-like reversible behaviour under low levels of mechanical stress and a plastic-like irreversible behaviour under high levels of mechanical stress. The elastic-like behaviour involves the nucleation and merging of 90° ferroelastic nanodomains, while the plastic-like behaviour, surprisingly, exhibits 180° domain switching associated with the formation of a large, new single domain. These results provide significant new insights into polarisation switching kinetics and expand the fundamental comprehension of domain behaviour. Further, real-time observation of domain switching behaviour during a complete deformation process assists in comprehensively understanding macroscopic hysteresis behaviour.

6.2. Experimental results and discussion

Figure 6-1 (a) presents a typical dark-field TEM image of a PMN-38%PT single-crystal pillar with dimensions of 2.0 μm × 1.5 μm × 0.08 μm (length × width × thickness) for the following in-situ compression and tension tests. The experimental setup and sample preparation have been detailed in Chapter 2. The indentation probe was covered with a layer of sticky matter to allow mechanical compression and tension experiments to be carried out on a sample pillar. Lamellar-like domains with different polarisation were found in the pillar. Three domains with 45° inclinations are marked by black-dashed lines and labelled with ①, ②, and ③ for the convenience of the following discussion. The STEM-HAADF technique[184, 275] was applied in the green box area to image the polarisation directions and the domain-wall structures. Through the measurement of the displacement between Pb cations and their surrounding Mg/Nb/Ti cations in the HAADF image[184, 190], four distinct domains were located in the green box area, as shown in the enlarged STEM-HAADF image: the a^- domain (the red vector) and the a^+ domain (the yellow vector) are separated by a horizontal 180° domain wall, while the c^- domain (the green vector) and the c^+ domain (the purple vector) are separated by a tilted 180° domain wall. The domain labelling codes follow those used in Chapter 5. A 45° tilted domain wall separates the *a* and *c*-domains to ensure a non-charged head-to-tail domain structure. The four distinct domains (a^-, a^+, c^-, and c^+ domains) meet at a quad point. The domain configuration of the area with black-dashed lines has been schematically drawn at the bottom of Figure 6-1 (a).

A low-level mechanical compression stress (~100 MPa) was applied to the pillar as shown in Figure 6-1 (b). Multiple 90° a^- nanodomains nucleated in the original c^+ domain area, forming nanostripes along the domain zone ②. This is consistent with the results presented in Chapter 5, where $c^\pm$ domains are easily rotated into $a^\pm$ domains under mechanical compression

along the *c* direction. Retracting the indentation probe changes the nature of the stress applied to the pillar from compression to tension, as shown in Figure 6-1 (c). Under tension stress, the domain evolution was different from when it was under compression: 90° nanostripes nucleated in the original $a^{\pm}$ domain zones ① and ③, while the domains in zone ② remained unchanged. Analysis of the newly formed 90° nanostripes shows that the rotation of $a^{\pm}$ domains to $c^{\pm}$ domains was triggered by the application of mechanical tension along the *c* direction. This result indicates that compression and tension along the same direction result in opposite effects: compression stress rotated the polarisation to the normal of the loading direction, while tension stress rotated the polarisation towards the loading direction.

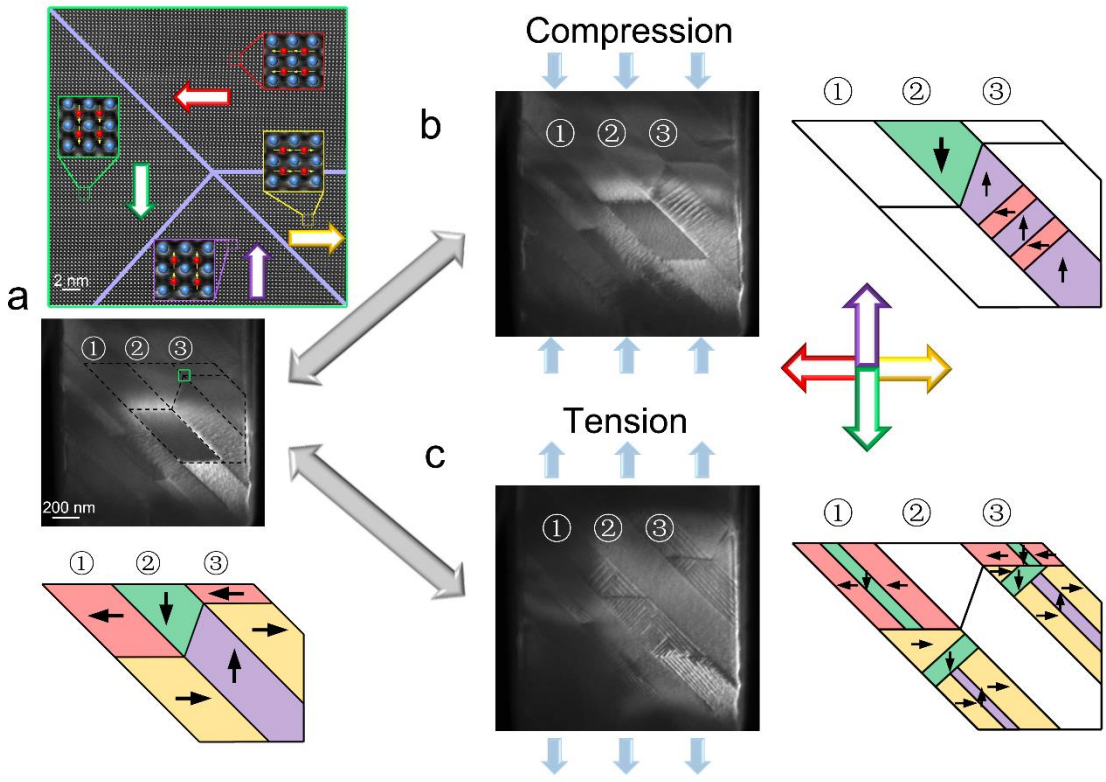

Figure 6-1 An in-situ compression and tension experiment on the same pillar. **(a)** The domain morphology without mechanical loading. On the bottom of the image is the schematic drawing of the three bands of domain areas labelled ①, ② and ③. The area marked by a green frame is enlarged. The corresponding STEM-HAADF image shows four distinct polarisations that meet at a quad point. **(b)** and **(c)** represent the domain morphologies under compressional and tensile stress respectively.

Although it is now clear that both compression and tension stresses promote the nucleation of 90° nanodomains, the domain evolution process under high levels of stress remains unknown. To explore the whole domain evolution process under increasing stress, a compression experiment is not suitable, as the pillar can be easily bent when subjected to high levels of compression stress. A series of TEM images in Figures 6-2 (a)–6-2 (d) and its corresponding stress–time plot in Figure 6-2 (e) present an example of the compression deformation process of a thin pillar. A platform in the stress–time curve was formed when the stress reached ~ 120MPa, which indicated the bending of the sample. This bending was confirmed by the bending contrast shown in Figure 6-2 (c). Therefore, tensile stressing is necessary for experiments with high levels of stress.

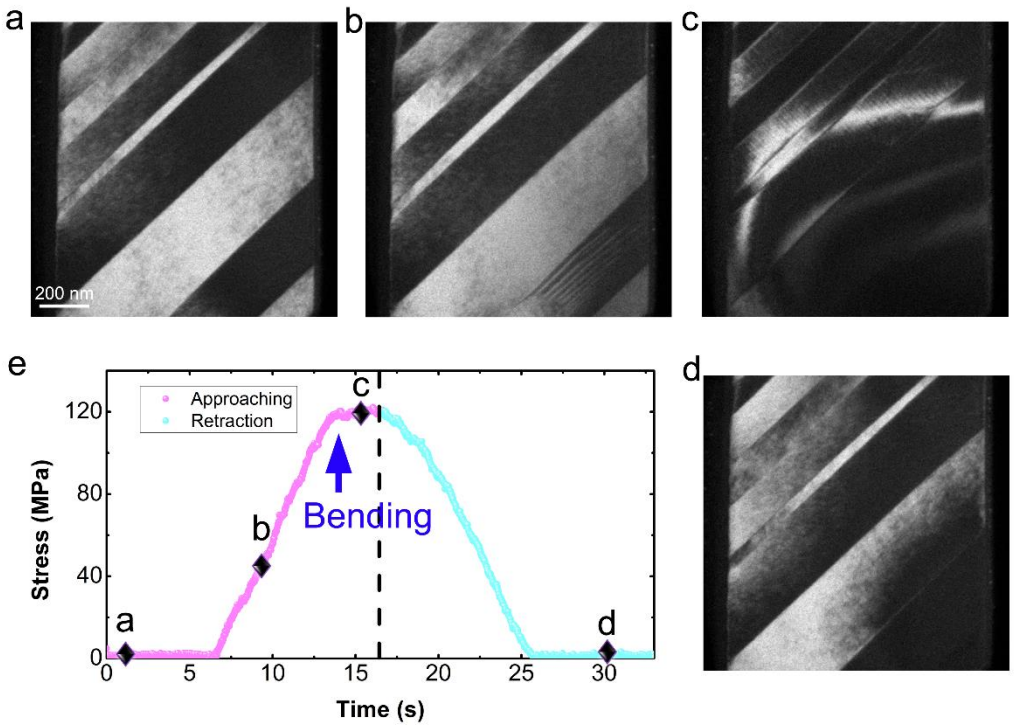

Figure 6-2 (a–d) A series of images showing the deformation of a pillar under compressional stress. The bending contour shown in **(c)** represents the bending of the pillar. **(e)** A load–time curve showing the real-time application of mechanical compressional loading. The horizontal line between 13 and 16 seconds shows the moment of bending.

Figure 6-3 shows a tensile experiment for real-time domain switching kinetics using a PTP device mentioned in Chapter 2. Figure 6-3 (a) shows the real-time measured stress–time curve, while points b–i correspond to the loading moment in Figures 6-3 (b)–6-3 (i). The linear stress–time plot confirmed that the mechanical deformation process was pure elastic for deformations under the maximum stress of 300 MPa. Consistent with the domain configuration shown in Figure 3-1, alternately aligned head-to-tail a^+ domain and c^- domain configurations are presented before stressing, as shown in Figure 6-3 (b). With increasing tensile stress, multiple 90° nanodomains formed in bulk a^+ domain areas, as shown in Figure 6-3 (c), which is consistent with those presented in Chapter 5 as well as the phenomena observed in Figure 6-1. When the stress was increased, more 90° nanodomains formed from the original a^+ domains. Figure 6-3 (d) shows an area (along with the corresponding enlarged area included in the green box) with a high density of nanodomains under stress levels reaching 105MPa. Further increasing the tensile stress led to the merging of the initiated 90° nanodomains until a new, large domain formed, as shown in Figures 6-3 (e)–6-3 (f). Full retraction of the stress removed all stress-induced nanodomains and the domains returned fully to their original configurations as shown in Figure 6-3 (i).

It has been reported that domain walls are pinned by defects such as oxygen vacancy or compositional variation in relaxor-based ferroelectrics[176, 210, 312]. The pinning effect that constrains micro-domains produces a large, elastic energy barrier. Energy applied by external stress overcomes the energy needed to initiate new domains, leading to the formation of nanodomains. However, the energy stored in the new nanodomain and domain walls was not large enough to overcome the large, elastic energy barrier. Therefore, reversed ferroelastic switching occurred after the external stress was removed, as shown in Figure 6-3 (i).

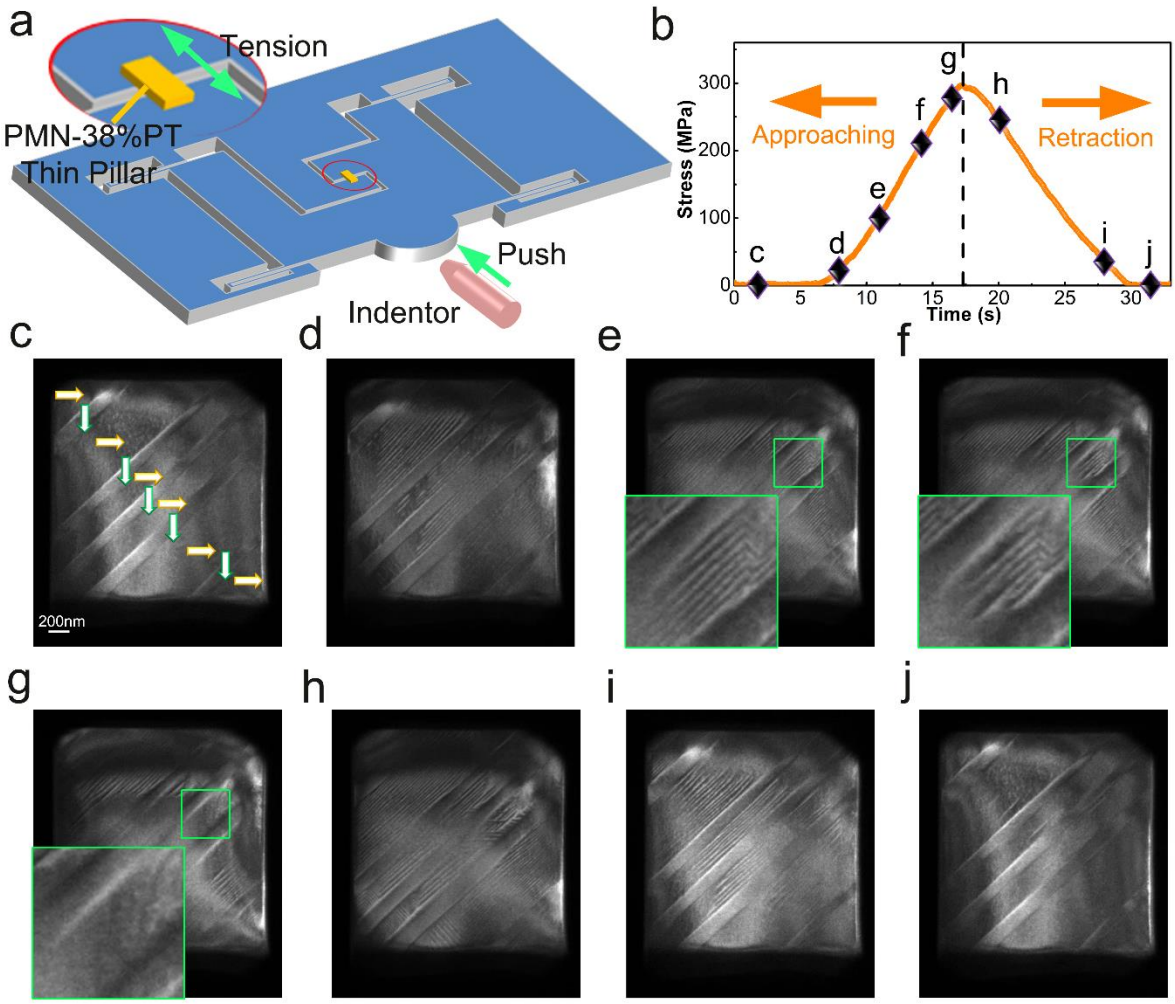

Figure 6-3 (a) A load–time curve showing the real-time application of mechanical tensile loading. The linear plot represents a pure elastic deformation during the deformation process. Points b–i correspond to the stress applied to the sample at **(b–i). (b–i)** A series of TEM images showing domain evolution under low levels of tensile stress.

Figure 6-4 shows a series of in-situ TEM images, demonstrating the domain evolution of the same pillar subjected to higher levels of tensile stress up to 1340MPa. It can be seen from Figure 6-4 (b) that the stress–time plot was linear. Because the deformation was in the displacement-controlled mode, the linear plot indicates that the mechanical deformation was pure elastic. The blue-dashed line in Figure 6-4 (f) is an imaginary datum line. The mechanical test was conducted under the displacement-controlled mode. The significant loading carried by the PTP device contributed to further bending during the stress releasing stage, leading to a delay of the retraction of the indentor. This introduced an uneven gradient in the stress slope

during the loading and unloading stages. However, this phenomenon did not affect my conclusion. Figures 6-4 (a)–6-4 (e) show the domain structures at the deformation stages, marked with a–e in Figure 6-4 (f). Note that, while Figures 6-4 (a)–6-4 (d) correspond to the loading stage, Figure 6-4 (e) shows the domain structure after unloading. Before loading, there was an alternately aligned a^+ and c^- domain configuration, as shown in Figure 6-4 (a). Two areas marked by numbers 1 and 2 in Figure 6-4 (a) are enlarged with purple and green frames respectively. At the stress level of ~ 350 MPa, some stress-induced nanodomains merged, forming micro-domains, while parts of them were in the process of merging, as depicted in Figure 6-4 (c). An area of high-density nanodomains is framed by a blue rectangle, marked with a number '3' and enlarged. Further increasing the stress led to the merging of all nanodomains into micro-domains and no further obvious domain switching was found after the merging process, as indicated in Figure 6-4 (d). After releasing the stress, the merged micro-domains disappeared, while large amounts of nanodomains appeared, as shown in Figure 6-4 (e). This indicated an irreversible domain switching process after the applied stress had reached a certain level.

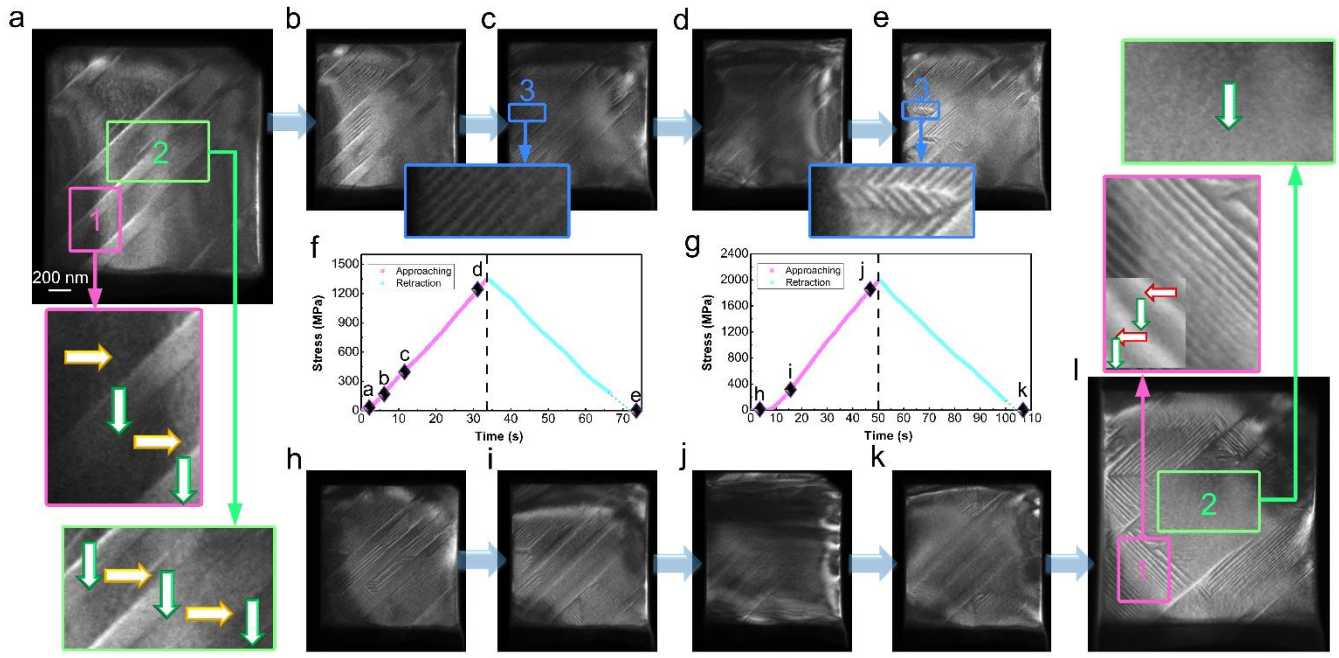

Figure 6-4 (a–e) A series of TEM images showing domain evolution under medium levels of tensile stress. The corresponding stress–time plot is shown in **(f)**. Labels **(a–e)** in **(f)** represent the stress applied at the moments shown in **(a–e)**. **(h-l)** TEM images showing in-situ deformation of the same pillar as in **(a-e)** under high levels of tensile stress. The corresponding stress–time plot is shown in **(g).** Labels h–k in **(g)** represent the stress applied at the moments shown in **(h–k)**. **(l)** shows the domain morphology 20 minutes after domain relaxation in **(k)**.

The domain orientation evolution in area three during the loading–unloading process occurred in an unexpected way. In the loading state, as shown in Figure 6-4 (c), nanoscale c^- domains formed within an original a^+ domain region, forming a $a^+/c^-/a^+/c^-$ domain structure. When the stress was increased to around 1250 MPa, all of the nanodomains emerged and aligned into micro c^-domains, as shown in Figure 6-4 (d). Interestingly, after unloading, parts of the c^- domains turned into a^+ domains, while other parts became a^- domains, resulting in combined a^+/c^- domains and a^-/c^- domain configurations, as shown in area three of Figure 6-4 (e). The behaviour of the partial reversion of domains is similar to the elastic–plastic deformation behaviour of metallic materials. When the applied load was larger than a threshold value, only part of the switched structure was reversed upon the release of the stress. In this case, when the applied tensile stress was sufficiently large, all *a*-domains switched to *c*-domains. However, once the tensile stress was released, the switched domains did not remain

stable enough and the large micro c^- domains did not maintain their high-energy, single domain states. The micro *c*-domains tended to transform into nanoscale domains[190, 278] and parts of the *c*-domains were backswitched. The backswitched domains could be either a^+ or a^-domains—each of which utilise equivalent energy[210]. This resulted in the 180° *a* domain switching that was observed following a loading cycle.

Although 180° domain switching does not contribute to the ferroelastic component, it increases the remaining polarisation significantly after a mechanical loading cycle. The increasing of remnant polarisation makes the use of such ferroelectric materials beneficial for non-volatile memory and other piezoelectric devices[323]. This 180° domain switching after a mechanical loading cycle has not been realised before and it significantly affects the performance of ferroelectric materials.

The second tensile loading–unloading cycle with a maximum stress of ~ 2000 MPa was applied to the same pillar, as shown in Figures 6-4 (g)–6-4 (l). The linear stress–time plot in Figure 6-4 (g) suggests that the specimen only experienced elastic deformation. Figures 6-4 (h)–6-4 (j) and 6-4 (k)–6-4 (l) show the domain evolution processes during loading and unloading respectively. The domain evolutions in Figures 6-4 (h)–6-4 (j) are similar to those shown in Figures 6-4 (b)–4 (d). A complicated domain morphology with remnant stress formed immediately after the large tensile stress was released, as indicated in Figure 6-4 (k). After 20 minutes, the remnant stress had been fully released, leaving behind a completely different domain morphology to Figure 6-4 (k) (see Figure 6-4 (l)). Compared with the initial polarisation in Figure 6-4 (a), Figure 6-4 (l) shows 180° domain switching in area one of the pink box, which is similar to the case that discussed above for area three. Interestingly, the previous bulk a^+/c^- domains were transformed into a single c^- domain in area two.

Chapter 5 discussed how the pinning on micro a^+/c^- domain boundaries was sufficiently large that the boundaries did not move under electrical stimulation. However, the formation of a single *c*-domain in area two indicates that a significant mechanical stress is able to overcome the defect-induced pinning effect and turn *a*-domains into *c*-domains permanently. During the deformation, sufficiently large stress overwhelmed the pinning effect on domain boundaries, resulting in the decreasing of the energy barriers. The disappearance of the constraint on the domain stabilised the switched c^- domains, leading to irreversible domain switching after the release of the loading.

Although the specimen experienced only elastic deformation, the domain switching processes under different levels of mechanical stress underwent reversible ('elastic') and irreversible ('plastic') evolution. At low stress levels, domains underwent elastic deformation and were fully reversed after the retraction of stress as a consequence of the existence of large nucleation energy barriers caused by the pinning effect. At medium stress levels, domains behaved in a plastic manner, with elements of the switched domains gaining sufficient energy to proceed to a stable state. After the retraction of stress, domains in an unstable state were backswitched, leading to the partial reversal of switched domains and the formation of 180° *a*-domains in the specimen. At high stress levels, large external energy broke the pinning of the micro-domain boundaries, decreasing the constraint on the domains. In these cases, the energy barrier was significantly lower and formed a single domain without backswitching after the removal of stress.

The above results demonstrate the capability of inducing permanent domain switching by elastic mechanical loading. This indicates that mechanical loading can have the same effect as electrical loading in driving ferroelectric domain switching. Caution is needed to avoid significant the mechanical deformation of ferroelectric devices during the operation as sufficiently large mechanical loading can permanently change domain configurations.

6.3. Summary

In summary, a systematic investigation of domain switching under significant mechanical loading revealed the capacity for the manipulation of temporal/permanent 90° ferroelastic domains and 180° ferroelectric domain switching. Domain switching behaviour can be either elastic at low stress levels or plastic at high stress levels when the specimen is subjected to elastic deformation. This study provides new insights into mechanical kinetics for ferroelastic domains and into the origin of the hysteresis of ferroelectric materials under mechanical loading.

Chapter 7

Conclusions and future perspectives

7.1. Conclusions

The responses of ferroelectric materials to several types of external stimuli and the corresponding domain switching kinetics have been investigated using in-situ TEM techniques combined with phase-field modelling. The following conclusions are drawn, which can assist in understanding the origins of ferroelectric properties and improving the performance of ferroelectric materials:

1. A high-energy e-beam is an efficient tool for manipulating erasable and stable ferroelectric domain patterns with high spatial resolutions in thin-film ferroelectric materials. The e-beam introduces positive charges through its interaction with the thin-film materials in the illuminated area. These positive charges then generate a high omnidirectional electric field that redirects the polarisation around the illuminated area.
2. The size of the redirected polarisation area is determined by the size of the e-beam, the e-beam energy, the sample volume and the electron-beam illumination time. An analytical expression has been deduced to quantitatively describe this relationship and to guide the manipulation of ferroelectric domains. Ferroelectric domain manipulation using an e-beam requires no pre-poling, no electrode and no physical contact between the material and a tip—a process that is ideal for manufacturing miniature and integrated electronic devices. Moreover, this technique potentially

allows for nanoscale domain manipulation, which can significantly improve the data-storage capacity of current memory devices.

3. Domain switching kinetics under mechanical and electrical stimulations for relaxor-based ferroelectric materials in the vicinity of MPB is different from that for normal ferroelectric materials because of the low and asymmetric energy barriers among the different domains in relaxor-based ferroelectrics. Domain switching behaviours are determined by the type of the previous stimulation. After a mechanical loading–unloading cycle, domain structures transform to a mechanically reversible state—that is, the domains are fully reversible under a mechanical loading–unloading cycle. After an electrical loading–unloading cycle, domain structures are in a mechanically irreversible state—that is, the domains are irreversible under a mechanical loading–unloading cycle. Domain switching behaviour can also be represented by using an electrically irreversible or electrically reversible state, in which a mechanically reversible state is equal to an electrically irreversible state and a mechanically irreversible state is equal to an electrically reversible state.
4. Mechanically reversible and mechanically irreversible states can be used to represent the logical signals zero and one for non-volatile memories. This can effectively avoid the domain backswitching effect and therefore significantly enhance the reliability of non-volatile memories.
5. The domains in ferroelectric materials with compositions outside the MPB (composition > 35%PT) for PMN-PT relaxor-based ferroelectrics are tetragonal shaped. The domain energy barrier formations for these materials are significantly higher than those for compositions within MPB. Moreover, when a composition is over the MPB (~38%PT), the domain walls are significantly pinned by defects, including compositional variations that provide even higher energy barriers for the

domains compared to the relaxor-based material within the MPB. Therefore, mechanical stimulation results in the formation of 90° nanodomains within these materials and electrical stimulation induces 180° domain reversal without moving the micro-domain wall.

6. The formation of 90° nanodomains induced by mechanical stress assists 180° ferroelectric domain switching. Because 90° switching requires less energy than 180° switching, electrical poling, with the assistance of mechanical loading, consumes less energy than electrical poling without mechanical loading. Such assistance reduces the threshold field for domain switching by ~ 40%, which provides a valuable way to reduce the energy consumption of ferroelectric devices.
7. Ferroelastic domain switching can be reversible (elastic) and irreversible (plastic) depending on the level of applied stress. Under a low level of applied stress, the formation of 90° nanodomains is fully reversible. Medium levels of applied stress help overcome the internal energy barriers of domain nucleation and domain-wall motion, leading to irreversible domain evolution. The stress induces 180° domain switching, introducing high remnant polarisation after the retraction of mechanical loading. A high level of stress not only induces 180° domain switching, but also overwhelms the strong pinning effect, causing the formation of large single domains. These important discoveries provide the potential for subverting the constraint effect caused by compositional variation or defects in ferroelectric materials by utilising large mechanical stress.

7.2. Future perspectives

Although many significant conclusions have been drawn from this thesis project, some outstanding issues still remain. Further investigations will be needed in the future as an extension of this thesis project. These include:

1. Many experimental parameters can affect the size of domains written by the e-beam. These include electron energy, e-beam intensity and specimen thickness. For example, a very thin specimen may not provide enough positive charges generated by the interaction between the e-beam and the specimen, while a very large specimen thickness will deteriorate the spatial resolution of the domain writing. It is therefore necessary to conduct thorough theoretical and experimental investigation to understand how electron energy, e-beam intensity and electron exposure time affect the generated electron field and what the optimal specimen thickness is for the highest possible spatial resolution for domain writing. These concerns are critical for the practical applications of domain writing using an e-beam.
2. It is difficult to manufacture freestanding, thin samples and to read data from the samples. Therefore, it is necessary to test double-layer, thin-film samples for practical applications. This cannot be achieved in a TEM. E-beam lithography is an appropriate tool for manipulating ferroelectric domain structures in double-layer thin films. To avoid the supplementing of positive charges to thin films after e-beam illumination, the substrate of the thin-film sample must be an insulator or, at least, a semiconductor. The thin film is constrained by the substrate because of the substrate/film lattice mismatch, by which domain switching is impeded. More experiments must be conducted to explore the best writing pathway when using a double-layer, thin-film sample.
3. As presented in Chapter 4, mechanically stable and unstable states can serve as two logical states—zero and one—for data storage. The data reading and writing processes require repeated mechanical and electrical loadings. These processes introduce significant mechanical stress to the ferroelectric materials used as data-storage media and could lead to the fatigue and failure of the materials. Repeated

ferroelectric domain switching millions of times may introduce significant crystalline defects and large compositional variations, posing significant constraints to domains and domain walls that may change domain switching behaviour. Therefore, it is of significance to conduct in-situ investigations of the fatigue behaviour, which can be induced by repeated domain switching. This could be achieved by using electrical PTP devices together with the Hystron PI-95 PicoIndentor, allowing repeated electrical and mechanical loadings under a TEM.

4. Although the tetragonal crystals usually possess very large domain bands while ferroelectrics having the MPB composition shows wave form domains that can be a couple orders of magnitude smaller than domain bands, the shape of the domain affect little on the performance of a ferroelectric memory cell. If a relaxor ferroelectric for memory application is chosen, a rhombohedral phase with poling direction along <001> is preferred [286] as a fatigue-free behaviour has been observed for a loading cycle of up to 10^5. The use of relaxor-based ferroelectric in memory devices has not been proposed nor tested. Therefore, detailed on domain reversal, writing cycles, and writing frequency are needed to be tested.
5. The introduction of 90° nanoscale domains facilitates 180° ferroelectric switching and reduces the threshold field for ferroelectric switching by ~ 40% under a low level of applied mechanical stress of ~ 190 MPa. It is expected that the reduction of this threshold field could be maximised at the most appropriate applied mechanical stress. However, it is difficult to increase the applied compression stress because of the likelihood of bending thin specimens under compression. However, since both compression and tensile stresses can trigger 90° nanodomain formation, tensile stress can replace compression stress for experiments requiring high levels of applied stress to avoid bending. The experiments can be conducted using an e-PTP.

An e-PTP device is modified from a traditional PTP device by depositing an electrical circuit on the PTP, as shown in Figure 7-1 (a). The e-PTP allows for applications of tensile stress and electrical bias along the same direction as that indicated in Figure 7-1 (b). To explore the effect of electrical poling under tensile stress along a vertical direction, I can deposit two platinum-conducted wires along two edges of the specimen. Because ferroelectric materials are insulators, the electrons flow from one conducted wire to the other, forming a vertical electric field that is perpendicular to the applied tensile stress direction, as shown in Figure 7-1 (c).

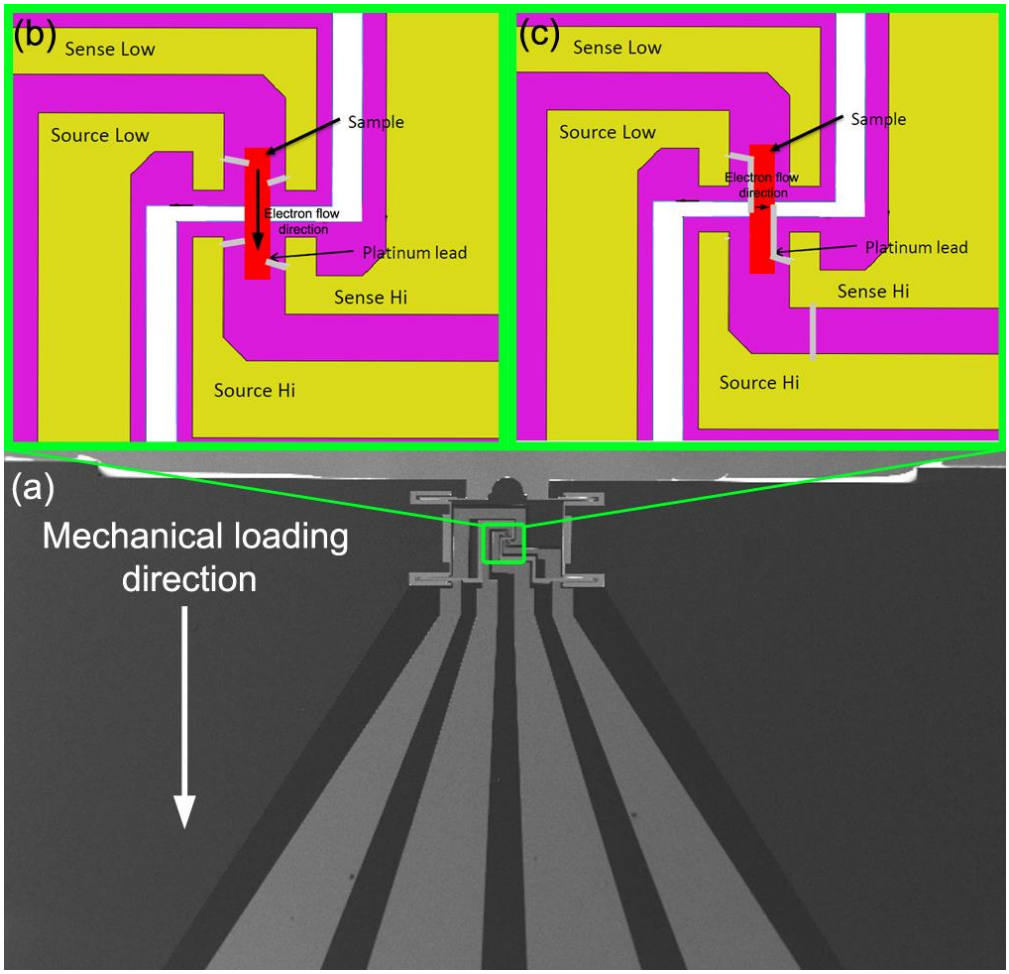

Figure 7-1 (a) An e-PTP device with integrated circuits. **(b)** A schematic drawing of the magnified area from **(a)**; the electron-flow direction is the same as the mechanical loading direction**. (c)** A schematic drawing of the magnified area from **(a)**; the electron-flow direction is perpendicular to the mechanical loading direction.

6. Ferroelectric materials possess pyroelectric properties. Therefore, ferroelectric domains also respond to external heating/cooling stimulation. My preliminary results of heating the relaxor-based ferroelectric PMN-38%PT shows that nanoscale domains—not limited to 90° domains—formed during the cooling process. In the meantime, pinned micro-domain walls disappeared after cooling to room temperature. These results indicate a notable remnant strain in ferroelectric materials and that the pinning effect can also be eliminated after heat treatment. Enlightened by this, it is possible to combine heat treatment with mechanical and/or electrical stimulations to improve the performance of ferroelectric devices.
7. It is interesting to see zipper-like domain walls to separating the energy unflavoured head-to-head and tail-to-tail charged domains. The domain walls still exists even after the retraction of the external electric field, which was not expected before. We will work on this in the future to characterise such interesting domain walls to get further insight on how polarization revolute inside these domain walls.
8. The strong pinning effect on the micro-domain walls contributes significant constraint to the domain and affects domain switching substantially. It has been speculated that pinning sources could be oxygen vacancies, topological defects and compositional variants. However, there has been no solid evidence to verify the nature of the sources. Advanced structural characterisation is needed to understand the pinning sources. A near-edge electron energy-loss spectroscopy (EELS) structure may assist in characterising the electronic structure and the chemical composition[230] of the domain walls. A high-spatial-resolution bright-field STEM technique[324] can help verify oxygen vacancies or other types of defects. By

ascertaining the reasons for the pinning effects, I can develop greater control over ferroelectric behaviours.

References

1. Bechmann R. ELASTIC, PIEZOELECTRIC, AND DIELECTRIC CONSTANTS OF POLARIZED BARIUM TITANATE CERAMICS AND SOME APPLICATIONS OF THE PIEZOELECTRIC EQUATIONS. *Journal of the Acoustical Society of America* **28**, 347-350 (1956).

2. Smolenskii GA, Agranovskaya AI. DIELECTRIC POLARIZATION OF A NUMBER OF COMPLEX COMPOUNDS. *Soviet Physics-Solid State* **1**, 1429-1437 (1960).

3. Curie J, P. C. Development by pressure of polar electricity in hemihedral crystals with inclined faces. *Bull Soc Miner* **3**, 4 (1880).

4. Ok KM, Chi EO, Halasyamani PS. Bulk characterization methods for non-centrosymmetric materials: second-harmonic generation, piezoelectricity, pyroelectricity, and ferroelectricity. *Chemical Society Reviews* **35**, 710-717 (2006).

5. Ozgur U, *et al.* A comprehensive review of ZnO materials and devices. *J Appl Phys* **98**, (2005).

6. Park SE, Shrout TR. Ultrahigh strain and piezoelectric behavior in relaxor based ferroelectric single crystals. *J Appl Phys* **82**, 1804-1811 (1997).

7. Whatmore RW. PYROELECTRIC DEVICES AND MATERIALS. *Reports on Progress in Physics* **49**, 1335-1386 (1986).

8. Chynoweth AG. DYNAMIC METHOD FOR MEASURING THE PYROELECTRIC EFFECT WITH SPECIAL REFERENCE TO BARIUM TITANATE. *J Appl Phys* **27**, 78-84 (1956).

9. Haertling GH. Ferroelectric ceramics: History and technology. *J Am Ceram Soc* **82**, 797-818 (1999).

10. Damjanovic D. Ferroelectric, dielectric and piezoelectric properties of ferroelectric thin films and ceramics. *Reports on Progress in Physics* **61**, 1267-1324 (1998).

11. Setter N, *et al*. Ferroelectric thin films: Review of materials, properties, and applications. *J Appl Phys* **100**, (2006).

12. Schlempe.Eo, Hamilton WC. NEUTRON-DIFFRACTION STUDY OF STRUCTURES OF FERROELECTRIC AND PARAELECTRIC AMMONIUM SULFATE. *Journal of Chemical Physics* **44**, 4498-& (1966).

13. Speck JS, Pompe W. DOMAIN CONFIGURATIONS DUE TO MULTIPLE MISFIT RELAXATION MECHANISMS IN EPITAXIAL FERROELECTRIC THIN-FILMS .1. THEORY. *J Appl Phys* **76**, 466-476 (1994).

14. Valasek J. Piezo-electric and allied phenomena in Rochelle salt. *Physical Review* **17**, 475-481 (1921).

15. Mouron P, Nguyen N, Choisnet J. CRYSTAL-CHEMISTRY OF THE CU(II)-TI(IV) PAIR IN ABO3 OXIDES OF THE CORUNDUM, BIXBYITE AND PEROVSKITE FAMILIES. *Revue De Chimie Minerale* **24**, 401-413 (1987).

16. Arlt G, Hennings D, Dewith G. DIELECTRIC-PROPERTIES OF FINE-GRAINED BARIUM-TITANATE CERAMICS. *J Appl Phys* **58**, 1619-1625 (1985).

17. Devonshire AF. THEORY OF BARIUM TITANATE .1. *Philos Mag* **40**, 1040-1063 (1949).

18. Uchino K, Sadanaga E, Hirose T. DEPENDENCE OF THE CRYSTAL-STRUCTURE ON PARTICLE-SIZE IN BARIUM-TITANATE. *J Am Ceram Soc* **72**, 1555-1558 (1989).

19. Matsumoto Y, Morikawa T, Adachi H, Hombo J. A NEW PREPARATION METHOD OF BARIUM-TITANATE PEROVSKITE FILM USING ELECTROCHEMICAL REDUCTION. *Materials Research Bulletin* **27**, 1319-1327 (1992).

20. Ouml;zen M, Mertens M, Snijkers F, Cool P. Hydrothermal synthesis and formation mechanism of tetragonal barium titanate in a highly concentrated alkaline solution. *Ceramics International* **42**, 10967-10975 (2016).

21. Zgonik M, *et al.* DIELECTRIC, ELASTIC, PIEZOELECTRIC, ELECTROOPTIC, AND ELASTO-OPTIC TENSORS OF BATIO3 CRYSTALS. *Phys Rev B* **50**, 5941-5949 (1994).

22. Frey MH, Payne DA. Grain-size effect on structure and phase transformations for barium titanate. *Phys Rev B* **54**, 3158-3168 (1996).

23. Barker AS, Loudon R. DIELECTRIC PROPERTIES AND OPTICAL PHONONS IN LINBO3. *Physical Review* **158**, 433-+ (1967).

24. Glass AM, Linde DVD, Negran TJ. HIGH-VOLTAGE BULK PHOTOVOLTAIC EFFECT AND THE PHOTOREFRACTIVE PROCESS IN LINBO3. *Appl Phys Lett* **25**, 233-235 (1974).

25. Jaffe B, Roth RS, Marzullo S. PIEZOELECTRIC PROPERTIES OF LEAD ZIRCONATE-LEAD TITANATE SOLID-SOLUTION CERAMICS. *J Appl Phys* **25**, 809-810 (1954).

26. Jaffe B, Roth RS, Marzullo S. PROPERTIES OF PIEZOELECTRIC CERAMICS IN THE SOLID-SOLUTION SERIES LEAD TITANATE-LEAD ZIRCONATE-LEAD OXIDE - TIN OXIDE AND LEAD TITANATE-LEAD HAFNATE. *Journal of Research of the National Bureau of Standards* **55**, 239-254 (1955).

27. Uchino K. *Designing with piezoelectric devices*. Amer Ceramic Soc (2002).

28. Cao WW, Cross LE. THEORETICAL-MODEL FOR THE MORPHOTROPIC PHASE-BOUNDARY IN LEAD ZIRCONATE LEAD TITANATE SOLID-SOLUTION. *Phys Rev B* **47**, 4825-4830 (1993).

29. Fan HQ, Kim HE. Perovskite stabilization and electromechanical properties of polycrystalline lead zinc niobate-lead zirconate titanate. *J Appl Phys* **91**, 317-322 (2002).

30. Yamamoto T. Ferroelectric properties of the PbZrO3-PbTiO3 system. *Jpn J Appl Phys Part 1 - Regul Pap Short Notes Rev Pap* **35**, 5104-5108 (1996).

31. Guo R, Cross LE, Park SE, Noheda B, Cox DE, Shirane G. Origin of the high piezoelectric response in PbZr1-xTixO3. *Phys Rev Lett* **84**, 5423-5426 (2000).

32. Randall CA, Kim N, Kucera JP, Cao WW, Shrout TR. Intrinsic and extrinsic size effects in fine-grained morphotropic-phase-boundary lead zirconate titanate ceramics. *J Am Ceram Soc* **81**, 677-688 (1998).

33. Eitel RE, Randall CA, Shrout TR, Rehrig PW, Hackenberger W, Park SE. New high temperature morphotropic phase boundary piezoelectrics based on Bi(Me)O-3-PbTiO3 ceramics. *Jpn J Appl Phys Part 1 - Regul Pap Short Notes Rev Pap* **40**, 5999-6002 (2001).

34. Shrout TR, Chang ZP, Kim NC, Markgraf S. DIELECTRIC BEHAVIOR OF SINGLE-CRYSTALS NEAR THE (1-X) PB(MG1/3NB2/3)O3-(X) PBTIO3 MORPHOTROPIC PHASE-BOUNDARY. *Ferroelectrics Letters Section* **12**, 63-69 (1990).

35. Anton SR, Sodano HA. A review of power harvesting using piezoelectric materials (2003-2006). *Smart Materials & Structures* **16**, R1-R21 (2007).

36. Shrout TR, Zhang SJ. Lead-free piezoelectric ceramics: Alternatives for PZT? *Journal of Electroceramics* **19**, 113-126 (2007).

37. Merz WJ. DOMAIN FORMATION AND DOMAIN WALL MOTIONS IN FERROELECTRIC BATIO3 SINGLE CRYSTALS. *Physical Review* **95**, 690-698 (1954).

38. Ishibashi Y, Takagi Y. FERROELECTRIC DOMAIN SWITCHING. *J Phys Soc Jpn* **31**, 506-+ (1971).

39. Kleemann W. RANDOM-FIELD INDUCED ANTIFERROMAGNETIC, FERROELECTRIC AND STRUCTURAL DOMAIN STATES. *International Journal of Modern Physics B* **7**, 2469-2507 (1993).

40. Whyte JR, Gregg JM. A diode for ferroelectric domain-wall motion. *Nat Commun* **6**, 7361 (2015).

41. Sahota H. Simulation of butterfly loops in ferroelectric materials. *Continuum Mechanics and Thermodynamics* **16**, 163-175 (2004).

42. Chew KH, Ong LH, Osman J, Tan EK, Tilley DR. Intrinsic hysteresis loops in ferroelectric film systems. *Ferroelectrics* **259**, 215-220 (2001).

43. Ong LH, Osman J, Tilley DR. Dielectric hysteresis loops of first-order antiferroelectrics. *Ferroelectrics* **355**, 130-135 (2007).

44. Ricinschi D, Okuyama M. Study of partially-switched states of ferroelectrics in relation to the spatial inhomogeneity of their domain structure. *Journal of Electroceramics* **24**, 33-38 (2010).

45. Wongdamnern N, Tangsritragul J, Ngamjarurojana A, Ananta S, Laosiritaworn Y, Yimnirun R. Hysteresis scaling relations in polycrystalline BaTiO3 bulk ceramics. *Materials Chemistry and Physics* **124**, 281-286 (2010).

46. Nomura S, Sawada S. ON THE HYSTERESIS LOOPS OF BATIO3 CERAMICS. *J Phys Soc Jpn* **4**, 120-121 (1949).

47. Pramanick A, Prewitt AD, Forrester JS, Jones JL. Domains, Domain Walls and Defects in Perovskite Ferroelectric Oxides: A Review of Present Understanding and Recent Contributions. *Critical Reviews in Solid State and Materials Sciences* **37**, 243-275 (2012).

48. Scott JF. Applications of modern ferroelectrics. *Science* **315**, 954-959 (2007).

49. John CS, Macleod TC, Evans J, Ho FD. Retention Analysis of a Non-Volatile Ferroelectric Memory Device. *Integrated Ferroelectrics* **140**, 23-34 (2012).

50. Hu ZJ, Tian MW, Nysten B, Jonas AM. Regular arrays of highly ordered ferroelectric polymer nanostructures for non-volatile low-voltage memories. *Nat Mater* **8**, 62-67 (2009).

51. Jeong DS, *et al*. Emerging memories: resistive switching mechanisms and current status. *Reports on Progress in Physics* **75**, (2012).

52. Ramesh R, Aggarwal S, Auciello O. Science and technology of ferroelectric films and heterostructures for non-volatile ferroelectric memories. *Materials Science & Engineering R-Reports* **32**, 191-236 (2001).

53. Asadi K, De Leeuw DM, De Boer B, Blom PWM. Organic non-volatile memories from ferroelectric phase-separated blends. *Nat Mater* **7**, 547-550 (2008).

54. Damjanovic D, Muralt P, Setter N. Ferroelectric Sensors. *Ieee Sensors Journal* **1**, 191-206 (2001).

55. Scott JF, Hoo YK. ELECTRICAL PROPERTIES OF FERROELECTRIC BaTiO3-on-Ni MULTILAYER CAPACITORS FOR ROOM-TEMPERATURE MAGNETOELECTRIC DETECTORS. *Integrated Ferroelectrics* **100**, 140-145 (2008).

56. Fabiny L, Vohra ST, Bucholtz F. HIGH-RESOLUTION FIBEROPTIC LOW-FREQUENCY VOLTAGE SENSOR-BASED ON THE ELECTROSTRICTIVE EFFECT. *Ieee Photonics Technology Letters* **5**, 952-953 (1993).

57. Guerra JDS, Pelaiz-Barranco A, Calderon-Pinar F, Perez-Martinez O, Gonzalez-Carmenate I. Ferroelectric ceramics for pyroelectric sensor. *Quimica Analitica* **18**, 60-61 (1999).

58. Pulskamp JS, Bedair SS, Polcawich RG, Judy D, Bhave SA, Ieee. Ferroelectric PZT RF MEMS Resonators. In: *2011 Joint Conference of the Ieee International Frequency Control Symposium/European Frequency and Time Forum Proceedings* (ed^(eds). Ieee (2011).

59. Kungl H, Hoffmann MJ. Method for the estimation of the total displacement of ferroelectric actuators under mixed thermal and electrical loading. *Sensors and Actuators a-Physical* **144**, 328-336 (2008).

60. Klotins E, Kundzins K, Andersen B, James A. The strain response of piezoelectric multilayer actuators under combined action of electric field and in-plane uniform load. *Ferroelectrics* **199**, 261-270 (1997).

61. Masuduzzaman M, Alam MA. Effective Nanometer Airgap of NEMS Devices Using Negative Capacitance of Ferroelectric Materials. *Nano Lett* **14**, 3160-3165 (2014).

62. Huber JE. Modelling and design of ferroelectric beam actuators. In: *Smart Structures and Materials 2004: Active Materials: Behavior and Mechanics* (ed^(eds Lagoudas DC). Spie-Int Soc Optical Engineering (2004).

63. Balakrishna AR, Huber JE, Landis CM. Nano-actuator concepts based on ferroelectric switching. *Smart Materials and Structures* **23**, (2014).

64. Udayakumar KR, *et al.* *FERROELECTRIC THIN-FILM ULTRASONIC MICROMOTORS*. I E E E (1991).

65. Flynn AM, Udayakumar KR, Barrett DS, McLurkin JD, Franck DL, Shectman AN. Tomorrow's surgery: micromotors and microrobots for minimally invasive procedures. *Minimally Invasive Therapy & Allied Technologies* **7**, 343-352 (1998).

66. Chen BL, Huang PC, Jang LS, Chen MK. Electrical failure analysis of peristaltic micropumps fabricated with PZT actuators. *Microelectronics Reliability* **52**, 1080-1085 (2012).

67. Zhang SH, *et al.* Relaxor ferroelectric polymers, thin film devices, and ink-jet microprinting for thin film device fabrication. *Ferroelectrics* **342**, 43-+ (2006).

68. Li SK, *et al.* Preparation of Diffuser-Type Micropumps Using PZT Thin Films Prepared by Metallo-Organic Compound Decomposition Process. *Ferroelectrics* **383**, 144-150 (2009).

69. Asthagiri A, Wu Z, Choudhury N, Cohen RE. Advances in first-principles studies of transducer materials. *Ferroelectrics* **333**, 69-78 (2006).

70. Davidsen RE, Smith SW. A two-dimensional array for B-mode and volumetric imaging with multiplexed electrostrictive elements. *Ultrasonic Imaging* **19**, 235-250 (1997).

71. Zhu BP, *et al.* Lift-Off PMN-PT Thick Film for High-Frequency Ultrasonic Biomicroscopy. *J Am Ceram Soc* **93**, 2929-2931 (2010).

72. Mathews S, Semenova Y, Farrell G. Electronic tunability of ferroelectric liquid crystal infiltrated photonic crystal fibre. *Electronics Letters* **45**, 617-U612 (2009).

73. Budaszewski D, Srivastava AK, Wolinski TR, Chigrinov VG. Photo-aligned photonic ferroelectric liquid crystal fibers. *Journal of the Society for Information Display* **23**, 196-201 (2015).

74. Lin PT, Liu Z, Wessels BW. Ferroelectric thin film photonic crystal waveguide and its electro-optic properties. *Journal of Optics a-Pure and Applied Optics* **11**, (2009).

75. Kung AH, Ieee. *Ferroelectric Photonic Structures: Characterization and Device Demonstration*. Ieee (2007).

76. Garcia V, Bibes M. ELECTRONICS Inside story of ferroelectric memories. *Nature* **483**, 279-281 (2012).

77. Han ST, Zhou Y, Roy VAL. Towards the Development of Flexible Non-Volatile Memories. *Adv Mater* **25**, 5425-5449 (2013).

78. Das S, Appenzeller J. FETRAM. An Organic Ferroelectric Material Based Novel Random Access Memory Cell. *Nano Lett* **11**, 4003-4007 (2011).

79. Messenger GC, Coppage FN. FERROELECTRIC MEMORIES - A POSSIBLE ANSWER TO THE HARDENED NONVOLATILE QUESTION. *Ieee Transactions on Nuclear Science* **35**, 1461-1466 (1988).

80. Lu H, *et al.* Mechanical Writing of Ferroelectric Polarization. *Science* **336**, 59-61 (2012).

81. Chan HB, Aksyuk VA, Kleiman RN, Bishop DJ, Capasso F. Quantum mechanical actuation of microelectromechanical systems by the Casimir force. *Science* **291**, 1941-1944 (2001).

82. Eom CB, Trolier-McKinstry S. Thin-film piezoelectric MEMS. *MRS Bull* **37**, 1007-1021 (2012).

83. Muralt P. Ferroelectric thin films for micro-sensors and actuators: a review. *Journal of Micromechanics and Microengineering* **10**, 136-146 (2000).

84. Spearing SM. Materials issues in microelectromechanical systems (MEMS). *Acta Materialia* **48**, 179-196 (2000).

85. Ekinci KL, Roukes ML. Nanoelectromechanical systems. *Review of Scientific Instruments* **76**, (2005).

86. Li M, Tang HX, Roukes ML. Ultra-sensitive NEMS-based cantilevers for sensing, scanned probe and very high-frequency applications. *Nat Nanotechnol* **2**, 114-120 (2007).

87. Cimalla V, Pezoldt J, Ambacher O. Group III nitride and SiC based MEMS and NEMS: materials properties, technology and applications. *J Phys D-Appl Phys* **40**, 6386-6434 (2007).

88. Kuwata J, Uchino K, Nomura S. PHASE-TRANSITIONS IN THE PB(ZN1/3NB2/3)O3-PBTIO3 SYSTEM. *Ferroelectrics* **37**, 579-582 (1981).

89. Yokomizo Y, Takahashi T, Nomura S. FERROELECTRIC PROPERTIES OF PB(ZN1/3NB2/3)O3. *J Phys Soc Jpn* **28**, 1278-+ (1970).

90. Birks EH. THE ELECTROCALORIC EFFECT IN PB(SC0.5NB0.5)O3 CERAMIC. *Physica Status Solidi a-Applied Research* **94**, 523-527 (1986).

91. Kersten O, Rost A, Schmidt G, Sternberg A. DIELECTRIC AND THERMAL-PROPERTIES OF PB(SC0.5NB0.5)O3 CERAMIC. *Ferroelectrics Letters Section* **1**, 171-174 (1984).

92. Cross LE. RELAXOR FERROELECTRICS. *Ferroelectrics* **76**, 241-267 (1987).

93. Bokov AA, Ye ZG. Recent progress in relaxor ferroelectrics with perovskite structure. *Journal of Materials Science* **41**, 31-52 (2006).

94. Samara GA. The relaxational properties of compositionally disordered ABO(3) perovskites. *J Phys-Condes Matter* **15**, R367-R411 (2003).

95. Ye ZG. Relaxor ferroelectric complex perovskites: Structure, properties and phase transitions. In: *Oxides: Phase Transitions, Non Stoichiometry, Superconductors* (ed^(eds Boulesteix C). Trans Tech Publications (1998).

96. Li F, Jin L, Xu Z, Zhang S. Electrostrictive effect in ferroelectrics: An alternative approach to improve piezoelectricity. *Applied Physics Reviews* **1**, 011103 (2014).

97. Viehland D, Jang SJ, Cross LE, Wuttig M. DEVIATION FROM CURIE-WEISS BEHAVIOR IN RELAXOR FERROELECTRICS. *Phys Rev B* **46**, 8003-8006 (1992).

98. Westphal V, Kleemann W, Glinchuk MD. DIFFUSE PHASE-TRANSITIONS AND RANDOM-FIELD-INDUCED DOMAIN STATES OF THE RELAXOR FERROELECTRIC PBMG1/3NB2/3O3. *Phys Rev Lett* **68**, 847-850 (1992).

99. Hlinka J, Petzelt J, Kamba S, Noujni D, Ostapchuk T. Infrared dielectric response of relaxor ferroelectrics. *Phase Transitions* **79**, 41-78 (2006).

100. Tu CS, Chen LF, Schmidt VH, Tsai CL. Phases and domain structures in relaxor-based ferroelectric (PbMg1/3Nb2/3O3)(0.69)(PbTiO3)(0.31) single crystal. *Jpn J Appl Phys Part 1 - Regul Pap Short Notes Rev Pap* **40**, 4118-4125 (2001).

101. Vugmeister BE. Polarization dynamics and formation of polar nanoregions in relaxor ferroelectrics. *Phys Rev B* **73**, (2006).

102. Macutkevic J, Banys J, Bussmann-Holder A, Bishop AR. Origin of polar nanoregions in relaxor ferroelectrics: Nonlinearity, discrete breather formation, ge transfer. *Phys Rev B* **83**, (2011).

103. Hirota K, Ye ZG, Wakimoto S, Gehring PM, Shirane G. Neutron diffuse scattering from polar nanoregions in the relaxor Pb(Mg1/3Nb2/3)O-3. *Phys Rev B* **65**, (2002).

104. Li F, *et al.* The origin of ultrahigh piezoelectricity in relaxor-ferroelectric solid solution crystals. *Nat Commun* **7**, 13807 (2016).

105. Setter N, Cross LE. THE ROLE OF B-SITE CATION DISORDER IN DIFFUSE PHASE-TRANSITION BEHAVIOR OF PEROVSKITE FERROELECTRICS. *J Appl Phys* **51**, 4356-4360 (1980).

106. Shrout TR, Fielding J. *RELAXOR FERROELECTRIC MATERIALS*. I E E E (1990).

107. Semenovskaya S, Khachaturyan AG. Ferroelectric transition in a random field: Possible relation to relaxor ferroelectrics. *Ferroelectrics* **206**, 157-180 (1998).

108. Skulski R. Superparaelectric behaviours of relaxor ferroelectrics. *Materials Science and Engineering B-Solid State Materials for Advanced Technology* **64**, 39-43 (1999).

109. Glinchuk MD. Relaxor ferroelectrics: from cross superparaelectric model to random field theory. *British Ceramic Transactions* **103**, 76-82 (2004).

110. Burns G, Dacol FH. GLASSY POLARIZATION BEHAVIOR IN FERROELECTRIC COMPOUNDS PB(MG1/3NB2/3)O3 AND PB(ZN1/3NB2/3)O3. *Solid State Commun* **48**, 853-856 (1983).

111. Colla EV, Vigil D, Timmerwilke J, Weissman MB, Viehland DD, Dkhil B. Stability of glassy and ferroelectric states in the relaxors PbMg1/3Nb2/3O3 and PbMg1/3Nb2/3O3-12% PbTiO3. *Phys Rev B* **75**, (2007).

112. Fisch R. Random-field models for relaxor ferroelectric behavior. *Phys Rev B* **67**, (2003).

113. Qu SH, Cao WQ. Research on polarization effect for relaxor ferroelectrics by spherical random bond-random field model. *Acta Physica Sinica* **63**, (2014).

114. Pirc R, Blinc R, Vikhnin VS. Effect of polar nanoregions on giant electrostriction and piezoelectricity in relaxor ferroelectrics. *Phys Rev B* **69**, (2004).

115. Bhalla AS, Guo RY, Roy R. The perovskite structure - a review of its role in ceramic science and technology. *Materials Research Innovations* **4**, 3-26 (2000).

116. Park SE, Shrout TR. Relaxor based ferroelectric single crystals for electro-mechanical actuators. *Materials Research Innovations* **1**, 20-25 (1997).

117. Nomura; S, Takahashi; T, Yokomizo Y. Ferroelectric Properties in the System Pb(Zn1/3Nb2/3)O3-PbTiO3. *J Phys Soc Jpn* **27**, 262 (1969).

118. Wada S, Park SE, Cross LE, Shrout TR. Engineered domain configuration in rhombohedral PZN-PT single crystals and their ferroelectric related properties. *Ferroelectrics* **221**, 147-155 (1999).

119. Park SE, Shrout TR. Characteristics of relaxor-based piezoelectric single crystals for ultrasonic transducers. *Ieee Transactions on Ultrasonics Ferroelectrics and Frequency Control* **44**, 1140-1147 (1997).

120. Zhao XY, Fang BJ, Cao H, Guo YP, Luo HS. Dielectric and piezoelectric performance of PMN-PT single crystals with compositions around the MPB: influence of composition, poling field and crystal orientation. *Materials Science and Engineering B-Solid State Materials for Advanced Technology* **96**, 254-262 (2002).

121. Noheda B. Structure and high-piezoelectricity in lead oxide solid solutions. *Current Opinion in Solid State & Materials Science* **6**, 27-34 (2002).

122. Choi SW, Shrout TR, Jang SJ, Bhalla AS. MORPHOTROPIC PHASE-BOUNDARY IN PB(MG1/3NB2/3)O3-PBTIO3 SYSTEM. *Materials Letters* **8**, 253-255 (1989).

123. Gupta SM, Viehland D. Tetragonal to rhombohedral transformation in the lead zirconium titanate lead magnesium niobate lead titanate crystalline solution. *J Appl Phys* **83**, 407-414 (1998).

124. Xia ZG, Li QA. Structural phase transformation and electrical properties of (0.90-x)Pb(Mg1/3Nb2/3)O-3-xPbTiO(3)-0.10Pb(Fe1/2Nb1/2)O-3 ferroelectric ceramics near the morphotropic phase boundary. *Acta Materialia* **55**, 6176-6181 (2007).

125. Chang WS, Lim LC, Yang P, Tu CS. Rhombohedral-to-tetragonal phase transformation and thermal depolarization in relaxor-based ferroelectric single crystal. *Appl Phys Lett* **93**, (2008).

126. Wang H, Zhu J, Lu N, Bokov AA, Ye ZG, Zhang XW. Hierarchical micro-/nanoscale domain structure in M-C phase of (1-x)Pb(Mg1/3Nb2/3)O-3-xPbTiO(3) single crystal. *Appl Phys Lett* **89**, (2006).

127. Ishibashi Y, Iwata M. Morphotropic phase boundary in solid solution systems of perovskite-type oxide ferroelectrics. *Japanese Journal of Applied Physics Part 2-Letters* **37**, L985-L987 (1998).

128. Zhang Y, Xue DZ, Wu HJ, Ding XD, Lookman T, Ren XB. Adaptive ferroelectric state at morphotropic phase boundary: Coexisting tetragonal and rhombohedral phases. *Acta Materialia* **71**, 176-184 (2014).

129. Bhattacharyya S, Jinschek JR, Cao H, Wang YU, Li JF, Viehland D. Direct high-resolution transmission electron microscopy observation of tetragonal nanotwins within the monoclinic M(C) phase of Pb(Mg(1/3)Nb(2/3))O(3)-0.35PbTiO(3) crystals. *Appl Phys Lett* **92**, (2008).

130. Vanderbilt D, Cohen MH. Monoclinic and triclinic phases in higher-order Devonshire theory. *Phys Rev B* **63**, (2001).

131. Noheda B, Cox DE, Shirane G, Gonzalo JA, Cross LE, Park SE. A monoclinic ferroelectric phase in the Pb(Zr1-xTix)O-3 solid solution. *Appl Phys Lett* **74**, 2059-2061 (1999).

132. Xu GS, Luo HS, Xu HQ, Yin ZW. Third ferroelectric phase in PMNT single crystals near the morphotropic phase boundary composition. *Phys Rev B* **64**, (2001).

133. Schonau KA, *et al.* Nanodomain structure of Pb Zr1-xTix O-3 at its morphotropic phase boundary: Investigations from local to average structure. *Phys Rev B* **75**, (2007).

134. Davis M, Damjanovic D, Setter N. Electric-field-, temperature-, and stress-induced phase transitions in relaxor ferroelectric single crystals. *Phys Rev B* **73**, (2006).

135. Fu HX, Cohen RE. Polarization rotation mechanism for ultrahigh electromechanical response in single-crystal piezoelectrics. *Nature* **403**, 281-283 (2000).

136. Ye ZG, Dong M. Morphotropic domain structures and phase transitions in relaxor-based piezo-/ferroelectric (1-x)Pb(Mg1/3Nb2/3)O-3-xPbTiO(3) single crystals. *J Appl Phys* **87**, 2312-2319 (2000).

137. Zekria D, Shuvaeva VA, Glazer AM. Birefringence imaging measurements on the phase diagram of Pb(Mg1/3Nb2/3)O-3-PbTiO3. *J Phys-Condes Matter* **17**, 1593-1600 (2005).

138. Guo YP, Luo HS, Chen KP, Xu HQ, Zhang XW, Yin ZW. Effect of composition and poling field on the properties and ferroelectric phase-stability of Pb(Mg1/3Nb2/3)O-3-PbTiO3 crystals. *J Appl Phys* **92**, 6134-6138 (2002).

139. Zhang R, Jiang B, Cao WW. Orientation dependence of piezoelectric properties of single domain 0.67Pb(Mn1/3Nb2/3)O-3-0.33PbTiO(3) crystals. *Appl Phys Lett* **82**, 3737-3739 (2003).

140. Davis M, Damjanovic D, Setter N. Pyroelectric properties of (1-x)Pb(Mg1/3Nb2/3)O-3-xPbTiO(3) and (1-x)Pb(Zn1/3Nb2/3)O-3-xPbTiO(3) single crystals measured using a dynamic method. *J Appl Phys* **96**, 2811-2815 (2004).

141. Davis M, Damjanovic D, Hayem D, Setter N. Domain engineering of the transverse piezoelectric coefficient in perovskite ferroelectrics. *J Appl Phys* **98**, (2005).

142. Delaunay T, Le Clezio E, Lematre M, Feuillard G. Relations between single-domain and multidomain piezoelastic properties in single crystals. *Ieee Transactions on Ultrasonics Ferroelectrics and Frequency Control* **53**, 1974-1981 (2006).

143. Zhang R, Cao WW. Transformed material coefficients for single-domain 0.67Pb(Mg1/3Nb2/3)O-3-0.33PbTiO(3) single crystals under differently defined coordinate systems. *Appl Phys Lett* **85**, 6380-6382 (2004).

144. Zhang R, Jiang B, Cao WW. Single-domain properties of 0.67Pb(Mg1/3Nb2/3)O-3-0.33PbTiO(3) single crystals under electric field bias. *Appl Phys Lett* **82**, 787-789 (2003).

145. Sato Y, Hirayama T, Ikuhara Y. Real-Time Direct Observations of Polarization Reversal in a Piezoelectric Crystal: Pb(Mg1/3Nb2/3)O-3-PbTiO3 Studied via In Situ Electrical Biasing Transmission Electron Microscopy. *Phys Rev Lett* **107**, (2011).

146. Zhang W, Bhattacharya K. A computational model of ferroelectric domains. Part I: model formulation and domain switching. *Acta Materialia* **53**, 185-198 (2005).

147. Tu CS, Tsai CL, Schmidt VH, Luo HS, Yin ZW. Dielectric, hypersonic, and domain anomalies of (PbMg1/3Nb2/3O3)(1-x)(PbTiO3)(x) single crystals. *J Appl Phys* **89**, 7908-7916 (2001).

148. Ye ZG, Dong M, Zhang L. Domain structures and phase transitions of the relaxor-based piezo-/ferroelectric (1-x)Pb(Zn1/3Nb2/3)O-3-xPbTiO(3) single crystals. *Ferroelectrics* **229**, 223-+ (1999).

149. Cao H, Li JF, Viehland D, Xu GY. Fragile phase stability in (1-x)Pb(Mg1/3Nb2/3O3)-xPbTiO(3) crystals: A comparison of 001 and 110 field-cooled phase diagrams. *Phys Rev B* **73**, (2006).

150. Sato Y, Hirayama T, Ikuhara Y. Evolution of nanodomains under DC electrical bias in Pb(Mg1/3Nb2/3) O-3-PbTiO3: An In-situ transmission electron microscopy study. *Appl Phys Lett* **100**, (2012).

151. Wang Z, Zhang R, Sun EW, Cao WW. Contributions of domain wall motion to complex electromechanical coefficients of 0.62Pb(Mg1/3Nb2/3)O-3-0.38PbTiO(3) crystals. *J Appl Phys* **107**, (2010).

152. Maxwell JC. A dynamical theory of the electromagnetic field. *Phil Trans R Soc Lond* **115**, 459-512 (1865).

153. Kimura T, Goto T, Shintani H, Ishizaka K, Arima T, Tokura Y. Magnetic control of ferroelectric polarization. *Nature* **426**, 55-58 (2003).

154. Eerenstein W, Mathur ND, Scott JF. Multiferroic and magnetoelectric materials. *Nature* **442**, 759-765 (2006).

155. Cheong SW, Mostovoy M. Multiferroics: a magnetic twist for ferroelectricity. *Nat Mater* **6**, 13-20 (2007).

156. Liu M, *et al.* Giant Electric Field Tuning of Magnetic Properties in Multiferroic Ferrite/Ferroelectric Heterostructures. *Adv Funct Mater* **19**, 1826-1831 (2009).

157. Chanthbouala A, *et al.* Solid-state memories based on ferroelectric tunnel junctions. *Nat Nanotechnol* **7**, 101-104 (2012).

158. Van Aken BB, Palstra TTM, Filippetti A, Spaldin NA. The origin of ferroelectricity in magnetoelectric YMnO3. *Nat Mater* **3**, 164-170 (2004).

159. Chae SC, *et al.* Direct Observation of the Proliferation of Ferroelectric Loop Domains and Vortex-Antivortex Pairs. *Phys Rev Lett* **108**, (2012).

160. Tomuta DG, Ramakrishnan S, Nieuwenhuys GJ, Mydosh JA. The magnetic susceptibility, specific heat and dielectric constant of hexagonal YMnO3, LuMnO3 and ScMnO3. *J Phys-Condes Matter* **13**, 4543-4552 (2001).

161. Choi T, Horibe Y, Yi HT, Choi YJ, Wu WD, Cheong SW. Insulating interlocked ferroelectric and structural antiphase domain walls in multiferroic YMnO3. *Nat Mater* **9**, 253-258 (2010).

162. Li J, *et al.* Scanning secondary-electron microscopy on ferroelectric domains and domain walls in YMnO3. *Appl Phys Lett* **100**, (2012).

163. Abrahams SC. Ferroelectricity and structure in the YMnO3 family. *Acta Crystallogr Sect B-Struct Sci* **57**, 485-490 (2001).

164. Aikawa Y, Katsufuji T, Arima T, Kato K. Effect of Mn trimerization on the magnetic and dielectric properties of hexagonal YMnO3. *Phys Rev B* **71**, (2005).

165. Chen Z, Wang X, Ringer S, Liao X. Manipulation of Nanoscale Domain Switching Using an Electron Beam with Omnidirectional Electric Field Distribution. *Phys Rev Lett* **117**, (2016).

166. Kumagai Y, Spaldin NA. Structural domain walls in polar hexagonal manganites. *Nat Commun* **4**, (2013).

167. Han MG, *et al.* Ferroelectric Switching Dynamics of Topological Vortex Domains in a Hexagonal Manganite. *Adv Mater* **25**, 2415-2421 (2013).

168. Meier D, *et al.* Anisotropic conductance at improper ferroelectric domain walls. *Nat Mater* **11**, 284-288 (2012).

169. Spaldin NA. Fundamental size limits in ferroelectricity. *Science* **304**, 1606-1607 (2004).

170. Salje E. PHASE-TRANSITIONS IN FERROELASTIC AND CO-ELASTIC CRYSTALS. *Ferroelectrics* **104**, 111-120 (1990).

171. Salje EKH. CRYSTALLOGRAPHY AND STRUCTURAL PHASE-TRANSITIONS, AN INTRODUCTION. *Acta Crystallographica a-Foundation and Advances* **47**, 453-+ (1991).

172. Salje EKH. Ferroelastic Materials. In: *Annual Review of Materials Research, Vol 42* (ed^(eds Clarke DR). Annual Reviews (2012).

173. Vlokh R, Martynyuk-Lototska I. Ferroelastic crystals as effective acoustooptic materials. *Ukrainian Journal of Physical Optics* **10**, 89-99 (2009).

174. Lookman T, Shenoy SR, Rasmussen KO, Saxena A, Bishop AR. Ferroelastic dynamics and strain compatibility. *Phys Rev B* **67**, (2003).

175. Wang J, Shi SQ, Chen LQ, Li YL, Zhang TY. Phase field simulations of ferroelectric/ferroelastic polarization switching. *Acta Materialia* **52**, 749-764 (2004).

176. Baek SH, *et al.* Ferroelastic switching for nanoscale non-volatile magnetoelectric devices. *Nat Mater* **9**, 309-314 (2010).

177. Wang CS, *et al.* Ferroelastic switching in a layered-perovskite thin film. *Nat Commun* **7**, (2016).

178. Salje E, Hoppmann G. DIRECT OBSERVATION OF FERROELASTICITY IN PB3(PO4)2-PB3(VO4)2. *Materials Research Bulletin* **11**, 1545-1549 (1976).

179. Salje EKH, Graemebarber A, Carpenter MA, Bismayer U. LATTICE-PARAMETERS, SPONTANEOUS STRAIN AND PHASE-TRANSITIONS IN PB3(PO4)2. *Acta Crystallogr Sect B-Struct Sci* **49**, 387-392 (1993).

180. Bismayer U, *et al.* Ferroelastic domains in lead phosphate-arsenate: An AFM, X-ray diffraction, TEM and Raman study. *Phase Transitions* **71**, 243-270 (2000).

181. Salje E, Wruck B. SPECIFIC-HEAT MEASUREMENTS AND CRITICAL EXPONENTS OF THE FERROELASTIC PHASE-TRANSITION IN PB3(PO4)2 AND PB3(P1-XASXO4)2. *Phys Rev B* **28**, 6510-6518 (1983).

182. Anbusathaiah V, *et al.* Ferroelastic domain wall dynamics in ferroelectric bilayers. *Acta Materialia* **58**, 5316-5325 (2010).

183. Kim K, Huber JE. In situ observation of ferroelastic domain evolution in a near-morphotropic Pb(Zr,Ti)O-3 ceramic by piezoresponse force microscopy. *J Eur Ceram Soc* **35**, 1459-1468 (2015).

184. Gao P, *et al.* Atomic-scale mechanisms of ferroelastic domain-wall-mediated ferroelectric switching. *Nat Commun* **4**, (2013).

185. Yuan RL, Duan L, Du XY, Li Y. Identification and mechanical control of ferroelastic domain structure in rhombohedral CaMn7O12. *Phys Rev B* **91**, (2015).

186. Potnis P, Huber J. In-situ observation of needle domain evolution in barium titanate single crystals. *J Eur Ceram Soc* **33**, 327-333 (2013).

187. Edwards D, *et al.* Local Probing of Ferroelectric and Ferroelastic Switching through Stress-Mediated Piezoelectric Spectroscopy. *Advanced Materials Interfaces* **3**, (2016).

188. Okayasu M, Sato K, Kusaba Y. Domain switching characteristics of lead zirconate titanate piezoelectric ceramics during mechanical compressive loading. *J Eur Ceram Soc* **31**, 129-140 (2011).

189. Reichmann A, Mitsche S, Zankel A, Poelt P, Reichmann K. In situ mechanical compression of polycrystalline BaTiO3 in the ESEM. *J Eur Ceram Soc* **34**, 2211-2215 (2014).

190. Gao P, *et al.* Ferroelastic domain switching dynamics under electrical and mechanical excitations. *Nat Commun* **5**, (2014).

191. Majdoub MS, Sharma P, Cagin T. Enhanced size-dependent piezoelectricity and elasticity in nanostructures due to the flexoelectric effect. *Phys Rev B* **77**, (2008).

192. Lee D, *et al.* Giant Flexoelectric Effect in Ferroelectric Epitaxial Thin Films. *Phys Rev Lett* **107**, (2011).

193. Li JH, Lin PT, Wessels BW. Polarization reversal and backswitching dynamics in epitaxial BaTiO3 thin films. *J Appl Phys* **106**, (2009).

194. Zhang R, Jiang B, Cao WW. Superior d(32)(*) and k(32)(*) coefficients in 0.955Pb(Zn1/3Nb2/3)O-3-0.045PbTiO(3) and 0.92Pb(Zn1/3Nb2/3)O-3-0.08PbTiO(3) single crystals poled along 011. *Journal of Physics and Chemistry of Solids* **65**, 1083-1086 (2004).

195. Jiang YJ, Fang DN, Li FX. In situ observation of electric-field-induced domain switching near a crack tip in poled 0.62PbMg(1/3)Nb(2/3)O(3)-0.38PbTiO(3) single crystal. *Appl Phys Lett* **90**, (2007).

196. Rankin C, Chou CH, Conklin D, Bonnell DA. Polarization and local reactivity on organic ferroelectric surfaces: Ferroelectric nanolithography using poly(vinylidene fluoride). *ACS Nano* **1**, 234-238 (2007).

197. Khan AI, Marti X, Serrao C, Ramesh R, Salahuddin S. Voltage-Controlled Ferroelastic Switching in Pb(Zr0.2Ti0.8)O-3 Thin Films. *Nano Lett* **15**, 2229-2234 (2015).

198. Xu RJ, *et al.* Ferroelectric polarization reversal via successive ferroelastic transitions. *Nat Mater* **14**, 79-86 (2015).

199. Gao P, *et al.* Direct Observations of Retention Failure in Ferroelectric Memories. *Adv Mater* **24**, 1106-1110 (2012).

200. Stringer CJ, Randall CA. In situ TEM investigations of the high-temperature relaxor ferroelectric BiScO3-Pb(Mg1/3Nb2/3)O-3-PbTiO3 ternary solid solution. *J Am Ceram Soc* **90**, 1802-1807 (2007).

201. Tagantsev AK. VOGEL-FULCHER RELATIONSHIP FOR THE DIELECTRIC PERMITTIVITY OF RELAXOR FERROELECTRICS. *Phys Rev Lett* **72**, 1100-1103 (1994).

202. Viehland D, Jang SJ, Cross LE, Wuttig M. FREEZING OF THE POLARIZATION FLUCTUATIONS IN LEAD MAGNESIUM NIOBATE RELAXORS. *J Appl Phys* **68**, 2916-2921 (1990).

203. Vogel H. The temperature dependence law of the viscosity of fluids. *Physikalische Zeitschrift* **22**, 645-646 (1921).

204. Glazounov AE, Tagantsev AK. Direct evidence for Vogel-Fulcher freezing in relaxor ferroelectrics. *Appl Phys Lett* **73**, 856-858 (1998).

205. Shtrikman S, Wohlfarth EP. THE THEORY OF THE VOGEL-FULCHER LAW OF SPIN-GLASSES. *Physics Letters A* **85**, 467-470 (1981).

206. Mulvihill ML, Cross LE, Cao WW, Uchino K. Domain-related phase transitionlike behavior in lead zinc niobate relaxor ferroelectric single crystals. *J Am Ceram Soc* **80**, 1462-1468 (1997).

207. Gibbs AS, Knight KS, Lightfoot P. High-temperature phase transitions of hexagonal YMnO3. *Phys Rev B* **83**, (2011).

208. Tanaka K, *et al.* Scanning Nonlinear Dielectric Microscopy Nano-Science and Technology for Next Generation High Density Ferroelectric Data Storage. *Jpn J Appl Phys* **47**, 3311-3325 (2008).

209. Marsilius M, Frederick J, Hu W, Tan XL, Granzow T, Han PD. Mechanical Confinement: An Effective Way of Tuning Properties of Piezoelectric Crystals. *Adv Funct Mater* **22**, 797-802 (2012).

210. Chen Z, *et al.* Facilitation of ferroelectric switching via mechanical manipulation of hierarchical nanoscale domain structures. *Phys Rev Lett*, (2016).

211. Zhu H, Chu DP, Fleck NA, Pane I, Huber JE, Natori E. POLARIZATION CHANGE OF PZTN FERROELECTRIC THIN FILMS UNDER UNIFORM IN-PLANE TENSILE STRESS. *Integrated Ferroelectrics* **95**, 117-127 (2007).

212. de Broglie L. Research on the theory of quanta. *Annales de Physique* **10**, 22-128 (1925).

213. Busch H. Berechnung der Bahn von Kathodenstrahlen im axialsymmetrischen elektromagnetischen Felde. *Annalen der Physik* **386**, 974-993 (1926).

214. Busch H. Über die Wirkungsweise der Konzentrierungsspule bei der Braunschen Röhre. *Archiv für Elektrotechnik* **18**, 583-594 (1927).

215. Knoll M, Ruska E. Das Elektronenmikroskop. *Zeitschrift für Physik* **78**, 318-339 (1932).

216. Ruska E. über Fortschritte im Bau und in der Leistung des magnetischen Elektronenmikroskops. *Zeitschrift für Physik* **87**, 580-602 (1934).

217. Knoll M. Aufladepotentiel und Sekundäremission elektronenbestrahlter. *Körper Z tech Phys* **16**, 467-475 (1935).

218. Schrodinger E. An undulatory theory of the mechanics of atoms and molecules. *Physical Review* **28**, 1049-1070 (1926).

219. Heisenberg W. Über quantentheoretische Umdeutung kinematischer und mechanischer Beziehungen. *Zeitschrift für Physik* **33**, 879-893 (1925).

220. Bethe H. Theorie der Beugung von Elektronen an Kristallen. *Annalen der Physik* **392**, 55-129 (1928).

221. Martin LB, Boyde A, Grine FE. ENAMEL STRUCTURE IN PRIMATES - A REVIEW OF SCANNING ELECTRON-MICROSCOPE STUDIES. *Scanning Microscopy* **2**, 1503-1526 (1988).

222. Bogner A, Jouneau PH, Thollet G, Basset D, Gauthier C. A history of scanning electron microscopy developments: Towards "wet-STEM" imaging. *Micron* **38**, 390-401 (2007).

223. Joseph I. Goldstein, *et al. Scanning Electron Microscopy and X-Ray Microanalysis*. Springer US (1992).

224. Volkert CA, Minor AM. Focused ion beam microscopy and micromachining. *MRS Bull* **32**, 389-395 (2007).

225. Orloff J, Utlaut M, Swanson L. Physics of Liquid Metal Ion Sources. In: *High Resolution Focused Ion Beams: FIB and its Applications: The Physics of Liquid Metal Ion Sources and Ion Optics and Their Application to Focused Ion Beam Technology* (ed^(eds). Springer US (2003).

226. Williams DB, Carter CB. The Transmission Electron Microscope. In: *Transmission Electron Microscopy: A Textbook for Materials Science* (ed^(eds). Springer US (2009).

227. Steve R, Robert P. A review of focused ion beam applications in microsystem technology. *Journal of Micromechanics and Microengineering* **11**, 287 (2001).

228. Wall J, Langmore J, Isaacson M, Crewe AV. SCANNING-TRANSMISSION ELECTRON-MICROSCOPY AT HIGH-RESOLUTION. *Proc Natl Acad Sci U S A* **71**, 1-5 (1974).

229. Dellby N, Krivanek OL, Nellist PD, Batson PE, Lupini AR. Progress in aberration-corrected scanning transmission electron microscopy. *Journal of Electron Microscopy* **50**, 177-185 (2001).

230. Varela M, *et al.* Materials characterization in the aberration-corrected scanning transmission electron microscope. *Ann Rev Mater Res* **35**, 539-569 (2005).

231. Jia CL, *et al.* Unit-cell scale mapping of ferroelectricity and tetragonality in epitaxial ultrathin ferroelectric films. *Nat Mater* **6**, 64-69 (2007).

232. Muller DA. Structure and bonding at the atomic scale by scanning transmission electron microscopy. *Nat Mater* **8**, 263-270 (2009).

233. Espinosa HD, Bernal RA, Filleter T. In Situ TEM Electromechanical Testing of Nanowires and Nanotubes. *Small* **8**, 3233-3252 (2012).

234. Gruverman A, Kalinin SV. Piezoresponse force microscopy and recent advances in nanoscale studies of ferroelectrics. *Journal of Materials Science* **41**, 107-116 (2006).

235. Bonnell DA, Kalinin SV, Kholkin AL, Gruverman A. Piezoresponse Force Microscopy: A Window into Electromechanical Behavior at the Nanoscale. *MRS Bull* **34**, 648-657 (2009).

236. Balke N, Bdikin I, Kalinin SV, Kholkin AL. Electromechanical Imaging and Spectroscopy of Ferroelectric and Piezoelectric Materials: State of the Art and Prospects for the Future. *J Am Ceram Soc* **92**, 1629-1647 (2009).

237. Li YW, Li FX. In situ observation of electric field induced crack propagation in BaTiO3 crystals along the field direction. *Scripta Materialia* **67**, 601-604 (2012).

238. Grigoriev A, *et al.* Nanosecond domain wall dynamics in ferroelectric Pb(Zr,Ti)O-3 thin films. *Phys Rev Lett* **96**, (2006).

239. Zhao T, *et al.* Electrical control of antiferromagnetic domains in multiferroic BiFeO3 films at room temperature. *Nat Mater* **5**, 823-829 (2006).

240. Gane N. The Direct Measurement of the Strength of Metals on a Sub-Micrometre Scale. *Proceedings of the Royal Society of London A Mathematical and Physical Sciences* **317**, 367-391 (1970).

241. *PI 95 TEM PicoIndenter User Manual*. Hysitron Incorporated (2011).

242. Rowlinson JS. Translation of J. D. van der Waals' "The thermodynamik theory of capillarity under the hypothesis of a continuous variation of density". *Journal of Statistical Physics* **20**, 197-200 (1979).

243. Cahn JW, Hilliard JE. Free Energy of a Nonuniform System. I. Interfacial Free Energy. *The Journal of Chemical Physics* **28**, 258-267 (1958).

244. Cahn JW. On spinodal decomposition. *Acta Metallurgica* **9**, 795-801 (1961).

245. CAHN J, W., ALLEN S, M. A MICROSCOPIC THEORY FOR DOMAIN WALL MOTION AND ITS EXPERIMENTAL VERIFICATION IN Fe-Al ALLOY DOMAIN GROWTH KINETICS. *J Phys Colloques* **38**, C7-51-C57-54 (1977).

246. Elder KR, Grant M, Provatas N, Kosterlitz JM. Sharp interface limits of phase-field models. *Physical Review E* **64**, (2001).

247. László G, Tamás P, James AW. Modelling polycrystalline solidification using phase field theory. *Journal of Physics: Condensed Matter* **16**, R1205 (2004).

248. Chen LQ, Wang YZ. The continuum field approach to modeling microstructural evolution. *Jom-Journal of the Minerals Metals & Materials Society* **48**, 13-18 (1996).

249. Aranson IS, Kalatsky VA, Vinokur VM. Continuum field description of crack propagation. *Phys Rev Lett* **85**, 118-121 (2000).

250. Chen LQ. Phase-field models for microstructure evolution. *Ann Rev Mater Res* **32**, 113-140 (2002).

251. Zhou H, Pei YM, Li FX, Luo HS, Fang DN. Electric-field-tunable mechanical properties of relaxor ferroelectric single crystal measured by nanoindentation. *Appl Phys Lett* **104**, (2014).

252. Yun WS, Urban JJ, Gu Q, Park H. Ferroelectric properties of individual barium titanate nanowires investigated by scanned probe Microscopy. *Nano Lett* **2**, 447-450 (2002).

253. Grinberg I, *et al.* Perovskite oxides for visible-light-absorbing ferroelectric and photovoltaic materials. *Nature* **503**, 509-+ (2013).

254. Larsen PK, Cuppens R, Spierings G. FERROELECTRIC MEMORIES. *Ferroelectrics* **128**, 265-292 (1992).

255. Guo R, *et al.* Non-volatile memory based on the ferroelectric photovoltaic effect. *Nat Commun* **4**, (2013).

256. Mateos L, Bausa LE, Ramirez MO. Two dimensional ferroelectric domain patterns in Yb3+ optically active LiNbO3 fabricated by direct electron beam writing. *Appl Phys Lett* **102**, (2013).

257. Chen XZ, *et al.* Nano-Imprinted Ferroelectric Polymer Nanodot Arrays for High Density Data Storage. *Adv Funct Mater* **23**, 3124-3129 (2013).

258. Morelli A, Johann F, Burns SR, Douglas A, Gregg JM. Deterministic Switching in Bismuth Ferrite Nanoislands. *Nano Lett* **16**, 5228-5234 (2016).

259. Jiang B, Bai Y, Chu WY, Su YJ, Qiao LJ. Direct observation of two 90 degrees steps of 180 degrees domain switching in BaTiO(3) single crystal under an antiparallel electric field. *Appl Phys Lett* **93**, (2008).

260. Nelson CT, *et al.* Domain Dynamics During Ferroelectric Switching. *Science* **334**, 968-971 (2011).

261. Zeng HR, Shimamura K, Villora EG, Takekawa S, Kitamura K. Reversed domain configuration behavior in BaMgF4 ferroelectric crystal. *J Mater Res* **22**, 1072-1076 (2007).

262. Matzen S, *et al.* Super switching and control of in-plane ferroelectric nanodomains in strained thin films. *Nat Commun* **5**, (2014).

263. Cho YS. Scanning nonlinear dielectric microscopy. *J Mater Res* **26**, 2007-2016 (2011).

264. Nellist PD, McCallum BC, Rodenburg JM. RESOLUTION BEYOND THE INFORMATION LIMIT IN TRANSMISSION ELECTRON-MICROSCOPY. *Nature* **374**, 630-632 (1995).

265. Matsumoto T, *et al.* Multivariate Statistical Characterization of Charged and Uncharged Domain Walls in Multiferroic Hexagonal YMnO3 Single Crystal Visualized by a Spherical Aberration-Corrected STEM. *Nano Lett* **13**, 4594-4601 (2013).

266. Egerton RF, Li P, Malac M. Radiation damage in the TEM and SEM. *Micron* **35**, 399-409 (2004).

267. Tanaka M, Kitamura N, Honjo G. ELECTRON OPTICAL STUDIES OF BARIUM TITANATE SINGLE CRYSTAL FILMS. *J Phys Soc Jpn* **17**, 1197-& (1962).

268. Chen H, Gong H, Ong CK. THE CHARGING BEHAVIOR AND INTERNAL ELECTRIC-FIELD OF PMMA IRRADIATED BY A KILOELECTRONVOLT ELECTRON-BEAM. *J Phys-Condes Matter* **7**, 1129-1137 (1995).

269. Whelan PM, Hodgson MJ. *Essential Principles of Physics*. Murray (1989).

270. Cosslett VE. TRANSMISSION ELECTRON-MICROSCOPY - PHYSICS OF IMAGE-FORMATION AND MICROANALYSIS - REIMER,L. *Nature* **309**, 186-186 (1984).

271. Ciftja O, Hysi I. The electrostatic potential of a uniformly charged disk as the source of novel mathematical identities. *Appl Math Lett* **24**, 1919-1923 (2011).

272. Mahboob I, *et al.* Origin of electron accumulation at wurtzite InN surfaces. *Phys Rev B* **69**, (2004).

273. Wallace SK, McKenna KP. Facet-Dependent Electron Trapping in TiO2 Nanocrystals. *J Phys Chem C* **119**, 1913-1920 (2015).

274. Gatel C, Lubk A, Pozzi G, Snoeck E, Hytch M. Counting Elementary Charges on Nanoparticles by Electron Holography. *Phys Rev Lett* **111**, (2013).

275. Jia CL, Urban K. Atomic-resolution measurement of oxygen concentration in oxide materials. *Science* **303**, 2001-2004 (2004).

276. Cazaux J. Mechanisms of charging in electron spectroscopy. *J Electron Spectrosc Relat Phenom* **105**, 155-185 (1999).

277. Kim DJ, *et al.* Polarization relaxation induced by a depolarization field in ultrathin ferroelectric BaTiO3 capacitors. *Phys Rev Lett* **95**, (2005).

278. Lohse O, Grossmann M, Boettger U, Bolten D, Waser R. Relaxation mechanism of ferroelectric switching in Pb(Zr,Ti)O-3 thin films. *J Appl Phys* **89**, 2332-2336 (2001).

279. Glaum J, Granzow T, Rodel J. Evaluation of domain wall motion in bipolar fatigued lead-zirconate-titanate: A study on reversible and irreversible contributions. *J Appl Phys* **107**, (2010).

280. Vrejoiu I, Le Rhun G, Zakharov ND, Hesse D, Pintilie L, Alexe M. Threading dislocations in epitaxial ferroelectric PbZr0.2Ti0.8O3 films and their effect on polarization backswitching. *Philos Mag* **86**, 4477-4486 (2006).

281. Lou XJ, Wang J. Bipolar and unipolar electrical fatigue in ferroelectric lead zirconate titanate thin films: An experimental comparison study. *J Appl Phys* **108**, (2010).

282. Cruz MP, *et al.* Strain control of domain-wall stability in epitaxial BiFeO3 (110) films. *Phys Rev Lett* **99**, (2007).

283. Chen WJ, Zheng Y, Xiong WM, Feng X, Wang B, Wang Y. Effect of Mechanical Loads on Stability of Nanodomains in Ferroelectric Ultrathin Films: Towards Flexible Erasing of the Non-Volatile Memories. *Sci Rep* **4**, (2014).

284. Catalan G, Sinnamon LJ, Gregg JM. The effect of flexoelectricity on the dielectric properties of inhomogeneously strained ferroelectric thin films. *J Phys-Condes Matter* **16**, 2253-2264 (2004).

285. Zhang SJ, Luo J, Hackenberger W, Shrout TR. Characterization of Pb(In1/2Nb1/2)O-3-Pb(Mg1/3Nb2/3)O-3-PbTiO3 ferroelectric crystal with enhanced phase transition temperatures. *J Appl Phys* **104**, (2008).

286. Zhang S, Luo J, Li F, Meyer Jr RJ, Hackenberger W, Shrout TR. Polarization fatigue in Pb(In0.5Nb0.5)O3–Pb(Mg1/3Nb2/3)O3–PbTiO3 single crystals. *Acta Materialia* **58**, 3773-3780 (2010).

287. Jin YM, Wang YU, Khachaturyan AG, Li JF, Viehland D. Conformal miniaturization of domains with low domain-wall energy: Monoclinic ferroelectric states near the morphotropic phase boundaries. *Phys Rev Lett* **91**, (2003).

288. Wan Q, Chen C, Shen YP. Effects of stress and electric field on the electromechanical properties of Pb(Mg1/3Nb2/3)O-3-0.32PbTiO(3) single crystals. *J Appl Phys* **98**, (2005).

289. Singh AK, Pandey D, Zaharko O. Powder neutron diffraction study of phase transitions in and a phase diagram of (1-x) Pb(Mg1/3Nb2/3)O-3 -xPbTiO(3). *Phys Rev B* **74**, (2006).

290. Viehland D. Symmetry-adaptive ferroelectric mesostates in oriented Pb(BI1/3BII2/3)O-3-PbTiO3 crystals. *J Appl Phys* **88**, 4794-4806 (2000).

291. Gaillard Y, Macias AH, Munoz-Saldana J, Anglada M, Trapaga G. Nanoindentation of BaTiO3: dislocation nucleation and mechanical twinning. *J Phys D-Appl Phys* **42**, (2009).

292. Li YL, Hu SY, Liu ZK, Chen LQ. Effect of substrate constraint on the stability and evolution of ferroelectric domain structures in thin films. *Acta Materialia* **50**, 395-411 (2002).

293. Jin YMM, Wang YU, Khachaturyan AG. Three-dimensional phase field microelasticity theory of a multivoid multicrack system in an elastically anisotropic body: model and computer simulations. *Philos Mag* **83**, 1587-1611 (2003).

294. Khachaturyan.Ag, Shatalov GA. THEORY OF MACROSCOPIC PERIODICITY FOR A PHASE TRANSITION IN SOLID STATE. *Soviet Physics Jetp-Ussr* **29**, 557-& (1969).

295. Lu Y, *et al.* Phase transitional behavior and piezoelectric properties of the orthorhombic phase of Pb(Mg(1/3)Nb(2/3))O(3)-PbTiO(3) single crystals. *Appl Phys Lett* **78**, 3109-3111 (2001).

296. Li YL, Hu SY, Liu ZK, Chen LQ. Effect of electrical boundary conditions on ferroelectric domain structures in thin films. *Appl Phys Lett* **81**, 427-429 (2002).

297. Li YL, Chen LQ, Asayama G, Schlom DG, Zurbuchen MA, Streiffer SK. Ferroelectric domain structures in SrBi2Nb2O9 epitaxial thin films: Electron microscopy and phase-field simulations. *J Appl Phys* **95**, 6332-6340 (2004).

298. Chen LQ, Shen J. Applications of semi-implicit Fourier-spectral method to phase field equations. *Comput Phys Commun* **108**, 147-158 (1998).

299. Choudhury S, Chen LQ, Li YL. Correlation between number of ferroelectric variants and coercive field of lead ziconate titanate single crystals. *Appl Phys Lett* **91**, 3 (2007).

300. Smith RC, Hom CL. Domain wall theory for ferroelectric hysteresis. *J Intell Mater Syst Struct* **10**, 195-213 (1999).

301. Chen IW, Wang Y. A domain wall model for relaxor ferroelectrics. *Ferroelectrics* **206**, 245-263 (1998).

302. Cohen RE. ORIGIN OF FERROELECTRICITY IN PEROVSKITE OXIDES. *Nature* **358**, 136-138 (1992).

303. Ren XB. Large electric-field-induced strain in ferroelectric crystals by point-defect-mediated reversible domain switching. *Nat Mater* **3**, 91-94 (2004).

304. Lu H, *et al.* Mechanically-Induced Resistive Switching in Ferroelectric Tunnel Junctions. *Nano Lett* **12**, 6289-6292 (2012).

305. Chen LF, *et al.* Electrical and mechanical switching of ferroelectric polarization in the 70 nm BiFeO3 film. *Sci Rep* **6**, (2016).

306. Park BH, Kang BS, Bu SD, Noh TW, Lee J, Jo W. Lanthanum-substituted bismuth titanate for use in non-volatile memories. *Nature* **401**, 682-684 (1999).

307. Sun EW, Cao WW. Relaxor-based ferroelectric single crystals: Growth, domain engineering, characterization and applications. *Prog Mater Sci* **65**, 124-210 (2014).

308. Lee D, *et al.* Multilevel Data Storage Memory Using Deterministic Polarization Control. *Adv Mater* **24**, 402-+ (2012).

309. Damjanovic D, Brem F, Setter N. Crystal orientation dependence of the piezoelectric d(33) coefficient in tetragonal BaTiO3 as a function of temperature. *Appl Phys Lett* **80**, 652-654 (2002).

310. Peng J, Chen JZ, Lu HS, He TH, Xu HQ, Lin D. Shear-mode piezoelectric properties of 0.69Pb(Mg1/3Nb2/3)O-3-0.31PbTiO(3) single crystals. *Solid State Commun* **130**, 53-57 (2004).

311. Agar JC, *et al.* Highly mobile ferroelastic domain walls in compositionally graded ferroelectric thin films. *Nat Mater* **15**, 549-+ (2016).

312. Liu S, Grinberg I, Rappe AM. Intrinsic ferroelectric switching from first principles. *Nature* **534**, 360-+ (2016).

313. Nahas Y, Prokhorenko S, Kornev I, Bellaiche L. Topological Point Defects in Relaxor Ferroelectrics. *Phys Rev Lett* **116**, (2016).

314. Chu F, Reaney IM, Setter N. ROLE OF DEFECTS IN THE FERROELECTRIC RELAXER LEAD SCANDIUM TANTALATE. *J Am Ceram Soc* **78**, 1947-1952 (1995).

315. Paruch P, Guyonnet J. Nanoscale studies of ferroelectric domain walls as pinned elastic interfaces. *Comptes Rendus Physique* **14**, 667-684 (2013).

316. Patel S, Chauhan A, Vaish R. Mechanical confinement for tuning ferroelectric response in PMN-PT single crystal. *J Appl Phys* **117**, (2015).

317. Webber KG, Zuo RZ, Lynch CS. Ceramic and single-crystal (1-x)PMN-xPT constitutive behavior under combined stress and electric field loading. *Acta Materialia* **56**, 1219-1227 (2008).

318. Chen LQ. Phase-field method of phase transitions/domain structures in ferroelectric thin films: A review. *J Am Ceram Soc* **91**, 1835-1844 (2008).

319. Hong L, Soh AK, Du QG, Li JY. Interaction of O vacancies and domain structures in single crystal BaTiO(3): Two-dimensional ferroelectric model. *Phys Rev B* **77**, (2008).

320. Meyer B, Vanderbilt D. Ab initio study of ferroelectric domain walls in PbTiO3. *Phys Rev B* **65**, (2002).

321. Catalan G, Schilling A, Scott JF, Gregg JM. Domains in three-dimensional ferroelectric nanostructures: theory and experiment. *J Phys-Condes Matter* **19**, (2007).

322. Dionot J, Geneste G, Mathieu C, Barrett N. Surface polarization, rumpling, and domain ordering of strained ultrathin BaTiO3(001) films with in-plane and out-of-plane polarization. *Phys Rev B* **90**, (2014).

323. Das RR, Bhattacharya P, Pérez W, Katiyar RS. High remanent polarization in Sr1−xCaxBi2Ta2O9 ferroelectric thin films. *Appl Phys Lett* **81**, 4052-4054 (2002).

324. Okunishi E, Sawada H, Kondo Y. Experimental study of annular bright field (ABF) imaging using aberration-corrected scanning transmission electron microscopy (STEM). *Micron* **43**, 538-544 (2012).